JETP Letters, Vol. 74, No. 5, 2001, pp. 247–250. Translated from Pis'ma v Zhurnal Éksperimental'noĭ i Teoreticheskoĭ Fiziki, Vol. 74, No. 5, 2001, pp. 275–278.

Effect of Massive Fields on Inflation

S. G. Rubin

Moscow State Engineering Physics Institute (Technical University), Kashirskoe sh. 31, Moscow, 115409 Russia

Research–Education Center on Cosmomicrophysics "Cosmion," Moscow, 125047 Russia

e-mail: serg.rubin@mtu-net.ru

Received May 3, 2001; in final form, July 25, 2001

Effects caused by an additional massive scalar field interacting with an inflaton field are analyzed. Inflation is shown to have two stages, the first of which is dominant and characterized by ultraslow dynamics of the inflaton field. Constraints on the model parameters are obtained. © *2001 MAIK "Nauka/Interperiodica".*

PACS numbers: 98.80.Cq

The occurrence of inflationary era in the evolution of the universe seems to be inevitable because it allows the explanation of a great number of observed facts [1, 2]. Early inflation mechanisms [3, 4] were based on the consistent equations of scalar and gravitational fields. Nevertheless, the simplest inflation models could not explain the totality of observed data. In particular, the predictions of the chaotic inflation model [5, 6] about temperature fluctuations in cosmic background radiation contradict observations except for a rather unnatural form of the inflaton field potential (see also [7]).

At the same time, the interaction of a large number of various fields existing in nature should give rise to new phenomena in inflation. Further development of the theory has led to the emergence of inflation models involving additional fields, among which are the models of hybrid inflation [8] and inflation on the pseudo Nambu–Goldstone field [9]. The interaction of the classical—inflaton—field with other particles produced by it is one of the basic elements of some inflation models. This effect provides a basis for the warm inflation scenario [10], which, however, is not free from flaws [11]; the back effect of the produced particles on the dynamics of inflaton field was considered in [12, 13].

The purpose of this work is to study the back reaction of an additional field on the classical motion of the basic inflaton field. It is assumed that the additional field is massive enough for it to be at the minimum of its effective potential during inflation. Nevertheless, it is shown below that its influence can noticeably decelerate the system's motion.

In what follows, the simplest form of interaction is considered allowing the analytical results to be obtained. Namely, we introduce, apart from the inflaton field φ, an additional scalar field χ and write the action in the form

$$S = \int d^4x\sqrt{-g}\Big[\frac{1}{2}\varphi_{,\mu}\varphi^{,\mu} - V(\varphi) + \frac{1}{2}\chi_{,\mu}\chi^{,\mu} - \frac{1}{2}m_\chi^2\chi^2 - \kappa\chi u(\varphi)\Big], \quad (1)$$

where $u(\varphi)$ is a polynomial of degree no higher than three for the renormalizable theories. In what follows, $u(\varphi) = \varphi^2$ is taken for definiteness. The first power of the field χ in the interaction is necessary in order to obtain compact analytical results valid for an arbitrary coupling constant κ, rather than the expansion in powers of this constant. The interaction of this type arises in supersymmetric theories and is considered in hybrid inflation scenarios [14]. Dolgov and Hansen [12] used this type of interaction in studying the back effect of produced particles on the motion of a classical field.

The set of the classical equations for both fields is written as

$$\frac{1}{\sqrt{-g}}\partial_\mu(\sqrt{-g}\partial^\mu\chi) + m_\chi^2\chi + \kappa\varphi^2 = 0,$$
$$\frac{1}{\sqrt{-g}}\partial_\mu(\sqrt{-g}\partial^\mu\varphi) + V'(\varphi) + 2\kappa\varphi\chi = 0. \quad (2)$$

Let us consider the case of heavy χ particles. In the inflationary era, this means that $m_\chi \gg H$ and the Hubble constant $H(\varphi)$ is determined by the slowly varying classical field φ. The first of Eqs. (2) can be brought to the form

$$\chi(x) = -\kappa\int G(x, x')\varphi^2(x')\sqrt{-g}dx'. \quad (3)$$

0021-3640/01/7405-0247$21.00

The right-hand side of Eq. (3) can be simplified using the equation for the Green's function $G(x, x')$ [15] written as

$$G(x, x') = \frac{1}{m_\chi^2\sqrt{-g}}\delta(x-x') - \frac{1}{m_\chi^2\sqrt{-g}}\partial_\mu\sqrt{-g}\partial^\mu G(x, x'). \quad (4)$$

After two iterations, the field χ takes the explicit form

$$\chi(x) \simeq -\frac{\kappa}{m_\chi^2}\varphi^2(x) + \frac{\kappa}{m_\chi^4}\partial_\mu\sqrt{-g}\partial^\mu\varphi^2(x), \quad (5)$$

which is valid if the derivatives of the inflaton field φ are small. Substituting this expression into the second of Eqs. (2), one arrives at the following classical equation for the inflaton field:

$$\partial_\mu\sqrt{-g}\partial^\mu\varphi + \sqrt{-g}V'_{\rm ren}(\varphi) + \frac{2\alpha^2}{m_\chi^2}\varphi\partial_\mu\sqrt{-g}\partial^\mu\varphi^2 = 0, \quad (6)$$

where $\alpha = \kappa/m_\chi$ is a dimensionless parameter and $V_{\rm ren}(\varphi) = V(\varphi) - (\alpha^2/2)\varphi^4$ is the inflaton-field potential renormalized due to interaction with the field χ. The last term on the left-hand side of Eq. (6) is usually treated as a back reaction of radiation [12]. Equation (6) corresponds to the effective action for inflaton field

$$S_{\rm eff} = \int d^4x\sqrt{-g}\left[\frac{1}{2}\partial_\mu\varphi\partial^\mu\varphi - V_{\rm ren}(\varphi) + \frac{\alpha^2}{2m_\chi^2}\partial_\mu\varphi^2\partial^\mu\varphi^2\right]. \quad (7)$$

Note that the correction $\delta V = -(\alpha^2/2)\varphi^4$ to the potential follows from the analysis of classical Eqs. (2). At the same time, the same expression can be obtained by calculating the first quantum correction to the φ-field potential interacting with the field χ [see Eq. (1)] at zero 4-momenta of external lines corresponding to the φ-field quanta. The internal line corresponds to the χ-field propagator in the *s* and *t* channels.

The last term in Eq. (7) is important for further consideration. Morris [16] showed that a change in the form of the kinetic term in the scalar–tensor theory leads to the inflation on a lower than ordinary energy scale, which is in agreement with the conclusions of this work. A similar result can be obtained by introducing a nonminimized interaction between an inflaton and a gravitational field [17, 18].

In general, the renormalized potential contains the sum of contributions from the corrections due to interaction with all existing fields. In the first model of chaotic inflation with the $\lambda\varphi^4$ potential, the observed data led to a value of $\lambda \sim 10^{-13}$. This means that the corrections introduced to the expression for λ by all fields, including the correction $\delta V = -(\alpha^2/2)\varphi^4$ considered in this work, must cancel with a high accuracy. Below, it is demonstrated that the renormalization of the kinetic term allows one, in particular, to materially weaken the conditions imposed by the observations on the parameters of the theory. In weak fields, the contribution from the last term in Eqs. (6) and (7) is negligible. As to the inflation stage, it can be substantial at large field magnitudes.

In inflation, the field is assumed to be uniform; i.e., $\varphi = \varphi(t)$ and Eq. (6) is greatly simplified. Taking into account that the scale factor a is expressed in terms of the Hubble constant H in the ordinary way, $a = \exp(\int Hdt)$, Eq. (6) can be rewritten as

$$\frac{d^2\varphi}{dt^2} + 3H\frac{d\varphi}{dt} + V'_{\rm ren}(\varphi) + \frac{4\alpha^2}{m_\chi^2}\left[3H\varphi^2\frac{d\varphi}{dt} + \varphi^2\frac{d^2\varphi}{dt^2} + \varphi\left(\frac{d\varphi}{dt}\right)^2\right] = 0. \quad (8)$$

The slow time variation of the field φ implies that the terms proportional to $d^2\varphi/dt^2$ and $(d\varphi/dt)^2$ are small. Neglecting them, one obtains the easily integrable equation

$$\left(3H + \frac{12H\alpha^2}{m_\chi^2}\varphi^2\right)\dot\varphi + V'_{\rm ren}(\varphi) = 0. \quad (9)$$

In what follows, the nonrenormalized potential is taken in the form $V(\varphi) = \lambda_0\varphi^4$, and, therefore, $V_{\rm ren} = \lambda\varphi^4$, where $\lambda = \lambda_0 - \alpha^2/2$. Taking into account the usual relation $H = \sqrt{8\pi V_{\rm ren}(\varphi)/3}/M_P$ between the Hubble constant and the potential, one can easily obtain the field variable φ as an implicit function of time:

$$t = \frac{\sqrt{3\pi/2}}{M_P\sqrt{\lambda}}\left[\ln(\varphi_0/\varphi) + \frac{2\alpha^2}{m_\chi^2}(\varphi_0^2 - \varphi^2)\right]. \quad (10)$$

Here, the first term reproduces the result of the standard inflation model. The second term results from the interaction of the inflaton field and the field χ. It follows from Eq. (9) that the second term dominates at

$$\varphi > \varphi_c \equiv m_\chi/2\alpha. \quad (11)$$

Therefore, there are two inflation stages: the ordinary stage at $\varphi \le \varphi_c$ and the ultraslow stage at $\varphi \ge \varphi_c$. Indeed, the field motion velocity

$$\dot\varphi = \frac{m_\chi^2}{12\alpha^2\varphi^2}\frac{V'_{\rm ren}}{H},$$

obtained from Eq. (9) with allowance made for Eq. (11), is much smaller than its ordinary value $\dot\varphi = V'_{\rm ren}/3H$. The first inflation stage is completed when condition (11) ceases to be true. Then, the ordinary inflation stage

begins and continues as long as the condition $\ddot{\varphi} \ll 3H\dot{\varphi}$ is satisfied.

Because the second stage has been much studied, I will analyze the first stage, for which the second term in Eqs. (9) and (10) dominates, i.e., for $\varphi > \varphi_c$. In this case, the field depends on time as

$$\varphi(t) = \sqrt{\varphi_0^2 - t\frac{\sqrt{\lambda}M_P m_\chi^2}{\alpha^2\sqrt{6\pi}}}. \quad (12)$$

This expression is derived under the "ultraslow roll-down" condition, which, according to Eq. (8), has the rather unusual form $\ddot{\varphi} \ll 12H\varphi^2\dot{\varphi}(\alpha^2/m_\chi^2)$.

Let us determine the amplitude of quantum fluctuations arising at the first inflation stage for the potential $\lambda\varphi^4$. This can most easily be done by taking into account that the first term in Eqs. (6) and (7) is much smaller than the third one and introducing an auxiliary field $\tilde{\varphi}$, after which the substitution $\tilde{\varphi} = (\alpha/m_\chi)\varphi^2$ brings action (7) to the form

$$S = \int dx\sqrt{-g}\left[\frac{1}{2}\partial_\mu\tilde{\varphi}\partial^\mu\tilde{\varphi} - \frac{1}{2}\tilde{m}^2\tilde{\varphi}^2\right], \quad (13)$$

corresponding to a free massive field with mass $\tilde{m} \equiv m_\chi\sqrt{2\lambda}/\alpha$. This substitution is valid at the inflation stage under consideration, when the field value is positive. The fluctuation amplitude for the massive noninteracting field is known to be $\Delta\tilde{\varphi} = \sqrt{3/8\pi^2}\,H^2/\tilde{m}$ [19]. On the scale of modern horizon, the constraint on the mass of quanta of this field is also known: $\tilde{m} \sim 10^{-6}M_P$, as obtained from the comparison with the COBE measurements of the energy-density fluctuations, $\delta\rho/\rho \approx 6\times 10^{-5}$ [20]. Expressing $\tilde{m}$ in terms of the initial parameters, one obtains the following relation between them:

$$\frac{m_\chi}{M_P}\frac{\sqrt{\lambda}}{\alpha} \sim 10^{-6}. \quad (14)$$

Let us determine the field φ_U at which a causally connected area was formed, which generated the visible part of the universe. The number of e-foldings necessary to explain the observed data is $N_U \simeq 60$. Then, using the relation $N_U = \int_{\varphi_U}^{\varphi_{\rm end}} H dt$, one has

$$N_U = \int_{\varphi_U}^{\varphi_c}\frac{H(\varphi)}{\dot{\varphi}}d\varphi + \int_{\varphi_c}^{\varphi_{\rm end}}\frac{H(\varphi)}{\dot{\varphi}}d\varphi = \frac{2\pi\alpha^2}{M_P^2 m_\chi^2}(\varphi_U^4 - \varphi_c^4) + \frac{\pi}{M_P^2}(\varphi_c^2 - \varphi_{\rm end}^2), \quad (15)$$

where it is taken into account that the time dependences of the field φ at the first and the second inflation stages are different. The second stage is completed at $\varphi = \varphi_{\rm end}$. Assuming that the first term containing the initial value of the field φ_U dominates, one obtains the desired expression

$$\varphi_U \simeq \left(\frac{N_U}{2\pi}\right)^{1/4}\sqrt{\frac{M_P m_\chi}{\alpha}}. \quad (16)$$

Note that the visible part of the universe in this case can be formed at $\varphi < M_P$, i.e., rather late. This is explained by the fact that, at the first stage, the field moves ultraslowly and the universe has had time to expand to the appropriate size. Expression (16) differs substantially from the standard result $\varphi_U = \sqrt{N_U/\pi}\,M_P$, which is obtained for the inflaton field with potential $\lambda\varphi^4$ without regard for the interaction with the massive fields of other sorts.

The second term in Eq. (15) determines the number N_2 of e-foldings at the second inflation stage. Assuming that $\varphi_c^2 \gg \varphi_{\rm end}^2$ and substituting the value φ_c from Eq. (11), one has

$$N_2 = \frac{\pi}{4}\left(\frac{m_\chi}{\alpha M_P}\right)^2. \quad (17)$$

Evidently, over a wide range of parameters α and m_χ, the second stage may be short or absent at all.

The above arguments are valid if the field χ is massive enough so that it is at the minimum of its effective potential during inflation. As is known, the field rapidly rolls down to the minimum if the Hubble constant becomes smaller than the field mass, i.e., if $H < m_\chi$. The Hubble constant depends on time. For this reason, the necessary estimates will be made for the instant the visible universe originated ($\varphi = \varphi_U$), that is, when the largest scale fluctuations arise. Simple mathematics gives

$$m_\chi > H(\varphi_U) \longrightarrow \frac{\sqrt{\lambda}}{\alpha} < \sqrt{\frac{3}{4N_U}} \sim 0.1. \quad (18)$$

This restriction indicates that one cannot fully avoid the fine tuning of parameters because $\lambda = \lambda_0 - \alpha^2/2$ and, according to constraint (18), $\alpha^2 \geq 100\lambda$. Nevertheless, this fitting is weaker than that requiring the cancellation of all quantum corrections down to a value of $\sim 10^{-13}$ in the early inflation models with the potential $\lambda\varphi^4$.

Using Eqs. (14) and (18), one can easily obtain a rather weak limitation $m_\chi \geq 10^{-5}M_P$ on the mass of the additional field χ.

Thus, a particular example was taken in this work to demonstrate that massive fields, even being at their minimum (which depends on the magnitude of the inflaton field), can materially decelerate the motion of the main—inflaton—field at the first inflation stage. Due to the first, ultraslow, stage, the visible universe

could form at $\varphi_U < M_P$. The second stage precedes the completion of inflation and evolves in the ordinary way, but it is rather short. In particular, for the parameters $m_\chi = 10^{-3}M_P$ and $\lambda = 10^{-6}$ satisfying constraints (14) and (18), one has the following: the visible universe formed at $\varphi_U \approx 5 \times 10^{-2}M_P$; the first and second stages are separated at $\varphi_c \approx 5 \times 10^{-4}M_P$; and the second inflation stage is much shorter than the first one.

The inclusion of the interaction between the inflaton field and more massive fields enables one to materially weaken the constraints imposed on the potential parameters by the smallness of energy-density fluctuations, although one fails to fully avoid the fine tuning of the parameters.

The effects considered are associated with the renormalization of the kinetic term for the inflaton field interacting with an additional massive field. Because the similar renormalization takes place for all sorts of additional fields [21], the inclusion of new fields will enhance the effect of deceleration of classical motion at high energies.

I am grateful to A.A. Sakharov for his useful comments, M.Yu. Khlopov, for his interest in the work; and the referee, for constructive criticism. This work was supported by the Russian State Scientific Engineering Program “Astronomy. Fundamental Cosmic Research” (project “Cosmoparticle Physics”) and by the International Collaboration Cosmion–ETHZ and Epcos–AMS.

REFERENCES

1. A. D. Linde, *The Large-Scale Structure of the Universe* (Harwood Academic Publ., London, 1990).
2. M. Yu. Khlopov, *Cosmoparticle Physics* (World Scientific, Singapore, 1999).
3. A. Starobinsky, Phys. Lett. B **91B**, 99 (1980).
4. A. H. Guth, Phys. Rev. D **23**, 347 (1981).
5. A. D. Linde, Phys. Scr. T **36**, 35 (1991).
6. A. D. Linde, Phys. Lett. B **129B**, 177 (1983).
7. R. H. Brandenberger, hep-ph/0101119 (2001).
8. A. D. Linde, Phys. Lett. B **259**, 38 (1991).
9. K. Freese, Phys. Rev. D **50**, 7731 (1994); astro-ph/9405045 (1994).
10. A. N. Taylor and A. Berera, Phys. Rev. D **62**, 083517 (2000); astro-ph/0006077 (2000).
11. J. Yokoyama and A. Linde, Phys. Rev. D **60**, 083509 (1999); hep-ph/9809409 (1998).
12. A. D. Dolgov and S. H. Hansen, Nucl. Phys. B **548**, 408 (1999); hep-ph/9810428 (1998).
13. I. Dymnikova and M. Yu. Khlopov, Mod. Phys. Lett. A **15**, 2305 (2000).
14. D. H. Luth and E. D. Stewart, Phys. Rev. D **54**, 7186 (1996); hep-ph/9606412 (1996).
15. N. D. Birrell and P. C. W. Davies, *Quantum Fields in Curved Space* (Cambridge Univ. Press, Cambridge, 1982).
16. J. R. Morris, gr-qc/0106022 (2001).
17. T. Futamase and K. Maeda, Phys. Rev. D **39**, 399 (1989).
18. V. Faraoni, Phys. Rev. D **53**, 6813 (1996).
19. T. S. Bunch and P. C. W. Davies, Proc. R. Soc. London, Ser. A **360**, 117 (1978).
20. C. L. Bennett, Astrophys. J. Lett. **464**, L1 (1996).
21. C. Itzykson and J.-B. Zuber, *Quantum Field Theory* (McGraw-Hill, New York, 1984).

Translated by R. Tyapaev

JETP Letters, Vol. 74, No. 5, 2001, pp. 251–254. Translated from Pis'ma v Zhurnal Éksperimental'noĭ i Teoreticheskoĭ Fiziki, Vol. 74, No. 5, 2001, pp. 279–282.

Rotation of Neutron Spin in Passing through a Noncentrosymmetric Single Crystal

V. V. Voronin*, E. G. Lapin, S. Yu. Semenikhin, and V. V. Fedorov

Petersburg Nuclear Physics Institute, Russian Academy of Sciences, Gatchina, 188300 Russia

** e-mail: vvv@mail.pnpi.spb.ru*

Received July 2, 2001

Rotation of the spin of cold neutrons passing through a noncentrosymmetric single crystal is observed. This effect is caused by the Schwinger interaction of the magnetic moment of a moving neutron with the crystalline electric field in a noncentrosymmetric single crystal and depends both on the direction of neutron trajectory in the crystal and on its energy. It is shown that the characteristic magnitude of the effect for α-quartz is $\simeq(1–2)\times10^{-4}$ rad/cm over a wide wavelength range (from 2.8 to 5.5 Å) and is determined by the degree of beam monochromaticity [$\Delta\lambda/\lambda = (2–5)\times10^{-2}$ in our experiment]. This magnitude corresponds to an electric field of $\simeq(0.5–1)\times10^5$ V/cm acting on a neutron. The measured value agrees well with the theoretical calculation. © *2001 MAIK "Nauka/Interperiodica".*

PACS numbers: 14.20.Dh; 61.12.Ld

1. Previously, we showed that neutrons passing through a noncentrosymmetric single crystal can experience a strong electric crystalline field [1, 2]. The magnitude of this field depends on the direction of neutron trajectory in the crystal and attains a maximum of ~$(10^8–10^9)$ V/cm if the Bragg condition is exactly met [3, 4].

Forte and Zeyen [5] observed the neutron spin rotation in the Bragg diffraction with a deviation from the exact Bragg condition of several Bragg widths, which corresponds to $\Delta\lambda/\lambda \sim 10^{-5}$. The measured effect proved to be several times weaker than was predicted theoretically, probably, because of low perfection of the single crystal used.

In this work, the neutron-optical effects are considered. This implies that the deviation from the Bragg condition may attain $10^3–10^5$ Bragg widths. In [6], we have shown theoretically that the electric field $\mathbf{E}_{\text{sum}}$ summed over all planes of a polar $PbTiO_3$ crystal may attain $\approx2\times10^6$ V/cm at a deviation of 10^4 Bragg widths from the Bragg condition [6].

The electric field does not decrease at a considerable deviation from the Bragg condition because the electric fields produced by different crystallographic planes combine, under certain conditions, into a field which is considerably stronger than the field produced by one plane.

These phenomena are of interest because they can be used in the search for the electric dipole moment of a neutron and in connection with the proposal [7, 8] of searching for the *T*-invariance violation in strong interactions (i.e., a "strong" or "nuclear" dipole moment of a neutron) using a neutron moving with an energy near the *P*-wave resonance in a noncentrosymmetric crystal, because the deviation from the Bragg condition is large enough for such neutrons.

2. Let a neutron with an energy of $E = \hbar^2k_0^2/2m$ be incident on a crystal away from the Bragg condition for any system of crystallographic planes. Then the neutron wave function can conveniently be written using the perturbation theory [9] and decomposing in the reciprocal lattice vectors **g**:

$$\psi(\mathbf{r}) = e^{i\mathbf{kr}}\left(1 + \sum_g \frac{V_g}{E_k - E_{k_g}} e^{i\mathbf{gr}}\right), \qquad (1)$$

where **k** is the neutron wave vector with allowance made for the refraction at the crystal boundary; $\mathbf{k}_g = \mathbf{k} + \mathbf{g}$; $V_g = v_g e^{i\phi_g}$ is the *g*th harmonic of the periodic potential of interaction between the neutron and crystal; and $E_k = \hbar^2k^2/2m$ and $E_{k_g} = \hbar^2k_g^2/2m$ are the neutron energies for the (**k**) and (**k** + **g**) states, respectively. The difference $E_k - E_{k_g}$ is, in fact, a deviation from the Bragg condition in energy units. The neutron density distribution $|\psi(\mathbf{r})|^2$ in the crystal has the form

$$|\psi(\mathbf{r})|^2 = 1 + \sum_g \frac{2v_g}{E_k - E_{k_g}} \cos(\mathbf{gr} + \phi_g). \qquad (2)$$

It is easy to see that the sign of the deviation $E_k - E_{k_g}$ from the Bragg condition determines the "concentration" of the neutron wave at maxima or minima of the periodic potential of neutron interaction with the crys-

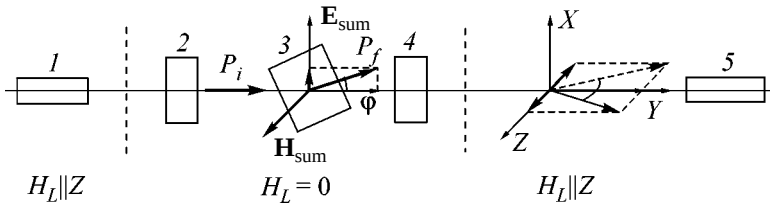

Fig. 1. Experimental scheme: (*1*) neutron guide–polarizer, (*2*) coil for spin rotation about the *X* axis by π/2, (*3*) 14 × 14 × 3.5-cm single crystal of α-quartz, (*4*) ±π/2 coil for rotation about the *Y* axis, (*5*) neutron guide–analyzer; H_L is the guiding magnetic field and *O* is the axis of crystal rotation ($O \| Z$).

tal. This changes the neutron kinetic energy as [9]

$$\tilde{E}_k = E - V_0 - \sum_g \frac{V_g V_{-g}}{E_k - E_{k_g}}, \qquad (3)$$

where V_0 is the zeroth harmonic or the mean crystal potential.

Thus, the crystal structure of the scatterer introduces correction to the mean crystal potential V_0 in the second order of the perturbation theory; i.e., when passing through the crystal without Bragg reflection, the neutron still "feels" the crystal structure. This correction is caused by the concentration of neutrons either in the "nuclear" crystallographic planes (maxima of the nuclear potential) or between them.

All types of neutron interaction with the crystal contribute to the quantity $V_g V_{-g}$.

Let us consider a nonmagnetic, nonabsorbing crystal. In this case, the quantity V_g can be written as [9]

$$V_g = v_g^N e^{i\phi_g^N} + i v_g^E e^{i\phi_g^E} \mu \frac{\boldsymbol{\sigma}[\mathbf{g} \times \mathbf{v}]}{c}, \qquad (4)$$

where v_g^N and ϕ_g^N are, respectively, the amplitude and phase of the *g*th harmonic of the potential of nuclear interaction of a neutron and crystal; v_g^E and ϕ_g^E are, respectively, the amplitude and phase of the *g*th harmonic of the electric crystal potential; μ and v are the magnetic moment and the velocity of a neutron, respectively; and *c* is the speed of light.

Substituting Eq. (4) into Eq. (3) and taking into account that $V_g = V_{-g}^*$ for a nonabsorbing crystal, we obtain

$$\tilde{E}_k = E - V_0 - \sum_g \frac{(v_g^N)^2}{E_k - E_{k_g}} - \mu \frac{\boldsymbol{\sigma}[\mathbf{E}_{\rm sum} \times \mathbf{v}]}{c}, \qquad (5)$$

where

$$\mathbf{E}_{\rm sum} = \sum_g \frac{2 v_g^N}{E_k - E_{k_g}} v_g^E \sin(\Delta\phi_g)\mathbf{g} \qquad (6)$$

means the electric field summed over all reflecting planes and acting on a neutron, and $\Delta\phi_g \equiv \phi_g^N - \phi_g^E$ is the phase shift between the *g*th harmonics of the nuclear and electric crystal potentials.

For a centrosymmetric crystal, $\Delta\phi_g \equiv 0$ and, therefore, $\mathbf{E}_{\rm sum} \equiv 0$.

In a noncentrosymmetric crystal, because the "electric" crystal planes are displaced from the "nuclear" planes, i.e., $\Delta\phi_g \neq 0$, an electric field arises acting on a neutron. As a result, the interaction potential between neutron and crystal becomes spin-dependent, leading to the neutron spin rotation about the $\mathbf{H}_{\rm sum} = [\mathbf{E}_{\rm sum} \times \mathbf{v}]/c$ direction through an angle of

$$\Delta\varphi_s = 2\frac{L}{\hbar v}\mu \frac{\boldsymbol{\sigma}[\mathbf{E}_{\rm sum} \times \mathbf{v}]}{c}, \qquad (7)$$

where *L* is the crystal thickness.

Let us consider an absorbing crystal. This can be done by introducing the imaginary part in the nuclear crystal potential; i.e.,

$$V_g = v_g^N e^{i\phi_g^N} + i v_g^{N'} e^{i\phi_g^{N'}} + i v_g^E e^{i\phi_g^E} \mu \frac{\boldsymbol{\sigma}[\mathbf{g} \times \mathbf{v}]}{c}, \qquad (8)$$

where $v_g^{N'}$ and $\phi_g^{N'}$ are, respectively, the amplitude and phase of the *g*th harmonic of the imaginary part of the nuclear potential.

Then we obtain for $\tilde{E}_k$

$$\tilde{E}_k = E - V_0 - V_{\langle g \rangle} - i(V_0' + V_{\langle g \rangle}') - \mu \frac{\boldsymbol{\sigma}[(\mathbf{E}_{\rm sum} + i\mathbf{E}_{\rm sum}') \times \mathbf{v}]}{c}, \qquad (9)$$

where

$$V_{\langle g \rangle} = \sum_g \frac{(v_g^N)^2 - (v_g^{N'})^2}{E_k - E_{k_g}}, \qquad (10)$$

$$V_{\langle g \rangle}' = \sum_g \frac{2 v_g^N v_g^{N'} \cos(\phi_g^N - \phi_g^{N'})}{E_k - E_{k_g}}, \qquad (11)$$

$$\mathbf{E}_{\rm sum}' = \sum_g \frac{2 v_g^{N'}}{E_k - E_{k_g}} v_g^E \sin(\phi_g^{N'} - \phi_g^E)\mathbf{g}. \qquad (12)$$

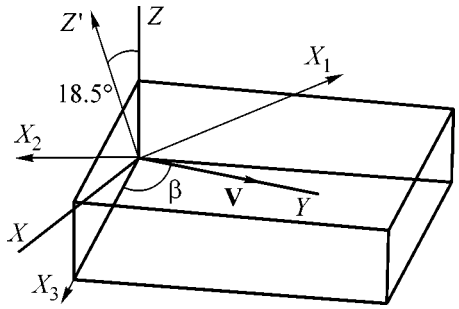

Fig. 2. Crystal orientation.

Thus, the imaginary part of the interaction potential between a neutron and a noncentrosymmetric crystal, i.e., absorption, depends both on the direction and magnitude of neutron velocity and on the spin direction.

Calculations show that the diffraction corrections in the α-quartz crystal over a wide wavelength range are

$$V_{\langle g\rangle} + iV'_{\langle g\rangle} \approx 10^{-3}(V_0 + iV'_0),$$

$$\boldsymbol{\mu\sigma}[(\mathbf{E}_{\text{sum}} + i\mathbf{E}'_{\text{sum}}) \times \mathbf{v}]/c \approx 10^{-6}(V_0 + iV'_0)$$

and rapidly increase as one of the reflecting planes or a group of planes is approached.

3. The experimental scheme is shown in Fig. 1.

To study the spin rotation, the polarization vector was oriented along the neutron velocity (*Y* axis), and the *X* component of this vector was measured after passing through the crystal. If the effect is absent, this component must be zero. The spectral dependence was measured by the time-of-flight method. To exclude the spurious effect caused by the nonzero *X* component of the polarization vector in actual experiment, the differential effect was measured for two crystal positions, differing by the rotation through 180° about the *Z* axis (which is equivalent to changing **v** by –**v**). In this case, the effect must reverse its sign [see Eq. (7)].

A $14 \times 14 \times 3.5$-cm α-quartz crystal was used in the experiment. The direction of neutron propagation in the laboratory coordinate system (*X, Y, Z*) and in the crystallographic coordinate system (Z', X_1, X_2, X_3) is shown in Fig. 2. The crystallographic axis Z' was rotated about the laboratory axis *Z* through an angle of 18.5°, which was dictated by the cut of the actual crystal. The angle β of crystal rotation was measured from the [110] axis (X_3).

The spectral dependence of the angle of neutron spin rotation was measured for the crystal positions corresponding to β = 90° and 30°. The resulting dependences are shown in Figs. 3 and 4. The solid lines are calculated by averaging Eq. (7) over the experimental energy resolution. It is seen that, as the Bragg reflections with nonzero electric field (indicated by dashed lines in Figs. 3 and 4) are approached, the effect increases and its maximum value is determined by the experimental energy resolution. The theoretical dependences agree well with the experimental data. The right ordinate axis is for the electric field $\mathbf{E}_{\text{sum}}$. The case shown in Fig. 3 corresponds to the situation where the positions of the planes contributing to $\mathbf{E}_{\text{sum}}$ virtually coincide, slightly increasing the net effect and making its observation easier. Figure 4 corresponds to the case of a more or less arbitrary choice of the crystal orientation. One can see that the effect at the level of $\pm 5 \times 10^{-5}$ rad/cm occurs over the entire wavelength range studied.

4. Thus, it is demonstrated experimentally that the neutron-optical effect of spin rotation due to the Schwinger interaction between the magnetic moment of a moving neutron and the crystalline electric field

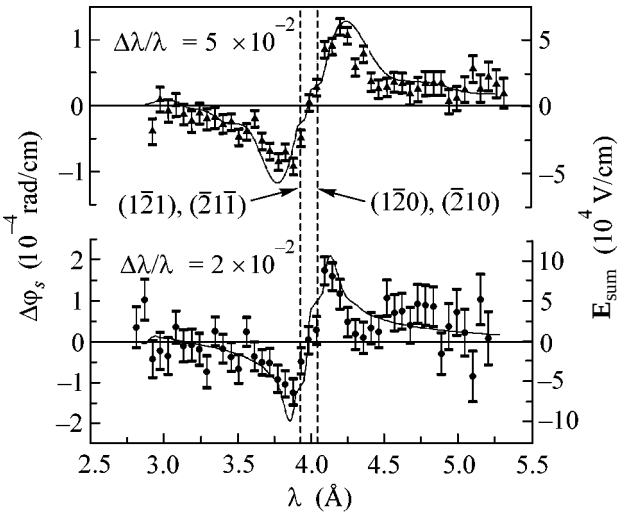

Fig. 3. The spectral dependence of the rotation angle $\Delta\varphi_s$ of the polarization vector for β = 90°.

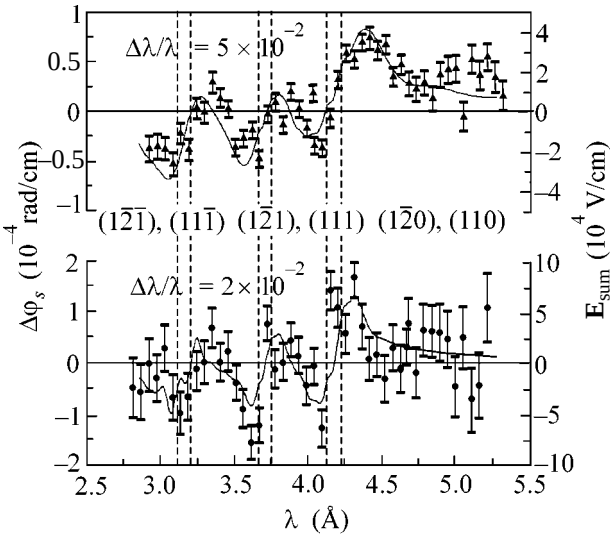

Fig. 4. The spectral dependence of the rotation angle $\Delta\varphi_s$ of the polarization vector for β = 30°.

can occur in a noncentrosymmetric crystal. The characteristic rotation parameter for the α-quartz crystal is $\sim 10^{-4}$ rad/cm, which corresponds to the electric field $\simeq 0.5 \times 10^5$ V/cm acting on a neutron.

It should be noted that the observed effect is evidence for the presence of other diffraction corrections, i.e., Eqs. (10)–(12), which lead to the orientational and energy dependences of the neutron–crystal interaction potential. In particular, the term (11) should give rise to the dependence of the imaginary part of nuclear interaction (absorption) on the direction of motion and energy of a neutron, whereas the term (12) should lead to the dependence of the absorption coefficient on the direction of neutron spin.

We are grateful to A.K. Rad'kov for assistance in theoretical calculations; and O.I. Sumbaev, V.L. Rumyantsev, and V.L. Alekseev for numerous useful discussions. This work was supported by the Russian Foundation for Basic Research (project nos. 00-02-16854, 01-02-06263), the INTAS (grant no. 00-00043), the sixth Expert Competition for Young Scientists of the Russian Academy of Sciences in 1999 (project no. 76), and the State Program "Integration" (project no. 278 of the field no. 3.2 in 2001).

REFERENCES

1. V. L. Alexeev, V. V. Fedorov, E. G. Lapin, *et al.*, Nucl. Instrum. Methods Phys. Res. A **284**, 181 (1989).
2. V. L. Alekseev, V. V. Voronin, E. G. Lapin, *et al.*, Zh. Éksp. Teor. Fiz. **96**, 1921 (1989) [Sov. Phys. JETP **69**, 1083 (1989)].
3. V. V. Fedorov, E. G. Lapin, S. Yu. Semenikhin, and V. V. Voronin, Physica B (Amsterdam) **297**, 293 (2001).
4. V. V. Voronin, E. G. Lapin, S. Yu. Semenikhin, and V. V. Fedorov, Pis'ma Zh. Éksp. Teor. Fiz. **72**, 445 (2000) [JETP Lett. **72**, 308 (2000)].
5. M. Forte and C. M. E. Zeyen, Nucl. Instrum. Methods Phys. Res. A **284**, 147 (1989).
6. V. V. Voronin and V. V. Fedorov, Preprint NP-8-1999, 2293, PIYaF (Inst. of Nuclear Physics, Gatchina, 1999).
7. V. G. Baryshevskiĭ, Yad. Fiz. **58**, 1558 (1995) [Phys. At. Nucl. **58**, 1471 (1995)].
8. V. G. Baryshevsky, J. Phys. G **23**, 509 (1997).
9. V. V. Fedorov, in *Proceedings of the XXVI Winter School of Leningrad Institute of Nuclear Physics, Leningrad, 1991*, p. 65.

Translated by R. Tyapaev

JETP Letters, Vol. 74, No. 5, 2001, pp. 255–257. Translated from Pis'ma v Zhurnal Éksperimental'noĭ i Teoreticheskoĭ Fiziki, Vol. 74, No. 5, 2001, pp. 283–286.

Ising-Type Exchange Interaction in Two-Level Optical Systems

A. R. Kessel* and I. S. Donskaya

Zavoiskiĭ Physicotechnical Institute, Kazan Scientific Center, Russian Academy of Sciences, Sibirskiĭ trakt 10/7, Kazan 29, 420029 Tatarstan, 664033 Russia

** e-mail: kessel@dionis.kfti.knc.ru*

Received June 13, 2001; in final form, August 8, 2001

It is shown that the indirect interaction of pseudospins via radiation field in a two-level optical system contains pseudospin energy components of the Ising exchange-interaction type. The conditions under which this interaction can show up in optical spectra are discussed. © *2001 MAIK "Nauka/Interperiodica".*

PACS numbers: 31.15.-p; 32.30.-r; 31.25.-v; 42.50.-p

The situation in which optical transitions occur between a certain pair of atomic energy levels (as a rule, ground level E_g and one of the excited levels E_e), while the remaining levels are not involved in the physical processes, is a standard situation in optics. The notion of a two-level system (TLS) and the pseudospin concept provide a convenient tool for the description of such situations; the pair of atomic energy levels of interest is treated as the eigenvalues and eigenstates of a Hamiltonian

$$H_S^j = \hbar\omega_0\hat{S}_j^Z, \quad \hbar\omega_0 = E_e - E_g, \tag{1}$$

which has the form of the Zeeman energy operator of a particle with effective pseudospin $S_j = 1/2$ [1]. It is customarily thought that the interaction between TLSs has the form $U_{jk}^x S_j^x S_k^x + U_{jk}^y S_j^y S_k^y$, because the electric dipole transition operator in the space of the E_g and E_e eigenstates has only nondiagonal matrix elements. However, this is valid only in the dipolar approximation. Below, it is demonstrated that the inclusion of electric quadrupole interaction [2]

$$V_2 = -\frac{e}{2c}\sum_{j=1}^{N}\sum_{\alpha,\beta} r_{\alpha j} r_{\beta j}\frac{\partial}{\partial R_{\alpha j}}\frac{\partial A_\beta(\mathbf{R}_j, t)}{\partial t} \tag{2}$$

in the Pauli Hamiltonian leads to the appearance of "energy" pseudospin components S_j^z for the indirect interaction [$R_{\alpha j}$ and $r_{\alpha i}$ are the α components of the radius-vectors of the nucleus j and the element of electron density of the optical shell of atom j, respectively, and $A_\beta(\mathbf{R}_j, t)$ is the β component of the vector potential of radiation field in the interaction representation].

The structure of the Hamiltonian of two subsystems in the problem of indirect interaction can generally be represented as

$$H = H_0 + V_{sf}, \quad H_0 = H_S + H_f, \tag{3}$$

where H_S is the Hamiltonian of a dynamic subsystem consisting of the noninteracting particles, H_f is the Hamiltonian of the interaction-mediating field, and V_{sf} is the operator of interaction between the particles of two subsystems.

The method of calculating the indirect interactions [3, 4] includes two steps and is based on the assumption that the matrix elements of the operators satisfy the inequality

$$|V_{sf}| \ll |H_0|.$$

The first step consists of the transition to the new representation using unitary transformation $U = \exp\{-L\}$, where L is the anti-Hermitian operator satisfying the condition

$$V_{sf} + [H_0, L] = 0. \tag{4}$$

As a result, the Hamiltonian H takes, in the new representation, the form

$$H \longrightarrow \tilde{H} = H_S + H_f + \frac{1}{2}[V_{sf}, L] + O(V_{sf}^3), \tag{5}$$

i.e., it gets rid of the terms linear in V_{sf}. The solution of the operator Eq. (4) is

$$\begin{aligned} L &= \frac{1}{i\hbar}\lim_{\varepsilon\to 0}\int_{-\infty}^{0} e^{\varepsilon t} V_{sf}(t)\,dt, \\ V_{sf}(t) &= \exp\{i(H_S + H_f)t/\hbar\}V_{sf} \\ &\quad\times \exp\{-i(H_S + H_f)t/\hbar\}. \end{aligned} \tag{6}$$

0021-3640/01/7405-0255$21.00

Therefore, the generator L of unitary linear transformation is of the order $L \sim |V_{sf}/|H_0|$.

The second step consists of averaging Eq. (5) for $\tilde{H}$ over the states of the interaction-mediating field, so that the second-order term

$$W = \frac{1}{2}\langle [V_{sf}, L]\rangle \tag{7}$$

in the perturbative expansion of Eq. (5) ceases to depend on the variables of the electromagnetic field but retains the dependence on the pseudospin operators of particles and, thus, acquires the meaning of the operator of their indirect interaction.

Let us represent the Pauli Hamiltonian of an atom in an electromagnetic field as

$$H = H_0 + V_1 + V_2, \quad H_0 = H_{0a} + H_{0ph}. \tag{8}$$

Here, H_{0a} is the Hamiltonian of an isolated atom [instead of H_{0a}, its projection (1) on the subspace of the TLS states will be used below], H_{0ph} is the Hamiltonian of the radiation field, and

$$V_1 = -\sum_j (\mathbf{d}_j \cdot \mathbf{E}(\mathbf{R}_j, t)),$$
$$\mathbf{E}(\mathbf{R}_j, t) = -\frac{1}{c}\frac{\partial \mathbf{A}(\mathbf{R}_j, t)}{\partial t}, \tag{9}$$

where $\mathbf{d}_j = e\mathbf{r}_j$ is the electric dipole moment of the $E_g \longleftrightarrow E_e$ transition of atom j. The operator V_2 is given by Eq. (2). In what follows, the role of operators H_s, H_f, and V_{sf} [Eq. (3)] is played by the operators (1), H_{0ph}, and V_2, respectively. In the secondary quantization representation, the operators H_{0ph} and V_2 have the form

$$H_{0ph} = \hbar\sum_{k\mu}\omega_k\left(a^+_{k\mu}a_{k\mu} + \frac{1}{2}\right), \tag{10}$$

$$V_2(t) = -\frac{e}{2}\sqrt{\frac{2\pi\hbar}{V}}\sum_i\sum_{\alpha,\beta} r_{\alpha j} r_{\beta j} \times \sum_{k,\mu} G^{\alpha\beta}_{k\mu}(\mathbf{R}_j)[a_{k\beta}(t) - a^+_{-k\mu}(t)],$$
$$G^{\alpha\beta}_{k\mu}(\mathbf{R}_j) = k^\alpha e^\alpha_{k\mu}\sqrt{\omega_k}e^{i\mathbf{k}\mathbf{R}_j}, \tag{11}$$

where $a^+_{k\mu}(t)$ and $a_{k\mu}(t)$ are the operators of creation and annihilation of a photon with momentum $\hbar\mathbf{k}$, polarization μ, and polarization vector $\mathbf{e}_{k\mu}$ [5, 6].

Using operators (1), (10), and (11) in the formalism described above, one can obtain the following expression for the operator of indirect interaction:

$$W = \hbar\sum_{ij} U^z_{ij} S^z_i S^z_j. \tag{12}$$

It follows that the coupling of the TLS to the radiation field via the quadrupole interaction V_2 gives rise to the exchange interaction of Ising type.

The potential of this interaction

$$U^z_{ij} = \frac{e^2(\rho_z - \rho_z)^2}{2\pi\hbar}\int_0^\infty k^4\left\{\frac{1}{15}j_0(kP)P_0\cos(\Theta_R) - \frac{1}{21}j_2(kP)P_2(\cos(\Theta_R)) - \frac{4}{35}j_4(kP)P_4(\cos(\Theta_R))\right\}dk, \tag{13}$$

where $\rho_\alpha = \langle \Psi_e|r^2_\alpha|\Psi_e\rangle - \langle \Psi_g|r^2_\alpha|\Psi_g\rangle$, $j_n(z)$ are the Bessel spherical functions, $P(\cos\Theta_R)$ is the Legendre polynomial, Θ_R is the polar angle between the crystal axis z and the vector $\mathbf{R}_{ij} = \mathbf{R}_j - \mathbf{R}_i$, and $R = |R_{ij}|$, is obtained after the transition from the summation to integration over the photon wave vectors.

Equation (13) can further be simplified on the basis of the following considerations. The upper limit of integration, unfortunately, cannot be extended to infinity, because the atom cannot be regarded as a point particle for the wavelengths shorter than atomic size, so that the form chosen above for the interaction V_{sf} becomes scarcely valid. In our case, it is reasonable to integrate to $k_{\max} = 2\pi/r_a$, where r_a is the atomic radius. Next, the condition $k_{\max}R > 1$ is always fulfilled, signifying that the interatomic separation is larger than the atomic size. This enables one to use the approximation

$$j_l(z) = \frac{1}{z}\cos\left(z - \frac{\pi}{2}(l+1)\right),$$

which is valid for large arguments. These simplifications give

$$U_{ij} = \hbar^{-1}\left[\frac{2\pi e(\rho_z - \rho_x)}{R}\right]^2 \times \frac{\cos(2\pi R/r_a)}{2r_a^3}\cos^2\Theta_R\sin^2\Theta_R. \tag{14}$$

Therefore, the potential (14) oscillates and drops as R^{-2}_{ij}. This drop is caused by the fact that the photon density at the point R_j decreases for those photons which already interacted with the TLS at the point R_i. The periodic dependence is typical of many indirect interactions, among which the interaction between nuclear spins via conduction electrons in metals is most familiar [4].

To estimate the parameters ρ_α, we choose the (1, 0, 0) and (2, 1, 1) states of the hydrogen atom [the (n, l, m) triads are indicated] as the ψ_g and ψ_e states [1]. With the hydrogen wave functions $\psi_{2,1,1}$ and $\psi_{1,0,0}$,

one has $\rho_x = \rho_y = 5r_B^2$ and $\rho_z = 11r_B^2$, where r_B is the Bohr radius. Choosing the values $r_a \sim 10^{-8}$ cm and $R \sim 10^{-6}$ cm for the other parameters, one obtains the following estimate for the Ising exchange integral: $U(R_{ij}) \approx 10^{13}$ rad/s.

For a disordered collective of TLSs in a medium, the interaction W can induce so-called inhomogeneous broadening of an optical transition, because it shifts the resonance frequency ω_0 for each atom j by a value of

$$\Delta\omega_j = \sum_i U_{ij}^z \langle S_j^z \rangle,$$

The root-mean-square value of the random variable $\Delta\omega_j$

$$\overline{\Delta\omega_j} = \frac{\sqrt{2n}}{3\sqrt{35}}\left[\left(\frac{2\pi}{r_a}\right)^3 \frac{e^2(\rho_z - \rho_x)^2}{\hbar}\right] \times \frac{\cos\{2\pi R_0/r_a\}}{\sqrt{\pi R_0}} \langle S_j^z \rangle, \quad (15)$$

can serve as a measure of the line broadening, where $\langle S_j^z \rangle$ is the temperature mean of the z component of pseudospin j at the temperature of the experiment (in general, it can be assumed to not change from point to point), R_0 is the shortest possible distance between the TLSs, and n is their concentration [7]. For $n = 10^{17}$ cm^{-3}, one has $\Delta\omega_j \approx 10^{12}$ rad/s.

The natural width of the emission line is given by the formula $\gamma = 2d^2\omega_0^2/3\hbar c^3$ [8]. For the optical frequencies $\omega_0/2\pi \sim 3 \times 10^{14}$ Hz, this gives $\gamma \approx 2 \times 10^5$ Hz, which is considerably smaller than the value obtained in this work.

A more intriguing manifestation of the Ising exchange interaction can be expected for the ordered system of TLSs in a crystal lattice. As known, the Ising magnets display additional resonance peaks if the exchange integral exceeds the natural linewidth [7]. Under these conditions, the $\Delta\omega_j$ quantities are no longer random variables but take fixed values to produce additional absorption peaks. The number of peaks depends on the number of exchange-coupled atoms. For example, in a linear Ising chain with nearest-neighbor exchange, three resonance frequencies occur at ω_0 and $\omega_0 \pm U_{ij}^z$.

The integrated intensities of these lines show an unusual temperature behavior; in particular, as the temperature approaches zero, all lines are frozen out except for one of them, whose intensity increases. Unfortunately, the separation $E_e - E_g$ between the optical energy levels is too large, so that one practically always deals with the zero-temperature limit. Because of this, a search for the additional peaks should be carried out under the nonequilibrium conditions.

The experiments of this type are well-known in magnetic resonance. Irradiation by a strong narrow-band microwave field in the region of an inhomogeneously broadened EPR line followed by sweeping the line contour with another weak field gives rise to a broad contour with a "burned hole" in it [9]. The EPR line shape undergoes intricate transformation in the course of re-establishing the equilibrium, and the relaxational properties of the object are judged from the kinetics of this process.

There is one more example. Upon the intense narrow-band saturation of a homogeneously broadened EPR line, its contour transforms in a complicated manner up to the appearance of the portions with negative absorption. A rather complicated kinetics of this process is due to the presence of a reservoir of magnetic dipole–dipole interactions and is well studied by the experimental methods [10].

To observe experimentally the Ising exchange interaction between the TLSs, a physical system should be disturbed from equilibrium, e.g., by the π pulse or intense stationary irradiation followed by sweeping the spectrum with a weak laser beam. In such a situation, one can expect that additional peaks will appear with a complicated kinetics.

We are grateful to K.M. Salikhov and V.N. Lisin for discussions.

REFERENCES

1. L. Allen and J. H. Eberly, *Optical Resonance and Two-Level Atoms* (Wiley, New York, 1975; Mir, Moscow, 1978).
2. R. Loudon, *The Quantum Theory of Light* (Clarendon Press, Oxford, 1973; Mir, Moscow, 1976).
3. H. Frohlich, Phys. Rev. **79**, 845 (1950).
4. M. A. Ruderman and C. Kittel, Phys. Rev. **96**, 99 (1954).
5. A. S. Davydov, *Quantum Mechanics* (Fizmatgiz, Moscow, 1963; Pergamon, Oxford, 1976).
6. W. H. Louisell, *Radiation and Noise in Quantum Electronics* (McGraw-Hill, New York, 1964; Nauka, Moscow, 1972); W. H. Louisell, *Quantum Statistical Properties of Radiation* (Wiley, New York, 1973).
7. A. R. Kessel and G. O. Berim, *Magnetic Resonance of Ising Magnetics* (Nauka, Moscow, 1982); G. O. Berim, M. M. Zaripov, and A. R. Kessel, Zh. Éksp. Teor. Fiz. **66**, 734 (1974) [Sov. Phys. JETP **39**, 355 (1974)]; Fiz. Tverd. Tela (Leningrad) **17**, 2622 (1975) [Sov. Phys. Solid State **17**, 1744 (1975)].
8. A. N. Oraevskiĭ, Usp. Fiz. Nauk **164**, 415 (1994) [Phys. Usp. **37**, 393 (1994)].
9. V. A. Atsarkin, *Dynamic Polarization of Nuclei in Solid Dielectrics* (Nauka, Moscow, 1980).
10. V. A. Atsarkin and M. I. Rodak, Usp. Fiz. Nauk **107**, 3 (1972) [Sov. Phys. Usp. **15**, 251 (1972)].

Translated by V. Sakun

JETP Letters, Vol. 74, No. 5, 2001, pp. 258–261. Translated from Pis'ma v Zhurnal Éksperimental'noĭ i Teoreticheskoĭ Fiziki, Vol. 74, No. 5, 2001, pp. 287–290.

Observation of Dynamic Effects in the Percolation Transition in a "Nonwetting Liquid–Nanoporous Body" System

V. D. Borman, A. A. Belogorlov, A. M. Grekhov, V. N. Tronin, and V. I. Troyan*

Moscow Institute of Engineering Physics, Kashirskoe sh. 31, Moscow, 115409 Russia

** e-mail: mal@park.mephi.ru*

Received July 18, 2001

Filling of a nanoporous body with liquid metal upon pulsed pressure buildup to a level far exceeding the percolation-threshold critical pressure was experimentally studied. The onset of the oscillating filling regime was observed. It disappears on bringing pressure down to a value lower than the percolation-transition critical pressure and on increasing the characteristic time of pressure buildup above threshold. A model is suggested allowing the explanation of the observed effects. © *2001 MAIK "Nauka/Interperiodica".*

PACS numbers: 64.60.Ak

At present, the formation of metal structures in a porous body with nanometer-sized pores attracts particular interest both from the standpoint of fundamental science and because of the possible use of such structures in nanotechnologies (see, e.g., [1, 2]). One of the methods of fabricating such structures consists in the filling of nanopores with a liquid metal at a pressure higher than the Laplace pressure (P_L) [3]. The process of filling a nanoporous body with a nonwetting liquid metal can be used for the absorption and accumulation of mechanical energy [3]. The percolation theory adequately describes this process [4]. In this theory, the filling process is treated as the growth of fractal clusters of filled pores. Experimentally, this is confirmed by the "devil staircase" effect [5] and the formation of "viscous fingers" during the filling of a porous body [4]. The hysteresis and "nonleakage" effects of a nonwetting liquid can also be explained by the theory of percolation with energy threshold [6].

In this work, the filling of a nanoporous body with a liquid metal upon pulsed pressure buildup to a level far exceeding the percolation threshold pressure p_c was studied experimentally. In compliance with the well-known filling theory [4], one could have expected that the filling speed increased while the filling time decreased with an increase in $(p - p_c)$ at $p > p_c$. However, we observed the onset of oscillating filling regime, which disappeared after bringing the pressure down to the below-threshold value p_{c1} ($p_{c1} > p_c$) and increasing the characteristic time t_{c1} of pressure buildup to the above- threshold value ($t_{1c} > t_1$).

Below, a physical model is proposed which explains the observed effects. Following [6, 7], the filling of a porous body can be treated as a process of "interaction" between the fractal clusters of filled and accessible, at a given pressure ($p = P_L$), pores in the course of fluid leakage from the body surface through the transitions from the clusters of filled pores to the adjacent cluster of accessible pores. As the percolation threshold is approached, the correlation length and the cluster size characteristic increase. This must lead to an increase in the characteristic time (τ) of interaction between clusters and an increase in the relaxation time of the system. For this reason, if the pressure-buildup characteristic time (t_1) is comparable with the relaxation time, then the percolation transition in the nonlinear system considered will be accompanied by the dynamic effects.

In our experiments, a liquid Wood's alloy (T_m = 72°C) and a Silokhrom SKh-1.5 porous body were placed in a high-pressure chamber. The mass and size of the Silokhrom grains were $m \cong 1$ g and 300 μm, respectively. The pore diameter in Silokhrom SKh-1.5 ranged from 130 to 260 nm. The pressure in the chamber was produced by mechanical action on a rod that could enter the chamber through gaskets. A decrease in volume of the Wood's alloy–Silokhrom system upon moving the rod inside the chamber produced excessive pressure. The change in volume was measured using a displacement pickup. The pressure was measured by a strain gauge that was mounted on a support under the high-pressure chamber. The gauge could detect strength from 0 to 1000 kg in the frequency range up to 10 kHz with an accuracy of ≈10%. The filling critical pressure was determined from the $V(p)$ dependence of the filled pore volume on pressure p for a quasi-static pressure buildup with a characteristic time of ≈10 s. For the system under study, this value was found to be p_c = 120 atm. In the experiments with dynamic filling, the time-dependent pressure in the chamber was measured for the pulsed mechanical action on the chamber rod. The measured compressibility of Silokhrom SKh-1.5 was $\chi \cong 1.6 \times 10^{-3}$ atm^{-1}. Since the compressibility of the chamber with volume $V_{ch} \approx 120$ cm^3 was $\chi \cong$

1.4×10^{-5} atm^{-1}, a change in the chamber volume filled with the Wood's alloy (the compressibility of the Wood's alloy is ~10^{-6} atm^{-1}) was vastly larger than the change in the Silokhrom volume in the dynamic experiments on the time scale of ≤10 ms with working pressure $p \approx 3 \times 10^2$ atm; i.e., $\Delta V_{ch} \gg \Delta V_S$. Because of this, the characteristics of a pressure pulse in the chamber were determined in special experiments, in which the chamber was filled only with the Wood's alloy. When studying the filling dynamics of the porous body, the maximal pressure in the chamber was p_0 = 240–600 atm, i.e., much higher than the critical pressure of the system of interest. The characteristic time t_1 of reaching the maximal pressure was varied in these experiments within 4–11 ms, and the characteristic time of pressure release was 5–10 ms.

The $p(t)$ curves for the pressure in the chamber filled with the Wood's alloy and porous body is shown in Fig. 1b. The corresponding $p_0(t)$ curves for the chamber filled only with the Wood's alloy is shown in Fig. 1a. For the short p_0 pulse ($p_{0\,max} \simeq 450$ atm, upper panel in Fig. 1a), periodic oscillations with the characteristic period $T \approx 1$ ms and amplitude $\delta p \sim 20 \pm 2$ atm appear in the $p(t)$ curve (upper panel in Fig. 1b). It is seen from the middle panel in Fig. 1b that, at a fixed duration, an increase in the amplitude of pulse p_0 (middle panel in Fig. 1a) gives rise to the additional harmonics in the $p(t)$ dependence. As the p_0 pressure amplitude decreases and the pulse duration increases (lower panel in Fig. 1a), the oscillations in the $p(t)$ curve disappear (lower panel in Fig. 1b). The instants of time t_2 (Fig. 1b) corresponding to the completion of filling the porous body with the Wood's alloy were determined from the momentum conservation law. One can see that the oscillations are observed at $t < t_2$. At $t > t_2$, the liquid leaks away from the porous body. At these times, the $p(t)$ curves also display oscillations (upper and middle panels in Fig. 1b). It follows from the data in Fig. 1 and from the additional experiments that, at a fixed duration of the p_0 pulse, there is a critical pressure $p_{0c} \cong 300$ atm below which the filling oscillations are absent. Note that the increase in the p_0 pulse duration from 10 to 20 ms also results in the disappearance of oscillations.

Let us discuss a possible mechanism of the observed dynamic effects. According to [6, 7], the filling dynamics for a porous body filled with a nonwetting fluid can be described using the kinetic equation for the distribution function of the fractal clusters of filled pores. It is known [6] that, at a given pressure p_0, all pores in a porous body can be divided into accessible (to filling) and inaccessible ones. Filling of a nanoporous body with a fluid at a given pressure proceeds through filling only the accessible pores. Within the framework of this approach, the filling process in the vicinity of the percolation threshold is treated as the interaction between the fractal clusters of filled and accessible pores.

For a qualitative description of the experimentally observed oscillations in dynamic pore filling, a simple model is proposed below, which allows for the salient features of cluster interaction within the macroscopic approach. With this approach, a change dV/dt in the volume of a porous body filled with fluid is proportional both to the filled volume $V(t)$ and to the volume V_z of accessible but, as yet, not filled pores. We will assume that the characteristic time of formation of the accessible pores is small compared to that of the filled pores. In this case, the accessible volume depends only on the external pressure and the total volume of filled pores. For a given pressure p_0, the volume $V_z(t)$ of unfilled pores at time t is determined by the difference between the accessible volume at zero time V_z^0 and the volume of filled pores at time t; i.e., $V_z(t) = V_z^0 - V(t)$. Therefore, for the time variation of the filled volume in a porous body, one has:

$$\frac{dV}{dt} = \Lambda V(V_z^0 - V) = \frac{1}{\tau}\frac{V}{V_z^0}(V_z^0 - V). \qquad (1)$$

Here, $\tau = (\Lambda V_z^0)^{-1}$ is the filling time of an elementary volume equal to the volume of a cluster with a size on the order of the correlation length $\xi(p_0) = R(\theta(p_0) - \theta_c)^{-\nu}$ ($\nu = 0.89$ [8]) and consisting of the accessible though not filled pores; $\theta(p_0)$ is the fraction of accessible pores at a pressure of p_0; and θ_c is the critical fraction of accessible pores, for which the infinite cluster of accessible pores arises. For the 3D systems, $\theta_c \approx 0.16$ [8]. The expression for the accessible volume can be written as

$$V_z^0 = \frac{V_0(\theta(p_0) - \theta_c)}{1 - \theta_c}, \qquad (2)$$

where V_0 is the volume of pores in a porous body. The difference $1 - \theta_c$ in the denominator accounts for the fact that all pores are accessible at $\theta(p_0) = 1$.

Using the Poiseuille formula [9], one can obtain the following estimate for the average filling time of one pore:

$$\tau_n \approx \frac{32\eta}{3p}\nu(p_0), \quad \nu(p_0) = \left(\frac{\langle R\rangle}{a}\right)^4,$$

$$\langle R\rangle = \int_{R(p_0)}^{\infty} F(R)RdR.$$

Here, $\langle R\rangle$ is the average pore radius in the porous medium, a is the average pore radius in the region where two pores are in contact, η is the fluid viscosity, $F(R)$ is the normalized (to unity) pore-size distribution function, and $R(p_0)$ is the lower limit to the pore radii satisfying the energetic condition for accessibility [6].

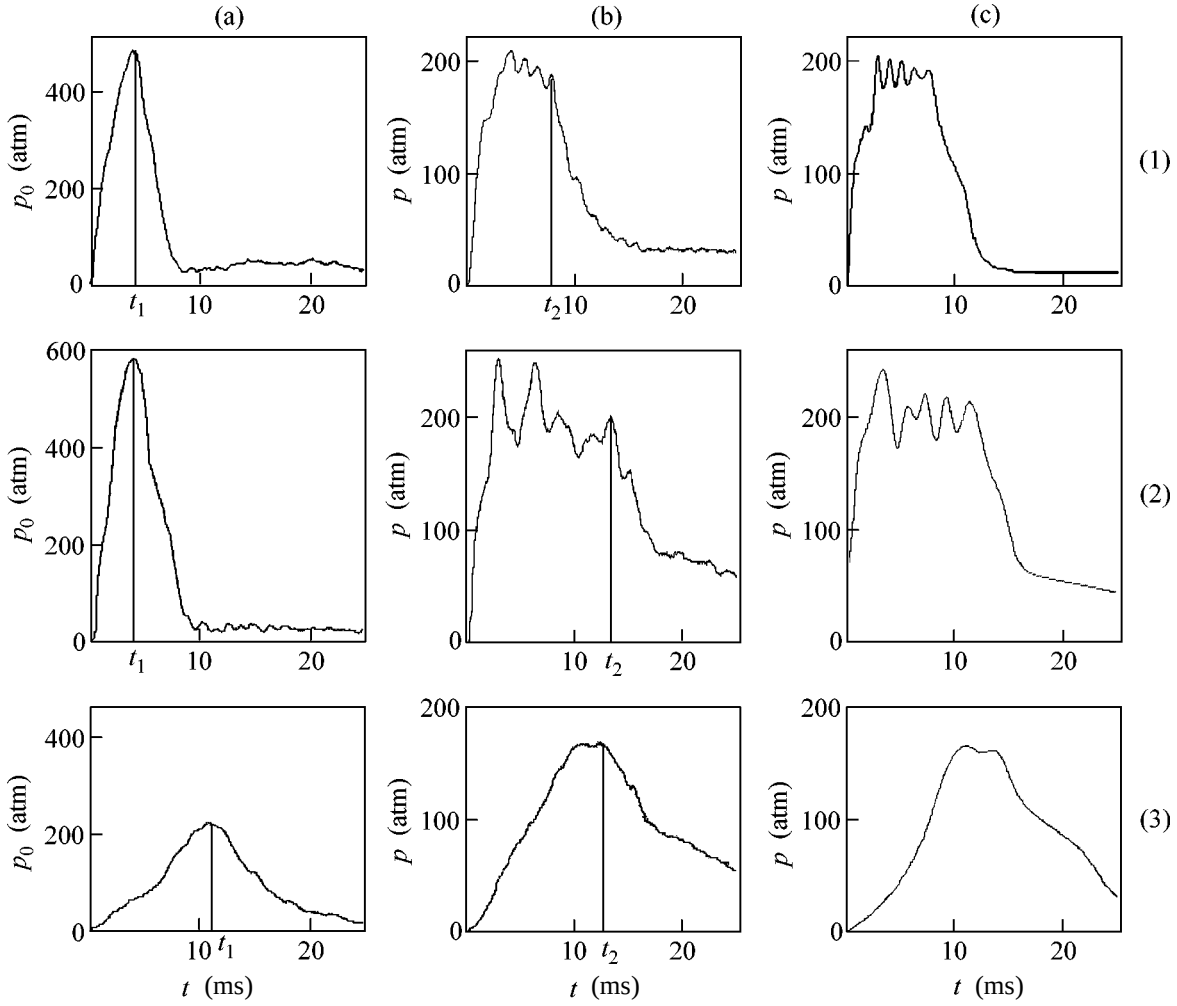

Fig. 1. Plots of pressure in the chamber vs. time: (a) a column filled with a liquid Wood's alloy; (b) a column filled with a liquid Wood's alloy and a porous body (Silokhrom SKh-1.5, 1 g); and (c) numerical simulation. The panels correspond to different values of $p_{0\,\max}$ and τ (see text).

Note that the ratio $(\langle R\rangle/a)^4$ is equal, by order of magnitude, to the inverse squared pore connectivity coefficient [6]. Therefore, after introducing the new variable $x(t) = V(t)/V_z^0$, Eq. (1) for the filled volume reduces to

$$\frac{dx}{dt} = \frac{x(1-x)}{\tau}, \tag{3}$$

where

$$\tau = \tau_n \beta^{-1}, \quad \beta \cong \frac{\theta(p_0) - \theta_c}{1 - \theta_c}.$$

Note that the filling characteristic time τ diverges in the vicinity of the percolation threshold. For the system studied, one has the following estimates: $\eta \cong 10^{-3}$ Pa s, $\langle R\rangle \approx 100$ nm, $\langle R\rangle/a \approx 3$, $\theta(p_0) - \theta_c \approx 10^{-3}\theta_c$ for $\xi(p_0) \approx L$ [6], and the grain size is $L \approx 300$ μm. The corresponding τ value is $\approx 10^{-3}$ s. The characteristic time of our measurements is comparable to the filling characteristic time τ. In this case, differential Eq. (1) should be replaced by its discrete analogue. One then obtains from Eq. (3):

$$y_{n+1} = (1 + \gamma\beta) y_n (1 - y_n),$$
$$y_n \equiv \frac{\gamma\beta}{1 + \gamma\beta} x_n, \quad \gamma \simeq \frac{\langle R^4\rangle}{\langle R\rangle^4} \gtrsim 2. \tag{4}$$

This equation is a familiar Feigenbaum transformation [10] which leads to the appearance of time oscillations through the period doubling scenario. However, contrary to the well-known results of the Feigenbaum period-doubling scenario, the parameter β, which is responsible for the period doubling in Eq. (4), itself depends on time because of the $p_0(t)$ dependence and, hence, depends on the quantity $\theta(p_0(t))$. The results of the numerical solution of this equation are presented in Fig. 1c.

In solving Eqs. (4), the experimentally measured quasi-static dependence $V(p)$ of the filled volume on pressure and the time dependence $p_0(t)$ of the pressure pulse (Fig. 1a) were used. One can see from the upper panel in Fig. 1c that the calculated and experimental curves are in qualitative agreement with each other. It is seen from the middle panel in Fig. 1c that the increase in the p_0 pulse amplitude at a fixed pulse duration leads to a more complicated oscillation pattern, in qualitative agreement with the experimentally observed dependence $p(t)$ (middle panel in Fig. 1b). It should be noted that, according to the calculations, the filling oscillation pattern changes appreciably even upon a small (≤10%) change in the p_0 pulse shape. An increase in the pressure-buildup characteristic time of $p_0(t)$ results in the disappearance of oscillations (lower panel in Fig. 1c) because of a decrease in the parameter β in Eq. (4) and, hence, the transition from the discrete filling regime to the continuous one.

Thus, the oscillations in the model suggested can appear only if a pressure higher than its percolation-transition critical value is achieved [i.e., $\theta(p_0) > \theta_c$] and if the pressure-buildup characteristic time becomes comparable to the pore-filling characteristic time τ given by Eq. (3).

In summary, the observed dynamic effects accompanying the pore filling with a nonwetting liquid have been qualitatively explained by a simple macroscopic model which allows for the interaction between the accessible and filled pores of a porous body following the pattern of the Feigenbaum-type scenario. The presence of a percolation threshold and the divergence of the compressibility [6] of a "nonwetting liquid–porous body" system allow the filling process to be treated as a physical phase transition. For this reason, the observed dynamic effects can be interpreted as processes appearing upon a strong pressure supersaturation on the time scale of the formation of a cluster of filled pores with it's size on the order of the correlation length close to the grain size in the porous body. On this time scale, the filling process has an essentially discrete character.

We are grateful to L.A. Maksimov, E.V. Gribanov, and V.V. Konyukov for their interest and assistance in this work. This work was supported by the INTAS, grant no. 99-01744.

REFERENCES

1. V. G. Balakirev, V. N. Bogomolov, V. V. Zhuravlev, *et al.*, Kristallografiya **38** (3), 111 (1993) [Crystallogr. Rep. **38**, 348 (1993)].
2. Y. Maeda, Phys. Low-Dimens. Struct. **10**, 1 (1997).
3. V. N. Bogomolov, Phys. Rev. B **51**, 17040 (1995).
4. M. Sahimi, Rev. Mod. Phys. **65**, 1393 (1993).
5. A. H. Thompson, A. J. Katz, and R. A. Raschke, Phys. Rev. Lett. **58**, 29 (1987).
6. V. D. Borman, A. M. Grekhov, and V. I. Troyan, Zh. Éksp. Teor. Fiz. **118**, 193 (2000) [JETP **91**, 170 (2000)].
7. A. A. Abrikosov, Pis'ma Zh. Éksp. Teor. Fiz. **29**, 72 (1979) [JETP Lett. **29**, 65 (1979)].
8. M. B. Isichenko, Rev. Mod. Phys. **64**, 961 (1992).
9. L. D. Landau and E. M. Lifshitz, *Course of Theoretical Physics*, Vol. 6: *Fluid Mechanics* (Nauka, Moscow, 1986; Pergamon, New York, 1987).
10. G. G. Malinetskiĭ, *Chaos. Structures. Computational Experiment* (Éditorial, Moscow, 2000).

Translated by V. Sakun

JETP Letters, Vol. 74, No. 5, 2001, pp. 262–266. Translated from Pis'ma v Zhurnal Éksperimental'noĭ i Teoreticheskoĭ Fiziki, Vol. 74, No. 5, 2001, pp. 291–295.

Critical State of Josephson Medium

N. D. Kuz'michev

Ogarev Mordovian State University, ul. Bol'shevistkaya 68, Saransk, 430000 Russia

Received May 11, 2001; in final form, July 20, 2001

A model of the critical state of a Josephson medium is developed on the basis of the Sonin theory of averaged Josephson medium. The model is used to explain the experimental data on the differential magnetic susceptibility $\chi_d(H)$ and magnetoresistance $R(H)$ of polycrystalline $YBa_2Cu_3O_{7-x}$ samples in fields $H <$ 100 Oe. © *2001 MAIK "Nauka/Interperiodica".*

PACS numbers: 74.50.+r; 74.80.Bj

At present, there is no clear understanding of the microscopic pattern of magnetic-field penetration into a granular high-temperature superconductor (HTSC). Semicrystalline granular HTSCs with Josephson (weak) contacts between grains display a series of anomalous properties in low magnetic fields $H <$ 10–50 Oe, e.g., nonlinearity and, simultaneously, the absence of magnetization hysteresis [1–5]. This fact contradicts both the Meissner effect (linear magnetization) and the well-known critical-state model [6–8], for the latter assumes a hysteretic behavior of superconductor magnetization. Other models of the magnetic properties of polycrystalline HTSCs, e.g., the superconducting glass model [7, 9] and the model of Josephson loops [1, 3, 10] also inadequately describe the experiment.

In this work, a model of the critical state of an averaged Josephson medium is developed which adequately describes the experimental data obtained earlier in [11–13] for the differential magnetic susceptibility and magnetoresistance of polycrystalline $YBa_2Cu_3O_{7-x}$ samples.

1. Theoretical model. To describe the penetration of a nonstationary magnetic field into a system of weak contacts in a granular HTSC, the well-known model of averaged Josephson medium [14, 15] and the concept of the critical state of a hard type-II superconductor [6] are used in this work.

According to the model of averaged Josephson medium, the supercurrent carriers in granular HTSC are in the coherent state (see, e.g., [9, 14]). The coherent state is characterized by the order parameter (wave function) $\Psi = \sqrt{n}e^{i\theta}$, where n is the effective concentration of supercurrent carriers and θ is their phase. Let us consider a sample of granular HTSC placed in an external magnetic field H. If $H < H_{c1J}$ (H_{c1J} is the lower critical field of weak contacts), then the static magnetic field penetrates into the array of weak contacts over a Josephson depth λ_J (for HTSC, $\lambda_J \sim$ 0.01–10 mm [7]). At present, no exact estimates exist for the value of H_{c1J}). The values from 0.001 to 100 Oe are reported in different publications (see, e.g., [7, 9, 14]). Since the magnetic flux is trapped in HTSC samples due to vortex pinning, one may assume that H_{c1J} is equal to the magnetization irreversibility field H_{irr} ($H_{irr} \sim$ 10–70 Oe [11, 13]). This leads to the following estimates. The values of λ_J, H_{c1J}, and j_{cJ} are related to each other by [16, 17]

$$H_{c1J} = \frac{4}{\pi}\lambda_J j_{cJ} \sim \lambda_J j_{cJ}. \quad (1)$$

Setting $j_{cJ} \sim$ 0.1–10 A/cm^2 [7], one obtains an estimate $\lambda_J \sim 1$–10^3 cm, which is inconsistent with the literature data ($\lambda_J \sim$ 0.01–10 mm). One has to assume that either $j_{cJ} \sim 10^3$–10^5 A/cm^2 or $H_{c1J} \sim 10^{-2}$–10^{-4} Oe. The latter is in agreement with the hypervortex model [14, 15]. At $H_{c1J} \sim 10^{-4}$ Oe, the hypervortex diameter of ~0.5 mm is of a macroscopic size. In what follows, the hypervortex model will be adopted.

In the critical-state model [6–8], an alternating external magnetic field penetrates into a sample in the form of low-mobile hypervortices [14, 15] and, according to the Maxwell equations, creates in the system of weak contacts an electric field $\mathbf{E}$ which induces a superconducting screening current $\mathbf{j}$:

$$\mathrm{curl}\mathbf{H} = j\frac{\mathbf{E}}{E}. \quad (2)$$

In a Josephson medium, the screening supercurrent density [Eq. (2)] is proportional to the Josephson critical current I_{cJ}, which is given either by the Ambegaokara–Baratoff formula (S–I–S junction) or by the formula for the S–N–S junctions [18]. In both cases, the

net result is the same. Below, the Ambegaokara–Baratoff formula is used for convenience [16, 17]:

$$I_{cJ} = \frac{\pi\Delta(T)}{2eR_n}\tanh\left[\frac{\Delta(T)}{2kT}\right], \quad (3)$$

where $\Delta(T)$ is the superconducting gap at temperature T, e is the electron charge, k is the Boltzmann constant, and R_n is the normal-state resistance of the junction [$R_n = \rho_n(l/S)$, where ρ_n is the junction resistivity, l is its length, and S is its cross-section].

The screening current j in a cylindrical sample is given by the formula

$$j = \left\langle j_{cj}\left|\frac{\sin(\pi\Phi/\Phi_0)}{\pi\Phi/\Phi_0}\right|\right\rangle\frac{\partial\Theta}{\partial\varphi}. \quad (4)$$

Here, the angular brackets $\langle\ldots\rangle$ denote the averaging over all Josephson contacts in the sample, $\Phi = \oint\mathbf{A}d\mathbf{l}$ is the magnetic flux entering the sample in the form of vortices (Josephson's or hypervortices), $\mathbf{A}$ is the magnetic-field vector potential (magnetic field is concentrated inside the vortex), $\Phi_0 = \pi\hbar/e = 2.07\times10^{-7}$ Gs cm^2 is the magnetic-flux quantum, Θ is the phase of screening current, and φ is the polar angle in the cylindrical coordinate system. The Josephson critical current density j_{cj}, according to Eq. (3), is

$$j_{cJ} = \frac{\Delta(T)}{4e\rho_n r}\tanh\left[\frac{\Delta(T)}{2kT}\right], \quad (5)$$

where ρ_n is the normal-state resistivity of a Josephson medium, and r is the running radius of the cylindrical sample. Indeed, the resistance of a ring layer of radius r, width a, and height b is $R = \rho(2\pi r/ab)$. One has $I \sim 1/R$ for the ring current and $j = I/ab \sim 1/2\pi\rho r$ for the current density. The resulting expression for the screening supercurrent density is

$$\begin{aligned} j &= \left\langle\frac{\Delta}{4e\rho_n r}\tanh\left(\frac{\Delta}{2kT}\right)\left|\frac{\sin(\pi\Phi/\Phi_0)}{\pi\Phi/\Phi_0}\right|\right\rangle\frac{\partial\Theta}{\partial\varphi} \\ &\approx \pm\frac{\Delta}{4\pi e\rho_n r}\tanh\left(\frac{\Delta}{2kT}\right). \end{aligned} \quad (6)$$

In Eq. (6), it is taken into account that $\langle|\sin(\pi\Phi/\Phi_0|\rangle \sim 1$ and $|\partial\Theta/\partial\varphi| = \Phi/\Phi_0 = N$ (N is the number of vortices entering the sample). The sign of $\partial\Theta/\partial\varphi$ depends on the direction of sweeping the external magnetic field, i.e., on $\partial H/\partial t$ and on the direction of the magnetic-field vector $\mathbf{H}$.

It follows from Eq. (6) that $j \propto n\Delta^2/rkT_c$ in the vicinity of T_c ($T < T_c$). The Ambegaokara–Baratoff formula (3) for $I_c(T)$ coincides, to a constant factor, with the Abrikosov–Gor'kov formula for the temperature-dependent supercurrent carrier concentration $n(T)$ [17, 18]. Accordingly, $|\Psi|^2 \propto n\Delta^2/(kT_c)^2$ and the shielding current (6) is

$$\mathbf{j} = \frac{e\hbar}{mi}(\Psi^*\nabla\Psi - \Psi\nabla\Psi^*). \quad (7)$$

According to Eq. (7), the critical-state equation (2) for a long cylinder is written as

$$\frac{\partial H_z}{\partial r} = \frac{e\hbar n}{mr}\frac{\partial\Theta}{\partial\varphi}. \quad (8)$$

This equation is an alternative form of Eq. (6). As was pointed out above, $|\partial\Theta/\partial\varphi| = N$ ($\sim H$) and $n \sim 1/N$ ($\sim 1/H$), because the "paramagnetic" hypervortices "take away" a part of the supercurrent carriers which are involved in the formation of a macroscopic screening supercurrent ($|\Psi|^2|\nabla\varphi| \sim j = \text{const}$). As a result, the right-hand side of Eq. (8) is independent of H, and one must put $|\partial\Theta/\partial\varphi| = 1$ in Eq. (8). Bearing Eqs. (6) and (8) in mind, let us introduce the notation

$$H_p = \frac{e\hbar n}{m} = \frac{\Delta}{4\pi e\rho_n}\tanh\left(\frac{\Delta}{2kT}\right).$$

In the model suggested, the equations for field penetration into the array of weak contacts uniformly filling the volume of a long cylinder ($L \gg R$, where L is the cylinder length and R is its radius; the magnetic field is aligned with the cylinder axis) and the volume of an "infinite" slab (the magnetic field is aligned with the z axis parallel to the slab plane) have, respectively, the form

$$\frac{\partial H_z}{\partial r} = \frac{H_p}{r}, \quad (9)$$

$$\frac{\partial H_z}{\partial x} = H_p\frac{\partial\Theta}{\partial y}, \quad (10)$$

where $\partial\Theta/\partial y \cong \pm\pi/l$ ($l \gg b$, where l is the slab length and width, b is its thickness, and $\partial\Theta/\partial y \cong +\pi/l$ for $\mathbf{H}$ aligned with the z axis).

The solution to Eq. (9) with boundary condition $H_z(R) = H$ (the axially directed external magnetic field H increases) is

$$H_z(r) = \begin{cases} H, & r > R \\ H - H_p\ln\dfrac{R}{r}, & r \le R \\ 0, & r < \rho. \end{cases} \quad (11)$$

The magnetic field does not penetrate into the cylinder region with $r < \rho = R\exp(-|H|/H_p)$. Using Eq. (11), one obtains for the cylinder magnetization

$$M = -H_p e^{-|H/H_p|}\sinh(H/H_p). \quad (12)$$

With this model, the lack of magnetization hysteresis in HTSC at low magnetic fields can be explained in a natural way. As a magnetic field rises ($H > H_{c1j}$), the

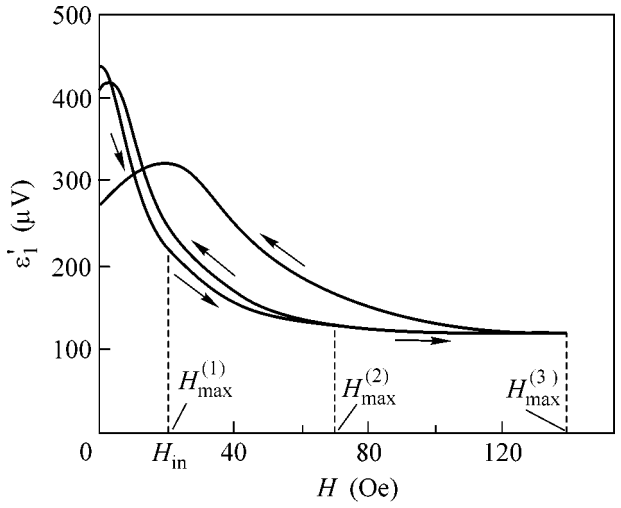

Fig. 1. Plots of $\varepsilon_1'(H)$ vs. static magnetic field for a ceramic $YBa_2Cu_3O_{7-x}$ sample no. 1 for three values of H_{max} (H_{max} is the maximal field of the magnetization cycle). The arrows indicate the cycling direction. The field $H_{max}^{(1)}$ coincides with H_{irr}.

number of hypervortices increases and their sizes diminish, similar to the Josephson vortices in the tunneling junction. The pinning of hypervortices prevents their creep. This process (transformation of the hypervortices into the intergrain Josephson vortices and intragrain Abrikosov vortices) is accompanied by the growth of the screening supercurrent which flows in the hypervortex penetration region of a Josephson medium. This process is described by Eq. (9), while the magnetization is given by Eq. (12). On reaching the field $H = H_J$, the hypervortex sizes become comparable to the average intergrain distance in the polycrystal, so that at $H > H_J$ the hypervortices are almost completely transformed into the usual Josephson vortices. If a field decreases from $H_{max} < H_J$, the process is reversed (the hypervortex size increases and its number decreases). This process is accompanied by a decrease in the screening supercurrent and also obeys Eqs. (9) and (12).

In contrast to the classical hard type-II superconductors, the hysteretic behavior of magnetization upon reversing the direction of sweeping the magnetic field in a Josephson medium is energetically unfavorable for HTSC polycrystals. Indeed, the Abrikosov vortices with a core of radius $\sim\xi$ (coherence length) are surrounded by a vortex current of radius $\sim\lambda$ (London penetration depth) and virtually do not change their size with magnetic field. This fact is manifested in the magnetic properties of superconductors as follows. The pinning of Abrikosov vortices by various imperfections in a hard type-II superconductor gives rise to the persistent screening supercurrent in the sample (critical state) [8]. As the field increases to $H_{max} > H_{c1}$ (lower critical field), the screening current flows in the vortex penetration region at a depth of ρ. The free energy of this state is determined by the energies of vortices, screening current, and their interaction. This state is unstable [8]. Its stability is maintained by the vortex pinning. As the field decreases from H_{max} to $H_1 > H_{c1}$, a current directed in opposition to the initial current is induced, according to Eq. (2), at the periphery of the sample at a depth of $\rho_1 < \rho$. Because of this, the sample of radius R is divided into two regions ($\rho < r < \rho_1$ and $\rho_1 < r < R$) with oppositely directed screening supercurrents. Since the superconductor magnetization is determined by these currents, it will display a hysteretic behavior. The energy of the hysteretic state is higher, because a positive energy of interaction between the oppositely directed screening currents is added to the initial energy, resulting in a lower stability of this state.

Contrary to the Abrikosov vortices, the hypervortices and the Josephson vortices change their size with changing magnetic field. That is, a degree of freedom exists due to which the hypervortices can adjust themselves to the external magnetic field and form a stable critical state of lower energy. Because of this, the magnetization hysteresis is absent in the Josephson medium containing hypervortices. As a result, the screening supercurrent arising upon field buildup and having smaller penetration depth, $\rho_2 < \rho$, is the only one that remains in the sample. Therefore, the hypervortices increase in size in the course of a field decrease and leave the sample, thereby reducing the penetration depth of the initial screening current.

This process is also described by Eqs. (9) and (12), which do not account for the hysteresis. As the field H decreases to zero, a trapped magnetic field $H \approx H_{c1J} \sim 10^{-1}$–$10^{-4}$ Oe, which is much lesser than the geomagnetic field, may remain in the sample. In magnetic fields $H > H_J$, some of the Josephson vortices, contrary to the hypervortices, may creep in the intergrain volume upon passing current through the polycrystalline sample. If the field is decreased from $H_{max} > H_J$, then the magnetization hysteresis will be observed. This is so because the formation of hypervortices from the Josephson vortices requires energy for overcoming a potential barrier analogous to the surface barrier. In this case, a "frozen" magnetic flux remains in the sample, giving rise to the magnetization hysteresis. The Josephson vortices may "transmit" through this barrier to form hypervortices or leave the sample, leading to the relaxation of the trapped magnetic flux.

Discussion and comparison with experiment. The experimental data obtained for the polycrystalline sample in our works [11, 13] are demonstrated in Fig. 1. One can see in Fig. 1 that, at small modulation amplitudes (h = 0.005 Oe), the amplitude ε_1' of the inphase part of the first harmonic of the response signal $\{\varepsilon_1' \propto h\chi_d(H)$ [19, 20], where $\chi_d(H)$ is the differential magnetic susceptibility$\}$ decreases sharply with increasing

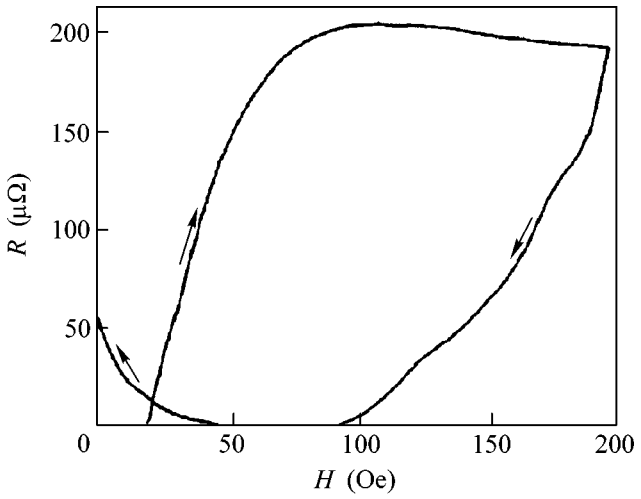

Fig. 2. Magnetic-field dependence of the resistance of a ceramic sample of $YBa_2Cu_3O_{7-x}$ for a dc current of I = 100 mA at $T \approx 77$ K. The arrows indicate the direction of magnetic-field sweep.

static magnetic field H in the range $0 < H < 30$ Oe, after which it smoothly tends toward saturation. The irreversible behavior of ε_1' is observed only if the maximal field H_{max} of the magnetization cycle exceeds a certain value H_{irr}. It follows from Fig. 1 that $H_{irr} \approx 20$ Oe. The value of H_{irr} depends on the sample preparation procedure and lies in the range ~10–70 Oe [11, 13]. With the model described in section 2, one has $H_{irr} = H_J$. Taking into account that $H_{irr} \approx 20$ Oe, the average intergrain distance can be estimated at $d \sim (\Phi_0/H_{irr})^{1/2} \sim 1$ μm. This value of d agrees well with the grain size.

It was found in [11] that $-\chi_d(H) = a + b/\cosh^2(H/H_0)$, where a and b are dimensionless parameters responsible for the linear (grain response) and nonlinear portions of $\chi_d(H)$, respectively (a, $b < 1$ and $H_0 \sim$ 10–25 Oe). Because the resulting nonlinear component of $\chi_d(H)$ fits well with magnetization (12) over the entire range of H values, except for a vicinity of $H = 0$, the parameter H_0 can be identified with H_p in Eq. (12). Using this H_p, let us estimate the effective concentration n_J[1] of supercurrent carriers in a Josephson medium (effective concentration of tunneling pairs). The estimate gives $n_J \sim 10^{19}$–10^{20} cm^{-3}. The concentration of supercurrent carriers in the grains of $YBa_2Cu_3O_{7-x}$ is ~10^{22} cm^{-3} [21]. The value obtained for n_J reflects the structure of the polycrystal. On the other hand, the effective concentration can be estimated by the formula $n_J \sim m\Delta/4\pi e^2\hbar\rho_N$ [cf. Eqs. (6) and (8)]. For $\Delta \sim 30$ meV [21] and $\rho_n \sim 1$ mΩ cm [22], one gets $n_J \sim 10^{19}$ cm^{-3}. Both estimates satisfactorily agree with each other.

The results of the experimental studies of the magnetoresistance of HTSC ceramics [12] are presented in Fig. 2. It is seen from this figure that the dc resistance arises at $H \sim 20$ Oe and increases with the field, while the hysteresis appears on the reverse course for H higher than 20 Oe. As the field approaches zero, a remanent resistance is observed which slowly disappears with time. A plausible explanation for these results is as follows. At $H < H_{irr}$, the strong pinning of hypervortices precludes the emergence of magnetoresistance, so that $R = 0$. At $H > H_{irr}$, the Josephson vortices break away from the pinning centers and move, resulting in the appearance of the dc resistance. A decrease from $H_{max} > H_{irr}$ gives rise to the hysteresis in the $R(H)$ dependence and to a remanent resistance $R(0)$ (Fig. 2), which slowly decreases with time. This is caused by the fact that the trapped Josephson vortices transmit through the potential barrier to form hypervortices and leave the sample.

I am grateful to A.I. Golovashkin, V.A. Koshurnikov, and G.A. Zharkov for discussion of the results.

[1] Unlike the concentration, the effective concentration is estimated using free-electron mass m.

REFERENCES

1. C. Jeffries, Q. Lam, Y. Kim, *et al.*, Phys. Rev. B **37**, 9840 (1988).
2. A. I. Golovashkin, N. D. Kuz'michev, I. S. Levchenko, *et al.*, Fiz. Tverd. Tela (Leningrad) **31** (4), 233 (1989) [Sov. Phys. Solid State **31**, 679 (1989)].
3. A. I. Golovashkin, N. D. Kuz'michev, I. S. Levchenko, *et al.*, Fiz. Tverd. Tela (Leningrad) **32**, 1374 (1990) [Sov. Phys. Solid State **32**, 802 (1990)].
4. Kh. R. Rostami, A. A. Sukhanov, and V. V. Mantorov, Fiz. Nizk. Temp. **22**, 58 (1996) [Low Temp. Phys. **22**, 42 (1996)].
5. S. L. Ginzburg, I. D. Luzyanin, É. Meukhvarishvili, *et al.*, Pis'ma Zh. Éksp. Teor. Fiz. **69**, 184 (1999) [JETP Lett. **69**, 196 (1999)].
6. C. Bean, Phys. Rev. Lett. **8**, 250 (1962).
7. J. R. Clem, Physica C (Amsterdam) **153-155**, 50 (1988).
8. R. G. Mints and A. L. Rakhmanov, *Instability in Superconductors* (Nauka, Moscow, 1984).
9. C. Ebner and D. Stroud, Phys. Rev. B **31**, 165 (1985).
10. C. Jeffries, Q. Lam, Y. Kim, *et al.*, Phys. Rev. B **39**, 11526 (1989).
11. N. D. Kuz'michev and V. V. Slavkin, in *Proceedings of the All-Russia Scientific and Practical Conference "Organizational Philosophical and Technical Problems of Modern Machine-Building Production", Ruzaevka, 2000*, Part 2, p. 9.
12. M. A. Vasyutin, A. I. Golovashkin, N. D. Kuz'michev, and I. S. Levchenko, Preprint No. 85, FIAN (Lebedev Inst. of Physics, USSR Academy of Sciences, Moscow, 1990).

13. A. I. Golovashkin, N. D. Kuz'michev, I. S. Levchenko, *et al.*, Preprint No. 163, FIAN (Lebedev Inst. of Physics, USSR Academy of Sciences, Moscow, 1990).

14. É. B. Sonin, Pis'ma Zh. Éksp. Teor. Fiz. **47**, 415 (1988) [JETP Lett. **47**, 496 (1988)].

15. É. B. Sonin and A. K. Tagantsev, Zh. Éksp. Teor. Fiz. **95**, 994 (1989) [Sov. Phys. JETP **68**, 572 (1989)].

16. L. Solymar, *Superconductive Tunnelling and Applications* (Chapman and Hall, London, 1972; Mir, Moscow, 1974).

17. I. O. Kulik and I. K. Yanson, in *Josephson Effect in Superconducting Tunnel Structures* (Nauka, Moscow, 1970).

18. A. A. Abrikosov, *Fundamentals of the Theory of Metals* (Nauka, Moscow, 1987; North-Holland, Amsterdam, 1988).

19. N. D. Kuz'michev, Pis'ma Zh. Tekh. Fiz. **17** (7), 56 (1991) [Sov. Tech. Phys. Lett. **17**, 259 (1991)].

20. N. D. Kuz'michev, Zh. Tekh. Fiz. **64** (12), 63 (1994) [Tech. Phys. **39**, 1236 (1994)].

21. A. I. Golovashkin, Kratk. Soobshch. Fiz., special issue (1991).

22. N. D. Kuz'michev and M. A. Vasyutin, Sverkhprovodimost: Fiz., Khim., Tekh. **7**, 93 (1994).

Translated by V. Sakun

JETP Letters, Vol. 74, No. 5, 2001, pp. 267–269. Translated from Pis'ma v Zhurnal Éksperimental'noĭ i Teoreticheskoĭ Fiziki, Vol. 74, No. 5, 2001, pp. 296–299.

Self-Organization of an Ensemble of Ge Nanoclusters upon Pulsed Irradiation with Low-Energy Ions during Heteroepitaxy on Si

A. V. Dvurechenskiĭ*, V. A. Zinov'ev, and Zh. V. Smagina

Institute of Semiconductor Physics, Siberian Division, Russian Academy of Sciences, pr. Akademika Lavrent'eva 13, Novosibirsk, 630090 Russia

** e-mail: dvurech@isp.nsc.ru*

Received July 30, 2001

Size distribution of Ge islands formed in the course of Ge heteroepitaxy on Si(111) was studied by scanning tunneling microscopy in experiments of two types: (i) conventional molecular beam epitaxy (MBE) and (ii) pulsed (0.5 s) irradiation with Ge ions of energy ≃200 eV at instants of time corresponding to a filling degree >0.5 for each monolayer. Experiments were performed at a temperature of 350°C. The pulsed ion-beam irradiation during heteroepitaxy leads to a decrease in the average size of Ge islands, an increase in their concentration, and a decrease in the root-mean-square deviation from the mean, as compared to the analogous values in conventional MBE experiments. © *2001 MAIK "Nauka/Interperiodica".*

PACS numbers: 68.65.Hb; 61.80.Jh; 68.37.Ef; 81.15.Hi

Self-organization of semiconducting nanostructures in the course of heteroepitaxy underlies the most promising method of forming ensembles of quantum dots [1–6]. At present, it is commonly accepted that the energy gain caused by the strain relief in 3D islands through the elastic relaxation in protrusion vertices is the key factor in the transition from a two-dimensional layered (2D) to three-dimensional island (3D) heteroepitaxial growth of pseudomorphic films. The islands are ordinarily formed due to the morphological instability of strained films in systems with a large (more than 2%) lattice mismatch between a film and a substrate, among which Ge/Si (4%) and InAs/GaAs (7%) are most familiar.

The self-organization (ordering) effects imply the appearance of islands with preferred characteristics: sizes, shapes, spacing between nanoclusters, and their mutual arrangement. The ordering processes are accompanied by the minimization of free energy of the system. At present, particular attention is being given to the size distribution of islands, because this parameter of a system of quantum dots is of crucial importance in practical applications.

Among the possible ways of improving island homogeneity in sizes, the following are most significant: (a) deviation from the singular surface plane of substrate (see [7] and references therein) and (b) nucleation synchronization [8].

It is generally believed that the nucleation of 3D islands occurs at the imperfections of the 2D layer (heterogeneous nucleation mechanism). Hence, the preliminary creation of the cluster nucleation sites is an efficient way for the island ordering control.

Nucleation synchronization is based on the idea of affecting the adatom supersaturation through a short-term increase in the density of molecular beam or short-term lowering of the substrate temperature. A cyclic variation of supersaturation in the course of growing each atomic layer underlies the optimized method of forming quantum-dimensional structures.

It has recently been found that irradiation with low-energy Ge ions during Ge heteroepitaxy on silicon stimulates the nucleation of Ge islands and reduces the critical thickness at which the 2D ⟶ 3D transition occurs in a pseudomorphic Ge film [9].

The purpose of this work was to study the process of formation of an ensemble of Ge islands and their self-organization upon short-term irradiation of a pseudomorphic Ge film with its own ions during the heteroepitaxy on Si(111) from molecular beams. The (111) face provides the highest stability against the morphological instability that leads to the formation of 3D islands at the surface of a pseudomorphic film during the conventional epitaxy. This was precisely the reason why the surface with (111) orientation was chosen for studying ion irradiation effects.

Experiments were performed in an ultrahigh-vacuum chamber of an MBE setup equipped with an electron-beam evaporator for Si and an effusion cell (boron nitride crucible) for Ge. A system for the ionization and acceleration of germanium ions was designed and fabricated by us and placed over the crucible. The Ge molecular beam was ionized by the transverse electron

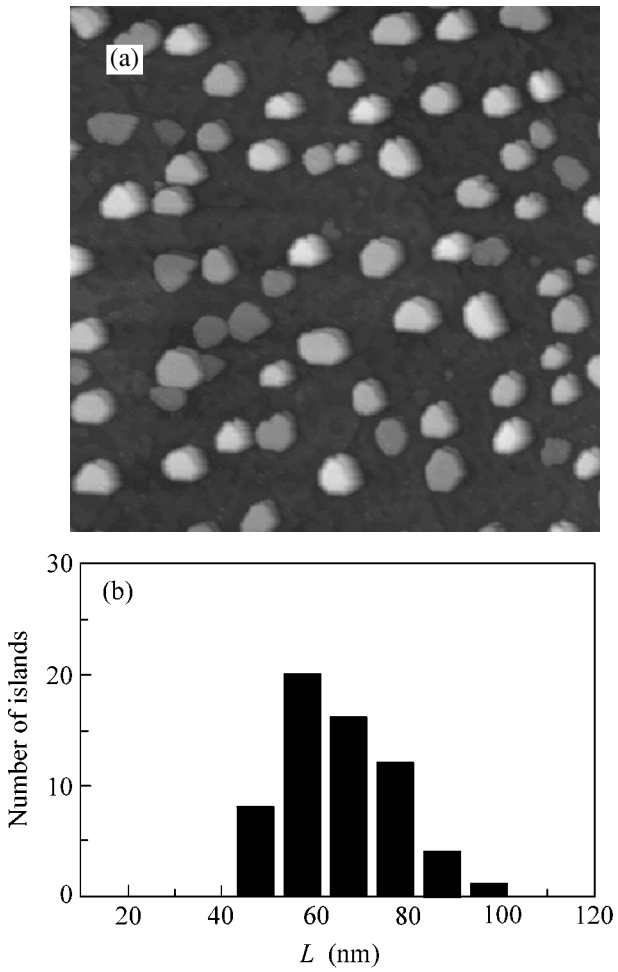

Fig. 1. (a) STM image of a 1000×1000 nm surface area, as obtained *ex situ* after Ge heteroepitaxy on Si(111) at a temperature of 350°C (five bilayers are deposited) and (b) size distribution of Ge islands.

beam. The ionization device allowed the degree of ionization of the Ge molecular beam to be varied from 0.1 to 0.5%. A pulsed accelerating voltage supply unit generated ion-current pulses with a duration of 0.5–1 s and an ion energy of 50–200 eV. The angle of incidence of the molecular and ion beams on the substrate was 54.5°. The analytical section of the chamber included a reflection high-energy (20 keV) electron diffractometer. The high-energy electron diffraction (HEED) pattern was detected by a digital video camera during the growth of germanium film, whereupon the data were fed into a computer and processed using a specially developed program package.

The growth velocity of the Ge film was ~1 bilayer (BL) in 10 s (one BL = 1.56×10^{15} at./cm^2), and the substrate temperature was varied in the range 200–400°C. Si(111) wafers with a misorientation angle less than 14′ were used as substrates. Prior to growing the Ge film, the wafers were subjected to high-temperature annealing followed by the growth of a buffer Si layer. The experiments on Ge heteroepitaxy on Si(111) were of two types: (i) conventional molecular beam epitaxy and (ii) molecular beam epitaxy with pulsed (0.5 s) irradiation by Ge ions of energy 200 eV at instants of time corresponding to a filling degree of ≥0.8 for each bilayer. The total amount of the deposited Ge was the same in both types of experiments.

The surface morphology was studied *ex situ* using scanning tunneling microscopy (STM), which allowed the real-space erect image of surface relief to be obtained with an atomic resolution. Measurements were carried out at room temperature in the dc tunneling current regime (bias 2 V, current 0.085–0.7 nA, feedback 3.76–5.31%). The STM images were processed using special programs for determining the size distribution of islands and their concentration.

The experimental results presented in Figs. 1 and 2 were obtained for a Ge flux density of 2.1×10^{14} at./cm^2 s, an ion-current density of 5.5×10^{11} at./cm^2 s, and a substrate temperature of 350°C. The amount of deposited Ge was equal to 5 BLs.

In the experiments of the first type, the concentration of Ge islands was found to be 7.3×10^9 cm^{-2}, their average size was $L = 63 \pm 9$ nm, and the size inhomogeneity was 14% (Fig. 1). In the second-type experiments, the island concentration was found to increase approximately twofold (1.2×10^{10} cm^{-2}), while the average size and size inhomogeneity diminished ($L = 43 \pm 4$ nm and 9%, respectively; Fig. 2). A decrease in the full width at half maximum of the size distribution function is evidence for the size ordering in an ensemble of Ge nanoclusters, the ordering process being the result of the irradiation of a pseudomorphic Ge film with low-energy ions.

Of interest was to carry out some estimates characterizing the process of ion-stimulated nucleation and the growth of Ge islands. It should be noted, first of all, that the integrated Ge ion flux (total irradiation dose) was $\Phi = 0.5 \times 5 \times 5.5 \times 10^{11}$ at./cm^2 s $\simeq 1.4 \times 10^{12}$ at./cm^2. Every impact of the accelerated Ge ions gives rise to ~10 adatoms as a result of knocking out atoms from their regular sites in one or two nearest-to-surface monolayers of the pseudomorphic Ge film. At the sites of knocked-out atoms, a vacancy cluster (of monoatomic thickness) is formed at the surface of the growing layer [10, 11]. The Φ value exceeds the experimentally obtained concentration of Ge islands by almost two orders of magnitude. Consequently, under the experimental conditions chosen, most of the vacancy formations created at the surface of the Ge layer by ion irradiation are smoothed out (annealed) due to the interaction with adatoms coming from the molecular beam or generated by the irradiation. Only a small fraction of vacancy clusters, likely, become the sites of Ge-island nucleation. It is also not improbable that the Stranski–Krastanov mechanism of island formation makes a certain contribution in the second-type experiments with a chosen amount of deposited Ge.

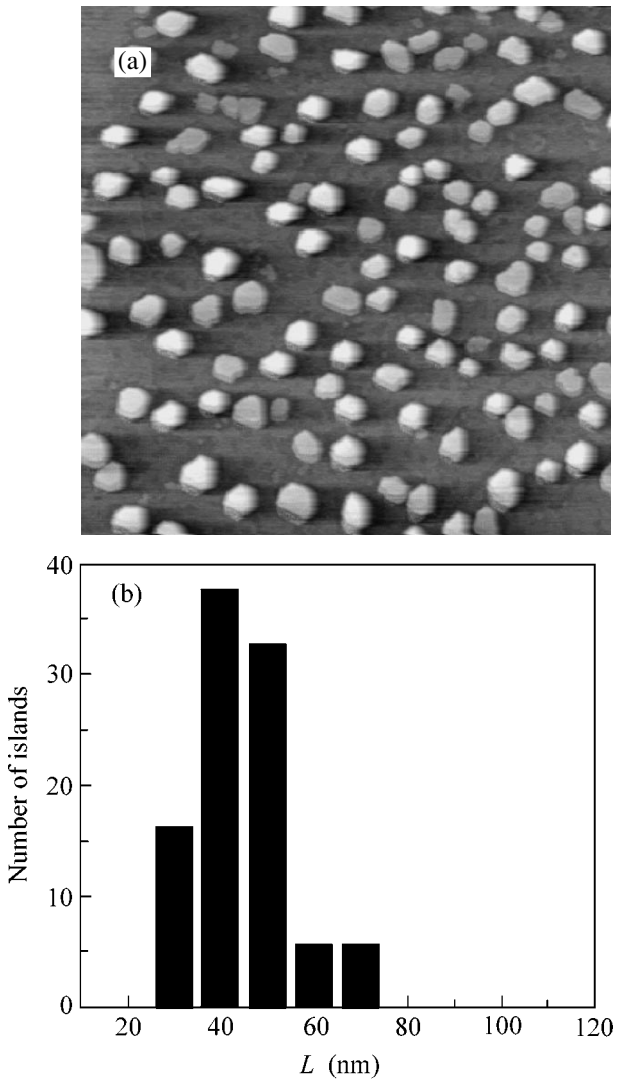

Fig. 2. The same as in Fig. 1 under conditions of pulsed (0.5 s) irradiation with low-energy (200 eV) Ge^+ ions during the heteroepitaxy.

The experiments with smaller amounts of deposited Ge give grounds to assume that the contribution from the ion-stimulated Ge-island formation dominates in the second-type experiments. For instance, the Ge islands are virtually not observed after growing 3.5 BL under conditions of conventional Ge heteroepitaxy on Si(111) (the Ge layer thickness is smaller than critical). The switching on of the pulsed irradiation in the course of heteroepitaxy (second-type experiments) gives rise to the islands with a concentration of 4.3×10^{-10} cm^{-2}.

The size ordering of the Ge islands is, most likely, caused by the following factors: (a) a single-event (within a pulse duration) nucleation of Ge islands after completing the growth of each layer followed by the enlargement of the islands and (b) a decrease in the growing layer roughness under the pulsed action of the Ge^+ ion beam, with an energy of about 200 eV, just before the growth oscillation maximum [9], likely because of an increase in the adatom diffusivity as a result of the ion-stimulated Ge(111)-surface reconstruction, namely, the transition from the (7×7) to the (5×5) superstructure.

We are grateful to V.A. Kudryavtsev for conducting experiments on heteroepitaxy and to S.A. Tiĭs and I.G. Kozhemyako for the STM measurements. This work was supported by the Russian Foundation for Basic Research (project no. 99-02-17196) and the program “Surface Atomic Structures” (project no. 4.2.99).

REFERENCES

1. Zh. I. Alferov, Fiz. Tekh. Poluprovodn. (St. Petersburg) **32**, 317 (1998) [Semiconductors **32**, 1 (1998)].
2. N. N. Ledentsov, V. M. Ustinov, V. A. Shchukin, *et al.*, Fiz. Tekh. Poluprovodn. (St. Petersburg) **32**, 385 (1998) [Semiconductors **32**, 343 (1998)].
3. A. V. Dvurechenskiĭ and A. I. Yakimov, Izv. Vyssh. Uchebn. Zaved., Mater. Élektron. Tekh. **4**, 4 (1999).
4. O. P. Pchelyakov, Yu. B. Bolkhovityanov, A. V. Dvurechenskii, *et al.*, Thin Solid Films **367**, 75 (2000).
5. O. P. Pchelyakov, Yu. B. Bolkhovityanov, A. V. Dvurechenskiĭ, *et al.*, Fiz. Tekh. Poluprovodn. (St. Petersburg) **34**, 1281 (2000) [Semiconductors **34**, 1229 (2000)].
6. A. V. Dvurechenskiĭ and A. I. Yakimov, Izv. Akad. Nauk, Ser. Fiz. **65**, 306 (2000).
7. Y. Kim, B. D. Min, and E. K. Kim, J. Appl. Phys. **85**, 2140 (1999).
8. V. A. Markov, O. P. Pchelyakov, L. V. Sokolov, *et al.*, Surf. Sci. **250**, 229 (1991).
9. A. V. Dvurechenskiĭ, V. A. Zinov’ev, V. A. Kudryavtsev, and Zh. V. Smagina, Pis’ma Zh. Éksp. Teor. Fiz. **72**, 190 (2000) [JETP Lett. **72**, 131 (2000)].
10. A. V. Dvurechenskiĭ, V. A. Zinov’ev, and V. A. Markov, Zh. Éksp. Teor. Fiz. **114**, 2055 (1998) [JETP **87**, 1116 (1998)].
11. A. V. Dvurechenskii, V. A. Zinovyev, V. A. Markov, and V. A. Kudryavtsev, Surf. Sci. **425**, 185 (1999).

Translated by V. Sakun

JETP Letters, Vol. 74, No. 5, 2001, pp. 270–273. From Pis'ma v Zhurnal Éksperimental'noĭ i Teoreticheskoĭ Fiziki, Vol. 74, No. 5, 2001, pp. 300–303.

Cyclotron Spin-Wave in the 2D Electron System[1]

L. V. Kulik[1,2], I. V. Kukushkin[1,2], V. E. Kirpichev[1,2], J. H. Smet[1], K. von Klitzing[1], V. Umansky[3], and W. Wegscheider[4]

[1] *Max-Planck-Institut für Festkörperforschung, 70569 Stuttgart, Germany*

[2] *Institute of Solid State Physics, Russian Academy of Sciences, Chernogolovka, Moscow region, 142432 Russia*

[3] *Braun Center for Submicron Research, Weizman Institute of Science, 76100 Rehovot, Israel*

[4] *Walter Schottky Institut, Technische Universität München, Am Coulombwall, D-85748 Garching, Germany*

Received July 31, 2001

The cyclotron spin-wave mode of a two-dimensional electron system have been investigated by inelastic light scattering. It is observed at small electron filling factors, $\nu \sim 0.1$, when the electron system is spin-depolarized. As long as the electron system becomes fully spin-polarized ($\nu > 0.2$), the cyclotron spin-wave disappears from the inelastic light scattering spectra. It reenters at electron filling factors $\nu > 1$. Over the range of electron filling factors of $1 < \nu < 2$, the cyclotron spin-wave energy is insensitive to both the experimentally accessible in-plane momenta and the electron concentration, whereas its inelastic light scattering efficiency is strongly influenced by the spin polarization of the electron system. © *2001 MAIK "Nauka/Interperiodica".*

PACS numbers: 75.30.Ds; 73.20.-r

Collective excitations in a two-dimensional electron system (2DES) under an external static magnetic field are usually classified as intra- and intersubband modes, associated with poles in the corresponding parts of charge- and spin-density response functions, the intra- and intersubband excitations being taken as noninteracting (the long-wave approximation). The intersubband part of the excitation spectrum consists of principal intersubband modes, which are charge- and spin-density excitations (CDE and SDE) [1], intersubband Bernstein modes [2, 3], and out-of-phase or optical charge and spin-density excitations [4, 5]. The intrasubband excitations can, in turn, be separated into inter- and intra-Landau-level collective modes. The latter are the spin-wave mode and fractional excitations, originating from the nontrivial self-ordering of the 2DES in a partially filled Landau level (LL) [6, 7]. As to the inter-Landau-level (ILL) excitations, they are associated with electron transitions from LL n to LL $n + m$ with or without flipping the electron spin. Their energies are given by

$$E(q) = m\hbar\omega_c + \delta S_z g\mu_B B + E_{\delta S_z}(q). \qquad (1)$$

Here, ω_c is the cyclotron frequency, $\delta S_z = -1, 0, 1$, and m are, respectively, the excitation spin and momentum projections along the magnetic-field axis [8]. At $q \longrightarrow 0$, the $E_{\delta S_z}(q)$ term equals zero for ILL excitations with $\delta S_z = 0$. It can, however, be significant for ILL excitations with $\delta S_z = -1, +1$ [9, 10]. Since there generally exist an infinite number of ILL excitations with different m, hereafter, an example of ILL excitations from the lowest Landau level with $m = 1$ will be considered. The theory of such excitations has been developed in [8] for integer and in [9, 11] for noninteger electron filling factors (ν).

When the electrons in the 2DES equally occupy the two spin states of the lowest LL, the ILL excitations can be classified as singlet and triplet states. The singlet state is a magnetoplasmon, which gives rise to a pole in the charge-density response function. The modes that constitute the triplet state are the two cyclotron spin-flip modes (SF, $\delta S_z = -1, 1$) and the cyclotron spin-wave mode (CSW, $\delta S_z = 0$), with its spin directed in the 2D plane. The magnetoplasmon can be described as an in-phase oscillation of two spin subsystems of the 2DES involving inter-LL electron transitions, whereas the spin-wave mode is associated with the out-of-phase oscillations of two spin subsystems. This classification is no longer valid if the ground state of the 2DES has a different occupation for the two spin states. In that case, both $\delta S_z = 0$ modes, the magnetoplasmon and the cyclotron spin wave, give rise to poles in the charge-density response function, whereas only the cyclotron SF modes give rise to poles in the spin-density response functions. Despite the mixed charge-spin character, the cyclotron spin-wave mode is not active in infrared absorption experiments, because it is a pure spin-density type excitation in the limit of $q \longrightarrow 0$, whereas it becomes a pure charge-density excitation only at $q \longrightarrow \infty$ (the latter statement is not valid for the special case of odd noninteger filling factors, $\nu = 3, 5, 7, \ldots$, when both $\delta S_z = 0$ modes are of charge-density type for all q [12]). Only recently, the cyclotron spin-wave mode was

[1] This article was submitted by the authors in English.

observed for the first time using the inelastic light scattering (ILS) technique in the limiting case of small non-integer filling factors ($\nu \ll 1$) [10]. Here, we report the study of the cyclotron spin-wave at large ν and demonstrate that, at $\nu \sim 2$, it is the cyclotron spin-density wave (*and not the magnetoplasmon*) that dominates inelastic light scattering in the vicinity of the cyclotron frequency.

Four different asymmetrically doped high-quality semiconductor heterostructures containing a single AlGaAs/GaAs quantum well (QW) with a width of 250–300 Å, electron concentrations in the dark of $1.6–3.5 \times 10^{11}$ cm^{-2}, and an electron mobility of $\sim 1.5–7 \times 10^6$ cm^2/Vs were used for this study. The electron concentration (n_s) in the samples was continuously tuned using the opto-depletion effect, and it was measured by means of *in-situ* luminescence [13]. A two-fiber optical system was utilized in the measurements [3]. One fiber transmitted the pumping laser beam, and the other collected the scattered light out of the cryostat. The angles between the sample surface and pumping and collecting fibers were chosen to attune the in-plane momentum transferred to the 2DES via the ILS process. The in-plane momentum was $0.4–1.0 \times 10^5$ cm^{-1}. The scattered light was dispersed by a Ramanor U-1000 double grating monochromator and detected by a CCD camera. Taking into account the resonant nature of ILS in a magnetic field, the experimental spectra were recorded using a series of different photon energies of the pumping radiation.

Figure 1 shows a typical ILS spectrum taken at small ν and a fixed magnetic field of 9.4 T. Three lines are observed in the energy range of the cyclotron resonance (Fig. 1). The lowest and the highest energy lines correspond to the $\Delta S_z = +1$ and $\Delta S_z = -1$ spin-flip modes, respectively (the negative g factor of electrons in GaAs is taken into account), whereas the two central lines correspond to two possible $\Delta S_z = 0$ modes: the magnetoplasmon or cyclotron mode with zero spin, and the cyclotron spin-wave with its spin directed in the QW plane [10]. The inelastic cross section of the spin-wave mode decreases when the spin polarization degree increases. At $\nu > 0.2$, only two modes are left in the spectra, characteristic of a spin-polarized 2DES: the $\Delta S_z = -1$ spin-flip mode and the magnetoplasmon (Fig. 1).

The CSW mode reenters in the ILS spectra as soon as the second electron spin state becomes populated. Figure 2 shows ILS spectra taken in the vicinity of the cyclotron frequency at different magnetic fields over the range of the electron filling factors $1 < \nu < 2$. Two ILS lines are observed, which are identified as the cyclotron spin-wave and magnetoplasmon modes using the same "symmetry test" as in [10]: if one tilts the magnetic field, inter- and intrasubband modes possessing the same symmetry should interact near their energy resonance. Such interactions were indeed observed in our experiment for the magnetoplasmon

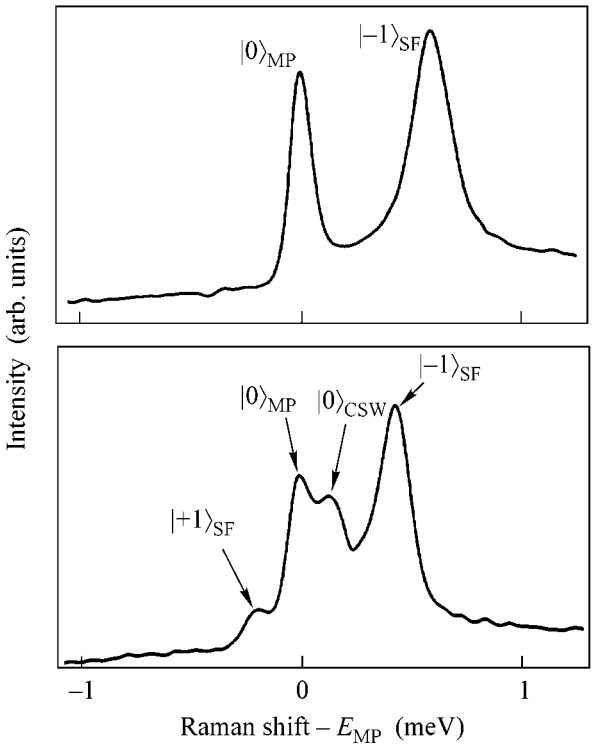

Fig. 1. ILS spectra measured for a single 300 Å QW sample for the in-plane momentum of 0.4×10^5 cm^{-1}, magnetic field $B = 9.4$ T, and $\nu = 0.12$ and 0.26. The lines are classified by the spin projection of their corresponding modes along the magnetic field axis. The spin-triplet state consists of the cyclotron spin-wave ($|0\rangle_{CSW}$) and two spin-flip modes ($|-1\rangle_{SF}$, $|+1\rangle_{SF}$). The spin-singlet state is the magnetoplasmon ($|0\rangle_{MP}$). The energy is measured from the magnetoplasmon energy.

and the intersubband CDE, as well as for the spin-wave and the intersubband SDE. The latter interaction is clearly seen in Fig. 2. Due to the coupling of CSW and SDE, the CSW energy declines from the corresponding energy calculated in the absense of mixing between inter- and intrasubband excitations (solid trianglers), whereas the magnetoplasmon energy intersects the SDE energy without an observable effect.

Having identified the cyclotron spin-wave mode, we compared its dispersion properties with those of the magnetoplasmon (MP). The dispersions of the CSW and MP modes at 6 T are shown in Fig. 3. In agreement with the theory of [9, 11], the CSW mode does not posses any appreciable dispersion for the experimentally accessible in-plane momenta. In contrast, the dispersion of the MP is easily observable. The MP energy demonstrates the familiar linear growth with increasing electron concentration. However, the experimentally observed linear slope of the magnetoplasmon energy is larger than the predicted one, and, as a consequence, the magnetoplasmon energy intersects the spin-wave energy at a finite electron concentration. Thus, at suffi-

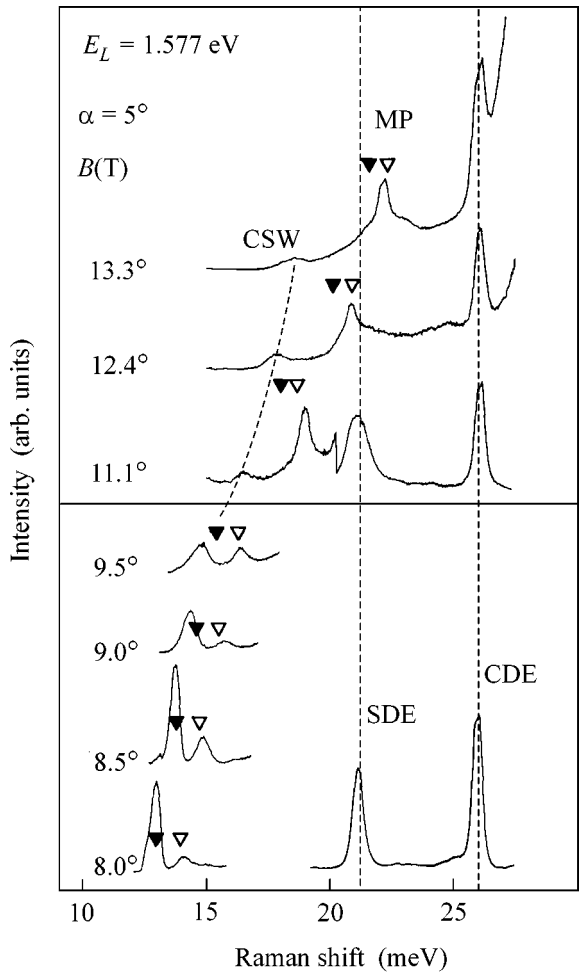

Fig. 2. ILS spectra measured for a 250 Å QW sample with $n_s = 3.5 \times 10^{11}$ cm^{-2} at different magnetic fields close to the response of the CSW and SDE energies. The simulated energies of the magnetoplasmon and the cyclotron spin wave at $q = 1.0 \times 10^5$ cm^{-1} in the absence of interaction between inter- and intrasubband excitations are shown by open and solid triangles. The dotted lines are guides to the eye.

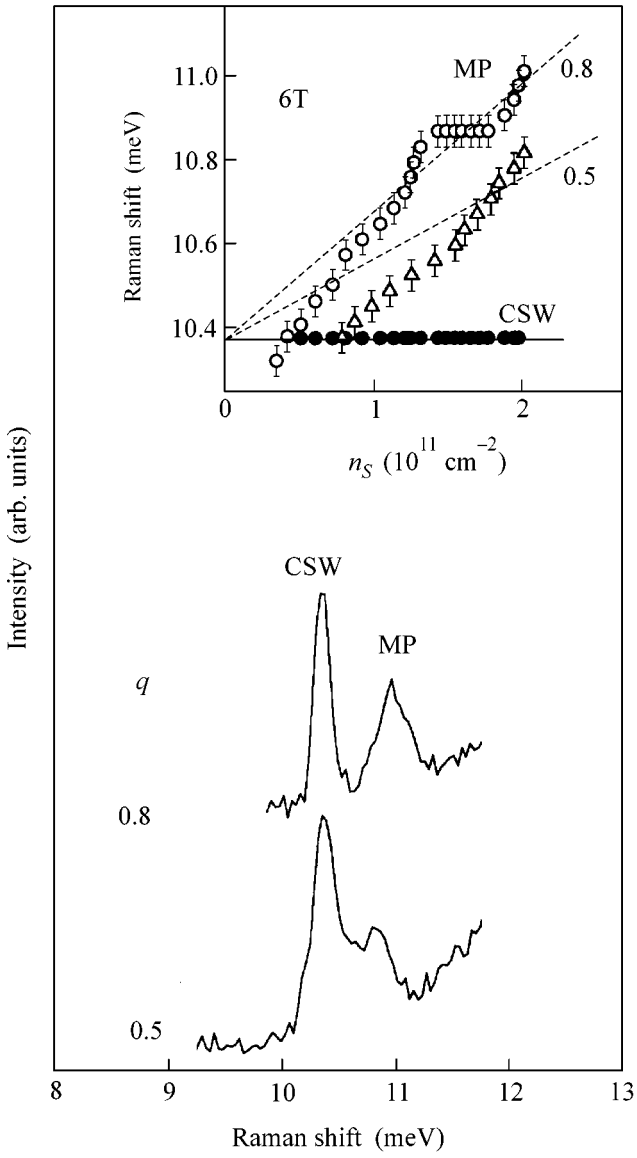

Fig. 3. ILS spectra measured for a 250 Å QW sample with $n_s = 2 \times 10^{11}$ cm^{-2} for two in-plane momenta, 0.5 and 0.8×10^5 cm^{-1}, and a magnetic field of 6 T. In the inset, the MP and SW energies vs. the electron concentration are shown.

ciently large ν, the MP energy exceeds the CSW energy, but at small ν the CSW energy exceeds that of the MP (Fig. 1). This result is in qualitative agreement with conclusions of [14, 15], where the influence of impurities on the spectrum of collective modes is considered. In a way, it resembles a similar experimental observation called "Collapse of the Hartree Term" for intersubband counterparts of CSW and MP, intersubband SDE and CDE [16]. It must, however, be stressed that in an ideal translational-invariant 2DES the calculated CSW and SDE energies are always below those of MP and CDE, respectively [9, 11].

The ILS cross section of the CSW mode and the magnetoplasmon strongly depend on the relative population of the two spin states in the 2DES ground state. Figure 4 shows the electron filling factor and the temperature dependence of the CSW and MP ILS cross sections. When a single spin state is occupied (ν = 1), only the MP mode is observed. The filling of the second spin state by increasing either the electron filling factor or the temperature is accompanied by the enhancement of the CSW ILS cross section. At ν = 2, the dipole-forbidden CSW mode dominates the ILS spectra, which is in contrast to the infrared absorption spectra, where only the dipole-allowed MP mode is generally observed [12]. The ILS from the cyclotron spin-wave mode can thus be employed to characterize the polarization properties of the 2DES's.

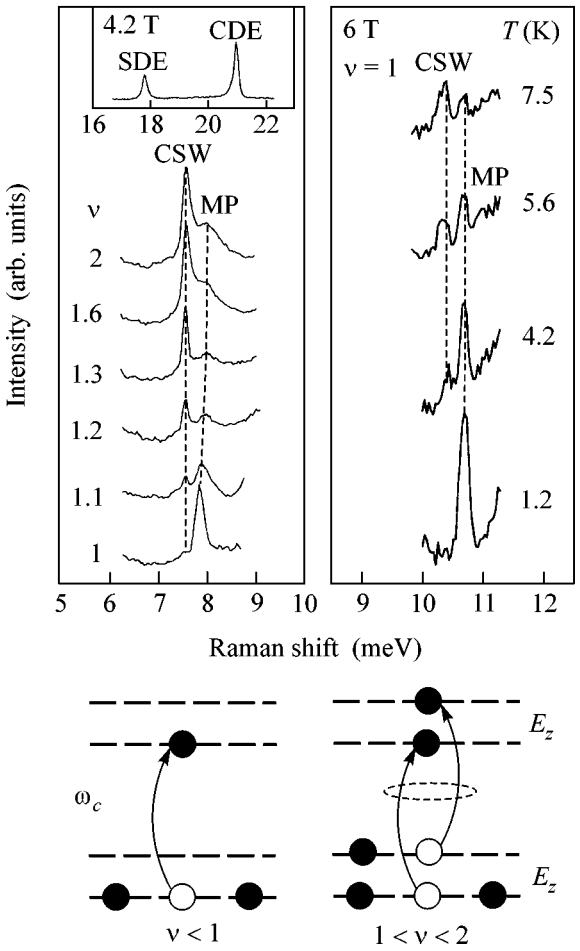

Fig. 4. Left: ILS spectra measured for a 250 Å QW sample with an electron concentration in the dark of 2×10^{11} cm^{-2} for a magnetic field of 4.2 T and different ν (ν is pointed at the left of the spectra). In the inset, the intersubband counterparts of the cyclotron spin wave and the magnetoplasmon, spin- and charge-density excitations (SDE and CDE) for ν = 2 are shown. Right: the temperature dependence of the relative ILS cross sections for the cyclotron spin wave and the magnetoplasmon for a magnetic field of 6 T and ν = 1. The diagram at the bottom demonstrates an additional degree of freedom that allows the cyclotron spin wave to exist. At $1 < \nu < 2$, two modes with $\delta S_z = 0$ can be constructed on the basis of two electronic transitions from two spin states coupled by the Coulomb interaction, whereas at $\nu < 1$ only the magnetoplasmon exists.

In conclusion, we studied the cyclotron spin-wave mode of 2DES in the case where electrons occupy the lowest LL. Being the out-of-phase oscillation of two electron spin subsystems of 2DES, the cyclotron spin-wave mode has zero oscillator strength at small in-plane momenta. Despite this fact, it is active in the inelastic light scattering whenever electrons fill more than one spin state. The energy of the cyclotron spin wave lies at the cyclotron frequency and does not change for the in-plane momenta used in the experiment. The last result is in perfect agreement with the theoretical predictions using Generalized Single Mode and Hartree–Fock approximations [8, 9, 11].

This work was supported by Volkswagen Stiftung, the Russian Foundation for Fundamental Research, the INTAS (project no. v99-1146), and the A. von Humbolt Stiftung (L. V. K.) and the German Israeli (J. H. S and V. U.) Foundations.

REFERENCES

1. A. Pinczuk, S. Schmitt-Rink, G. Danan, *et al.*, Phys. Rev. Lett. **63**, 1633 (1989).
2. G. Brozak, B. V. Shanabrook, D. Gammon, and D. S. Katzer, Phys. Rev. B **47**, 9981 (1993).
3. V. E. Kirpichev, L. V. Kulik, I. V. Kukushkin, *et al.*, Phys. Rev. B **59**, R12751 (1999); L. V. Kulik, I. V. Kukushkin, V. E. Kirpichev, *et al.*, Phys. Rev. B **61**, 12717 (2000).
4. L. V. Kulik, I. V. Kukushkin, V. E. Kirpichev, *et al.*, Phys. Rev. Lett. **86**, 1837 (2001).
5. V. E. Bisti, Pis'ma Zh. Éksp. Teor. Fiz. **69**, 543 (1999) [JETP Lett. **69**, 584 (1999)].
6. M. Dobers, K. V. Klitzing, and G. Weimann, Phys. Rev. B **38**, 5453 (1988).
7. M. Kang, A. Pinczuk, B. S. Dennis, *et al.*, Phys. Rev. Lett. **84**, 546 (2000).
8. C. Kallin and B. I. Halperin, Phys. Rev. B **30**, 5655 (1984).
9. J. P. Longo and C. Kallin, Phys. Rev. B **47**, 4429 (1993).
10. L. V. Kulik, I. V. Kukushkin, V. E. Kirpichev, *et al.*, Phys. Rev. B **63**, 201402(R) (2001).
11. H. C. A. Oji and A. H. MacDonald, Phys. Rev. B **33**, 3810 (1986).
12. M. Manger, E. Batke, R. Hey, *et al.*, Phys. Rev. B **63**, 121203(R) (2001).
13. O. V. Volkov, I. V. Kukushkin, M. V. Lebedev, *et al.*, Pis'ma Zh. Éksp. Teor. Fiz. **71**, 558 (2000) [JETP Lett. **71**, 383 (2000)].
14. C. M. Hu, T. Friedrich, E. Batke, *et al.*, Phys. Rev. B **52**, 12090 (1995).
15. C. Kallin and B. I. Halperin, Phys. Rev. B **31**, 3635 (1985).
16. S. Ernst, A. R. Goni, K. Syassen, and K. Eberl, Phys. Rev. Lett. **72**, 4029 (1994).

JETP Letters, Vol. 74, No. 5, 2001, pp. 274–278. Translated from Pis'ma v Zhurnal Éksperimental'noĭ i Teoreticheskoĭ Fiziki, Vol. 74, No. 5, 2001, pp. 304–308.

Nonstoichiometry and Critical Temperature of MgB_2

M. V. Indenbom*, L. S. Uspenskaya, M. P. Kulakov, I. K. Bdikin, and S. A. Zver'kov

Institute of Solid-State Physics, Russian Academy of Sciences, Chernogolovka, Moscow region, 142432 Russia

** e-mail: indenbom@issp.ac.ru*

Received August 1, 2001

The influence of nonstoichiometry of the new high-temperature superconductor MgB_2 on its critical temperature was studied by the direct magnetooptical observations of the penetration and trapping of magnetic flux. To preclude the possible influence of accidental factors, a special sample with transition from pure boron to the MgB_2 with an excess of Mg was synthesized. In a narrow region near the unreacted boron, the magnetic-field trapping and screening disappear at a temperature 1.5 K higher than in the dominant stoichiometric region of the sample. © *2001 MAIK "Nauka/Interperiodica".*

PACS numbers: 74.62.Bf; 74.72.-h

Although it has been found in the avalanche of works, devoted to studying the superconductivity of MgB_2 [1] after its recent discovery, that even high-quality samples show a noticeable scatter of the transition temperature from canonical 39 K to 37 K and lower, this fact was either not discussed at all or attributed to the influence of impurities. A strong lowering of critical temperature in aluminum-doped MgB_2 [2] provides an example of such an influence. However, the use of pure components in the synthesis of MgB_2 precludes the impurity effect. The influence of different contents of boron isotopes ^{11}B and ^{10}B can also be excluded, because the replacement of all isotopes of one sort by the isotopes of another sort shifts T_c by only 1 K [3], and because one ordinarily uses approximately the same natural mixture of isotopes. The fact that T_c depends only on the synthesis temperature suggests that MgB_2 is not strictly stoichiometric and that a homogeneity region $Mg_{1-x}B_2$ exists in the Mg–B diagram [4]. The large values of x correspond to higher T_c, in compliance with recent band calculations of $Mg_{1-x}B_2$ [5]. Attempts to directly study the influence of the nonstoichiometry of $Mg_{1-x}B_2$ on T_c have faced the problem of measuring the contents of light Mg and B elements with a high accuracy (see [6] and references therein). Moreover, the removal of a portion of magnesium by vacuum annealing of samples, or the preparation of a magnesium-deficient or magnesium-enriched $Mg_{1-x}B_2$, virtually did not affect the T_c value [6]. To obviate the uncertainty associated with controlling the composition of $Mg_{1-x}B_2$, we have synthesized samples in which the Mg content changes monotonically within the maximum possible limits. Our method of the direct visualization of magnetic field in superconductors [7–9] allowed not only the spatial inhomogeneities of magnetic-flux dynamics to be resolved for these samples but also the temperature dependences of the local magnetic ac susceptibility to be measured at selected points [9].

Dense ceramic samples of $Mg_{1-x}B_2$ with variable Mg content were prepared using the following workup. A powder of amorphous boron (99.95% purity) was pressed into cylinders with a diameter of about 10 mm at a pressure of 2×10^2 MPa and placed at the bottom of a molybdenum crucible. Plates of metallic magnesium (99.95% purity) were set on a boron pellet, and the crucible was closed with a cover and placed in a furnace with an electrical heater. The furnace was preliminary evacuated to 10^{-5} atm and then filled with pure argon at a pressure of 10–12 atm. After heating to 950°C, the exothermic combination reaction between boron and magnesium started from the boron surface. For the details of this method of synthesizing MgB_2, see [4]. The temperature dependences of resistance, magnetic susceptibility, and microwave losses were measured for dense ceramic samples that were cut from the synthesized ceramics [4, 10]. The same samples were used for pressure studies [11]. According to these measurements, the superconducting transition temperature was near 38 K. The amount of magnesium and the synthesis time were chosen so that the unreacted boron powder remained in the central part of the synthesized ceramics. Metallic magnesium condensed on the outer surface of such a hollow MgB_2 cylinder upon cooling

0021-3640/01/7405-0274$21.00 © 2001 MAIK "Nauka/Interperiodica"

in the furnace. Therefore, the synthesized samples were characterized by a gradual transition from an excess of magnesium to its deficiency. Further studies were carried out with thin plates that were cut along the cylinder radius (dashed prism in Fig. 1), ground to a thickness of 260 μm, and polished to mirror luster (see Fig. 3a).

The weight percentage of Mg in the samples was determined relative to the pure metallic magnesium standard using X-ray microanalysis. These measurements confirmed that the Mg content decreased from the outer edge of the sample at $R = 0$ to the unreacted boron core at $R = 3$ mm (upper curve in Fig. 2). Although measurements were made for the cleanest and smoothest areas of the polished surfaces without noticeable inclusions and pores, the results showed a sizable scatter. The Mg weight content in the ideal MgB_2 lattice is 53%. One may assume that the composition of the prepared MgB_2 gradually changes from stoichiometric to approximately $Mg_{0.8}B_2$. A small contribution of pure magnesium detected by X-ray diffraction was neglected. The enhanced content of Mg at the edge $R = 0$ is, apparently, due to the above-mentioned condensation of Mg on the outer surface of the ceramics. To find out how the phase composition and lattice parameters change along R, the sample was cross-cut into several fragments, and the diffraction spectra were measured separately for each of them. Because the intensities of the corresponding diffraction peaks were normalized to the surface areas of these fragments, the variations of peak intensities from sample to sample were proportional to the variations of the concentrations of the respective crystal phases. It was established that the content of pure Mg (lower curve in Fig. 2) decreased in accordance with the assumed drop of magnesium vapor pressure during Mg deposition at the end of synthesis. At the same time, the content of MgB_2 (middle curve in Fig. 2) virtually does not change along R except for a region near $R = 3$ mm, where the reduced content of MgB_2 is likely due to the presence of residual amorphous boron, which does not reveal itself in X-ray diffraction. The MgB_4 phase was not observed at all. A small amount of MgO was detected in all fragments, probably, because of the oxidation of their surfaces. Measurements of the diffraction peaks (201) and (102) of MgB_2 suggested that the lattice parameter c increased with increasing R (inset in Fig. 2), in agreement with the data reported in [6]. This counts in favor of the fact that the concentration gradient produced for Mg in the course of synthesis leads to the respective Mg deficiency in the MgB_2 lattice.

The magnetic-flux trapping in one of the thin plates (1×3 mm) with a gradient of Mg content across it is shown in Fig. 3 for different temperatures. The images were obtained using a ferrimagnetic garnet film with in-plane anisotropy. The film was placed on the polished surface of the sample and served as an indicator of magnetic-field distribution [9]. Unique possibilities of this method have already found use in recently initiated studies of MgB_2; these possibilities are aimed at demonstrating good intergrain supercurrent in ceramics and wires [12–16] and revealing the specific features of magnetic-

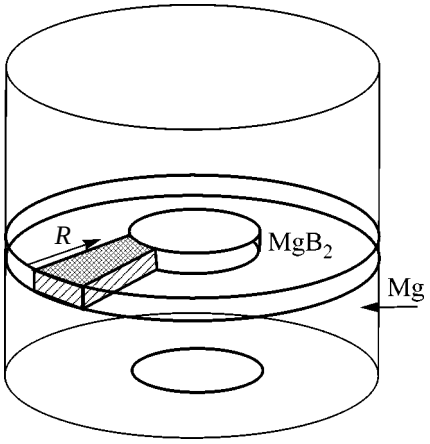

Fig. 1. Scheme of synthesis and preparation of the ceramic samples of $Mg_{1-x}B_2$ for study. The Mg arrow indicates the direction of magnesium diffusion, and B is the residual unreacted boron at the cylinder center. R corresponds to the abscissa in Fig. 2.

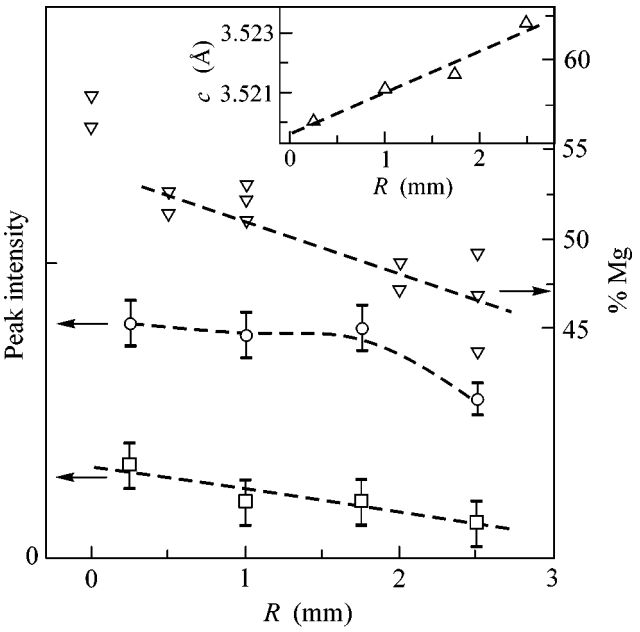

Fig. 2. Distribution of Mg and MgB_2 along the direction from the outer surface of the synthesized cylinder to the inner unreacted boron core. The left axis is for the relative X-ray peak intensity: □ for pure Mg and ○ for MgB_2. The right axis (▽) is for the Mg weight percentage, as measured using X-ray microanalysis. Inset: variation of the lattice parameter c of MgB_2 in the sample.

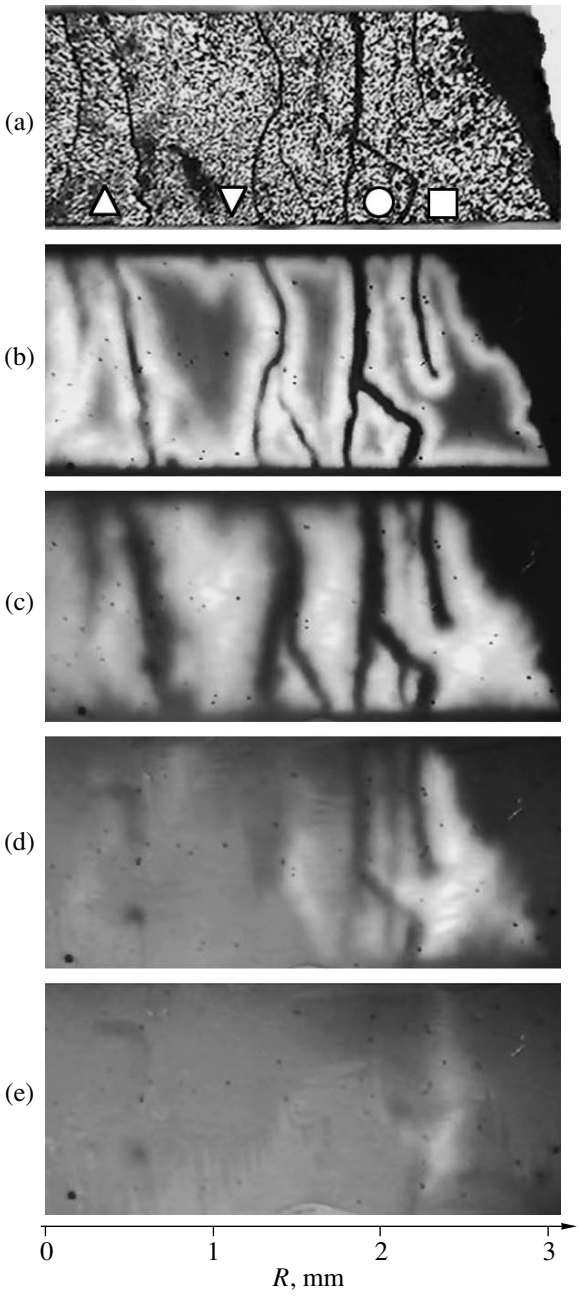

Fig. 3. Magnetic-flux trapping in one of the MgB_2 plates that was cut out as shown in Fig. 1. Maximal field is 1200 Oe. T = (b) 29.0 K (partial penetration of magnetic field), (c) 36.3 K, (d) 37.8 K, and (e) 38.7 K. (a) Plate surface. (b–e) The residual unreacted boron (at the right) is colored black and does not show up in the magnetooptical images. The marks △, ▽, ○, and □ indicate the areas for which the magnetic susceptibility curves (shown in Fig. 4) were measured.

field penetration into new films [17–19]. The sample was preliminarily zero-field cooled to a temperature of 12 K. After each additional rise in temperature, a maximal field of 1200 Oe was applied again and then switched off. At low temperatures, a partial magnetic-field penetration was observed (Fig. 3b). The magnetic flux penetrated and trapped near the sample edges and cracks shows up as bright light stripes (a higher brightness corresponds to a higher field at the corresponding area of the superconductor surface [9]). The azimuthal cracks, which are seen both at the polished plate surface (Fig. 3a) and due to field penetration, evidently, appear as a result of the expansion of the material in the course of synthesis, but they have little effect on the radial diffusion of Mg during the synthesis. One can clearly see that, even away from T_c, the penetration depths are different in the sample domains separated by cracks. At the edge, where the Mg content is higher (at the left of the figure), the magnetic field penetrates easier and the trapped-flux stripes are wider. At temperatures above 35 K, magnetic field penetrates over the entire depth of the sample, and the maximal trapped flux is observed at the centers of the domains separated by cracks (Fig. 3c). A magnetic flux trapped in the magnesium-enriched part is considerably smaller than at the opposite Mg-deficient edge, and, hence, the critical current is weaker at the same temperature. When the superconductivity at the left edge completely disappears at a temperature corresponding to the temperature $T_c \approx 38$ K of superconducting transition measured for this ceramics by macroscopic methods [4, 10], the right edge continues to firmly hold the penetrated magnetic flux (Fig. 3d). One can see from a comparison of Figs. 3c and 3d that the fields trapped at the opposite edges of the sample are comparable if the temperatures differ by 1.5 K. The last traces of superconductivity are observed at the right edge in the form of a narrow stripe at a temperature that is also approximately 1.5 K higher than for an analogous pattern at the left edge of the sample (Fig. 3e). This value corresponds to the maximum increase in T_c due to the Mg deficiency.

To more accurately estimate T_c and present the data in a more customary form, we measured the local ac magnetic susceptibilities, as was done in our previous work [8]. For this purpose, a small fragment of the microscopic image (20 μm in diameter) was cut out using a diaphragm, and its brightness was measured by a photomultiplier, whose field-synchronized signal was detected by a lock-in voltmeter. These measurements are fully analogous to the measurements of local susceptibility using miniature coils or a Hall microprobe, but in our case the measurements can be done for any one point at the sample surface during a single experiment. The curves obtained for the characteristic points indicated in Fig. 3a are presented in Fig. 4. The local values of T_c correspond to the onset of diamagnetic screening upon lowering the temperature. According to our observations of magnetic-flux trapping, they change from 37.2 to 39.0 K, with a maximum near the largest magnesium deficiency.

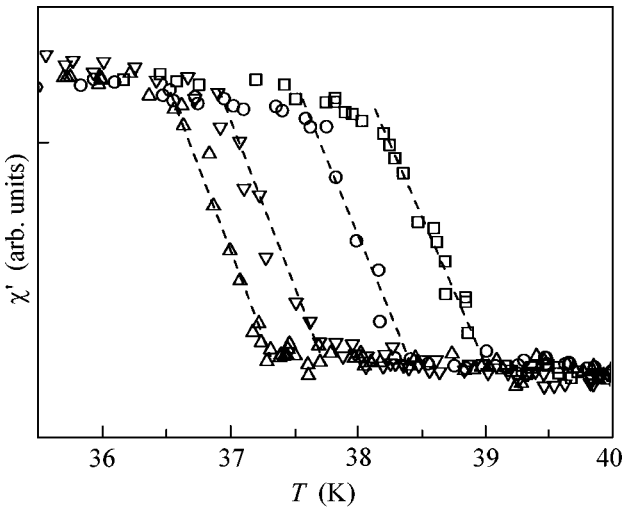

Fig. 4. Local magnetic susceptibility curves. The Mg deficiency increases from left to right. The measurement points are marked in Fig. 3a by △, ▽, ○, and □, respectively. The ac field amplitude is 8 G and the frequency is 17 Hz.

The results obtained in this work closely resemble our observations of the inhomogeneous superconductivity in single crystals of a high-temperature $YBa_2Cu_3O_{7-\delta}$ superconductor with inhomogeneous oxygen content [8]. The only distinction is that this effect is more pronounced in $YBa_2Cu_3O_{7-\delta}$: from the maximum transition temperature in the oxygen-saturated corner of a crystal to the absence of superconductivity in its bulk, to which oxygen does not diffuse. As for $Mg_{1-x}B_2$, a change in the transition temperature is comparable with the transition width so that this change is not quite obvious.

Thus, the superconducting transition temperature rises with an increase in the Mg deficiency, confirming the possible existence of a homogeneity region for $Mg_{1-x}B_2$. The crystal lattice of $Mg_{1-x}B_2$ is very dense and the B–B bonds are very strong, so that the presence of boron vacancies and stable interstitial Mg atoms is energetically unfavorable [5]. Magnesium deficiency is the only "natural" free parameter. Accordingly, one can conclude that the maximal "canonical" value $T_c = 39$ K [1] occurs in $Mg_{1-x}B_2$ with a certain magnesium deficiency ($x \sim 0.2$), which is in equilibrium with the MgB_4 phase and is mostly obtained upon high-temperature annealing. As to the "proper" value of T_c for the stoichiometric MgB_2 ($x = 0$), it is more than 1.5 degrees higher and is achieved in the synthesis with an excess of magnesium, as, e.g., in our syntheses of composite Mg–MgB_2 targets by the method similar to that described above and conducted with the same starting materials [19]. As was pointed out above, the band calculations of nonstoichiometric $Mg_{1-x}B_2$ have led to the same conclusion [5], but the real Mg deficiency is much smaller than that assumed in calculations. It should also be pointed out that the effect noticeably increases under pressure. The rate of pressure-induced T_c degradation changes systematically from $dT_c/dp \approx -1$ K/GPa for the samples with $T_c \approx 39$ K to $dT_c/dp \approx -2$ K/GPa for the samples with $T_c \approx 37$ K [11, 20]. In light of the aforesaid, this is explained by the fact that the Fermi level in Mg-deficient $Mg_{1-x}B_2$ ($x > 0$) lies in a less steep region of the two-dimensional energy band, so that the pressure-induced band shift has a considerably weaker effect on T_c [21].

Financial support for part of the experimental equipment by the Alexander von Humboldt Foundation and the Swiss National Scientific Foundation (project no. 7-SUP-J048290-96) is greatly acknowledged. This work was supported by the State Program of the Russian Federation "Topical Problems of Condensed Matter Physics," "High-Temperature Superconductivity" direction. We thank A.A. Polyanskii for acquainting us with his magnetooptical studies of MgB_2 ceramics and films [12–14, 17] before their publication.

REFERENCES

1. J. Nagamatsu, N. Nakagawa, T. Muranaka, *et al.*, Nature **410**, 63 (2001).
2. J. S. Slusky, N. Rogado, K. A. Regan, *et al.*, Nature **410**, 343 (2001); cond-mat/0102262 (2001).
3. S. L. Bud'ko, G. Lapertot, C. Petrovic, *et al.*, Phys. Rev. Lett. **86**, 1877 (2001).
4. N. N. Kolesnikov and M. P. Kulakov, cond-mat/0107164 (2001); Physica C (Amsterdam) (in press).
5. N. I. Medvedeva, A. L. Ivanovski, J. E. Medvedeva, and A. J. Freeman, Phys. Rev. B **64**, 20502 (2001); cond-mat/0103157 (2001); N. I. Medvedeva, Yu. E. Medvedeva, A. L. Ivanovskiĭ, *et al.*, Pis'ma Zh. Éksp. Teor. Fiz. **73**, 378 (2001) [JETP Lett. **73**, 336 (2001)].
6. Y. Y. Xue, R. L. Meng, B. Lorenz, *et al.*, cond-mat/0105478 (2001); submitted to Phys. Rev. B.
7. A. A. Polyanskii, V. K. Vlasko-Vlasov, M. V. Indenbom, and V. I. Nikitenko, Pis'ma Zh. Tekh. Fiz. **15** (22), 1 (1989) [Sov. Tech. Phys. Lett. **15**, 872 (1989)].
8. V. K. Vlasko-Vlasov, M. V. Indenbom, V. I. Nikitenko, *et al.*, Sverkhprovodimost: Fiz., Khim., Tekh. **3**, 1199 (1990); L. Dorosinskii, B. Farber, M. Indenbom, *et al.*, Ferroelectrics **111**, 321 (1990).
9. L. A. Dorosinskii, M. V. Indenbom, V. I. Nikitenko, *et al.*, Physica C (Amsterdam) **206**, 360 (1993).
10. Yu. A. Nefyodov, M. R. Trunin, A. F. Shevkun, *et al.*, cond-mat/0107057 (2001).
11. V. G. Tissen, M. V. Nefedova, N. N. Kolesnikov, and M. P. Kulakov, cond-mat/0105475 (2001); Physica C (Amsterdam) (in press).
12. D. C. Larbalestier, M. O. Rikel, L. D. Cooley, *et al.*, Nature **410**, 186 (2001); cond-mat/0102216 (2001).

13. A. A. Polyanskii, J. Y. Jiang, M. Rikel, *et al.*, APS March Meeting, Seattle, 2001, unpublished.

14. A. A. Polyanskii, A. Gurevich, J. Jiang, *et al.*, cond-mat/0107532 (2001); submitted to Supercond. Sci. Technol.

15. K. Kawano, J. S. Abell, M. Kambara, *et al.*, cond-mat/0104114 (2001).

16. T. C. Shields, K. Kawano, D. Holdom, and J. S. Abell, cond-mat/0107034 (2001).

17. A. A. Polyanskii *et al.*, unpublished.

18. T. H. Johansen, M. Baziljevich, D. V. Shantsev, *et al.*, cond-mat/0104113 (2001); submitted to Phys. Rev. Lett.

19. C. N. Ermolov, M. V. Indenbom, A. N. Rossolenko, *et al.*, Pis'ma Zh. Éksp. Teor. Fiz. **73**, 626 (2001) [JETP Lett. **73**, 557 (2001)].

20. S. Deemyad, J. S. Schilling, J. D. Jorgensen, and D. G. Hinks, cond-mat/0106057 (2001).

21. P. Bordet, M. Mezouar, M. Núñez-Regueiro, *et al.*, cond-mat/0106585 (2001); Phys. Rev. B (in press).

Translated by V. Sakun

JETP Letters, Vol. 74, No. 5, 2001, pp. 279–283. From Pis'ma v Zhurnal Éksperimental'noĭ i Teoreticheskoĭ Fiziki, Vol. 74, No. 5, 2001, pp. 309–313.

On Critical Behavior of Phase Transitions in Certain Antiferromagnets with Complicated Ordering[1]

A. I. Mudrov* and K. B. Varnashev**

Bar-Ilan University, 52900 Ramat-Gan, Israel

St. Petersburg Electrotechnical University, St. Petersburg, 197376 Russia

** e-mail: mudrova@macs.biu.ac.il*

*** e-mail: kvarnash@kv8100.spb.edu*

Received June 28, 2001; in final form August 6, 2001

Within the four-loop ε expansion, we study the critical behavior of certain antiferromagnets with complicated ordering. We show that an anisotropic stable fixed point governs the phase transitions with new critical exponents. This is supported by the estimate of critical dimensionality $N_c^C = 1.445(20)$ obtained from six loops via the exact relation $N_c^C = \frac{1}{2}N_c^R$ established for the complex and real hypercubic models. © *2001 MAIK "Nauka/Interperiodica".*

PACS numbers: 75.40.Cx; 64.60.Fr; 75.50.Gg

It is known that the critical properties of phase transitions in certain antiferromagnets involving an increase of the unit cell in one or more directions at the critical temperature can be described by a generalized $2N$-component ($N \geq 2$) Ginzburg-Landau model with three independent quartic terms

$$H = \int d^D x \left[\frac{1}{2}\sum_{i=1}^{2N} (m_0^2 \varphi_i^2 + \nabla\varphi_i \nabla\varphi_i) + \frac{u_0}{4!}\left(\sum_{i=1}^{2N} \varphi_i^2\right)^2 + \frac{v_0}{4!}\sum_{i=1}^{2N} \varphi_i^4 + 2\frac{z_0}{4!}\sum_{i=1}^{N} \varphi_{2i-1}^2 \varphi_{2i}^2 \right] \quad (1)$$

associated with the isotropic, cubic, and tetragonal interactions, respectively [1]. Here, φ_i is the real vector order parameter in $D = 4 - \varepsilon$ dimensions and m_0^2 is proportional to the deviation from the mean-field transition point. When $N = 2$, Hamiltonian (1) describes the antiferromagnetic phase transitions in $TbAu_2$ and DyC_2 and the structural phase transition in NbO_2 crystal.[2] Another physically important case $N = 3$ is relevant to the antiferromagnetic phase transitions in such substances as K_2IrCl_6, TbD_2, MnS_2, and Nd. All these phase transitions are known from experiments to be of second order[3] (see [5] and references therein). However, the experimental data were insufficiently accurate to provide reliable values of critical exponents, and the obtained estimates [6–8] were found to differ significantly from the theoretically expected numbers.

For the first time, the magnetic and structural phase transitions described by model (1) were studied within the framework of the renormalization group (RG) by Mukamel and Krinsky to the lowest orders in ε [1, 4]. A three-dimensionally stable fixed point (FP) with coordinates $u^* > 0$, $v^* = z^* > 0$ was predicted.[4] That point was shown to determine a new universality class with a specific set of critical exponents. However, for the physically important case $N = 2$, the critical exponents of this unique stable FP turned out to be exactly the same as those of the $O(4)$-symmetric one.

For the years, an alternative analysis of critical behavior of the model, the RG approach in three dimensions, was carried out within two- and three-loop approximations [9, 10]. Those investigations gave the same qualitative predictions: the unique stable FP does exist on the 3D RG flow diagram. By using different resummation procedures, the critical exponents computed at this point proved to be close to those of the

[1] This article was submitted by the authors in English.

[2] The phase transitions in helical magnets Tb, Dy, and Ho belong to the same class of universality [2].

[3] An interesting type of multisublattice antiferromagnets, such as MnO, CoO, FeO, and NiO, was studied in [3, 4]. It was shown, to the leading orders in ε, that the phase transitions in these substances are of first order.

[4] Following Mukamel [1], we call this point "unique."

Bose FP ($u = 0$, $v = z > 0$) rather than to the isotropic [$O(N)$-symmetric; $u > 0$, $v = z = 0$] one. It was also shown that the unique and the Bose FPs are very close to each other, so that they may interchange their stability in the next orders of RG approximation [10].

Recently, the critical properties of the model were analyzed to third order in ε [11,12]. Investigation of the FP stability and calculation of the critical dimensionality N_c of the order parameter separating two different regimes of critical behavior[5] confirmed that model (1) has a unique stable FP at $N = 2$ and $N = 3$. However, the twofold degeneracy of the stability matrix eigenvalues at the one-loop level was observed for this FP [12]. That degeneracy was shown to cause a substantial decrease in the accuracy expected within the three-loop approximation and the powers of $\sqrt{\varepsilon}$ to appear in the expansions.[6] So, computational difficulties were shown to grow faster than the amount of essential information one could extract from high-loop approximations. That resulted in the conclusion that the ε-expansion method is not quite effective for the given model.

Another problem associated with model (1) is the question whether the unique FP is really stable in 3D, thus leading to a new class of universality, or is its stability only an effect of insufficient accuracy of the RG approximations used. Indeed, there are general nonperturbative theoretical arguments indicating that the only stable FP in 3D may be the Bose one and the phase transitions of interest should be governed by that stable FP [14]. However, up to now, this assertion found no confirmation within the RG approach. In such a situation, it is highly desirable to extend already known ε expansions for the stability matrix eigenvalues, critical exponents, and the critical dimensionality in order to apply the more sophisticated resummation technique to longer expansions.

In this work, we first avoid the problem of the eigenvalues degeneracy in model (1) by analyzing the critical behavior of an equivalent complex N^C-component order parameter model with the effective Hamiltonian

$$H = \int d^D x \Big[\frac{1}{2}(m_0^2 \psi_i \psi_i^* + \nabla \psi_i \nabla \psi_i^*) + \frac{u_0}{4!} \psi_i \psi_i^* \psi_j \psi_j^* + \frac{v_0}{4!} \psi_i \psi_i \psi_i^* \psi_i^* \Big] \tag{2}$$

comprising the isotropic and cubic interactions.[7] Note that this Hamiltonian also describes the real hypercubic model [16] if ψ_i is thought to be the real N^R-component order parameter. The model (2) comes out exactly from model (l) at $v_0 = z_0$, and it is free from eigenvalue degeneracy. Second, we examine the existence of the anisotropic stable FP in model (2) on the basis of the higher-order ε expansion. Namely, using dimensional regularization and the minimal subtraction scheme [17], we derive the four-loop RG functions as a power series in ε and analyze the FP stability. For the first time, we give realistic numerical estimates for the stability matrix eigenvalues using the Borel transformation with a conformal mapping [18]. This allows us to carry out careful analysis of the stability of all the FPs of the model. We state the exact relation $N_c^C = \frac{1}{2} N_c^R$ between the critical (marginal) spin dimensionalities of the real and complex hypercubic models and obtain the estimate $N_c^C = 1.445(20)$ using six-loop results of [19]. We show that the anisotropic (complex cubic; $u \neq 0$, $v \neq 0$) stable FP of model (2), being the counterpart of the unique point in model (1), does exist on the 3D RG flow diagram at $N^C > N_c^C$. For this stable FP, we give more accurate critical exponent estimates in comparison with the previous three-loop results [12] by applying the summation technique of [20] to the longer series.

The four-loop ε expansion for the β functions of model (2) were recently obtained by us in [21]. From the system of equations $\beta_u(u^*, v^*) = 0$, $\beta_v(u^*, v^*) = 0$, one can calculate formal series for the four FPs: the trivial Gaussian one and nontrivial isotropic, Bose, and complex cubic FPs. Instead of presenting here the FPs themselves, which have no direct physical meaning, we present the eigenvalues of the stability matrix

$$\Omega = \begin{pmatrix} \dfrac{\partial \beta_u(u, v)}{\partial u} & \dfrac{\partial \beta_u(u, v)}{\partial v} \\ \dfrac{\partial \beta_v(u, v)}{\partial u} & \dfrac{\partial \beta_v(u, v)}{\partial v} \end{pmatrix} \tag{3}$$

taken at the most intriguing Bose and complex cubic FPs. They are

$$\omega_1 = -\frac{1}{2}\varepsilon + \frac{6}{20}\varepsilon^2 + \frac{1}{8}\Big[-\frac{257}{125} - \frac{384}{125}\zeta(3)\Big]\varepsilon^3 + \frac{1}{16}\Big[\frac{5109}{1250} + \frac{624}{125}\zeta(3) - \frac{576}{125}\zeta(4) + \frac{3648}{125}\zeta(5)\Big]\varepsilon^4,$$
$$\omega_2 = \frac{1}{10}\varepsilon - \frac{14}{100}\varepsilon^2 + \frac{1}{8}\Big[-\frac{311}{625} + \frac{768}{625}\zeta(3)\Big]\varepsilon^3 + \frac{1}{16}\Big[-\frac{61}{250} + \frac{3752}{3125}\zeta(3) + \frac{1152}{625}\zeta(4) - \frac{4864}{625}\zeta(5)\Big]\varepsilon^4, \tag{4}$$

[5] When $N > N_c$, the unique FP is stable in 3D, while for $N < N_c$, the stable FP is the isotropic one.

[6] A similar phenomenon was observed earlier in studying the impure Ising model (see [13]). Half-integer powers in ε arising in that model have different origin but also lead to the loss of accuracy.

[7] The model with the complex vector order parameter was considered by Dzyaloshinskii [15] in studying the phase transitions in DyC_2, $TbAu_2$ ($N^C = 2$) and TbD_2, MnS_2, and Nd ($N^C = 3$).

at the Bose FP and for $N^C = 2$

$$\omega_1 = -\frac{1}{2}\varepsilon + \frac{13}{48}\varepsilon^2 + \frac{1}{8}\left[-\frac{65}{36} - \frac{7}{3}\zeta(3)\right]\varepsilon^3 + \frac{1}{16}\left[\frac{1679}{432} + \frac{169}{36}\zeta(3) - \frac{7}{2}\zeta(4) + \frac{365}{18}\zeta(5)\right]\varepsilon^4,$$

$$\omega_2 = -\frac{1}{12}\varepsilon^2 + \frac{1}{8}\left[\frac{5}{18} + \frac{5}{6}\zeta(3)\right]\varepsilon^3 + \frac{1}{16}\left[\frac{181}{144} - \frac{145}{72}\zeta(3) + \frac{5}{4}\zeta(4) - \frac{50}{9}\zeta(5)\right]\varepsilon^4 \quad (5)$$

and $N^C = 3$

$$\omega_1 = -\frac{1}{2}\varepsilon + \frac{58}{220}\varepsilon^2 + \frac{1}{8}\left[-\frac{19533}{15125} - \frac{14832}{6655}\zeta(3)\right]\varepsilon^3 + \frac{1}{16}\left[\frac{310518757}{91506250} + \frac{1644864}{1830125}\zeta(3) - \frac{22248}{6655}\zeta(4) + \frac{283056}{14641}\zeta(5)\right]\varepsilon^4,$$

$$\omega_2 = -\frac{1}{22}\varepsilon + \frac{2}{2420}\varepsilon^2 + \frac{1}{8}\left[\frac{90363}{166375} - \frac{3408}{73205}\zeta(3)\right]\varepsilon^3 + \frac{1}{16}\left[\frac{1151231173}{1006568750} - \frac{50696504}{20131375}\zeta(3) - \frac{5112}{73205}\zeta(4) + \frac{107344}{161051}\zeta(5)\right]\varepsilon^4 \quad (6)$$

at the complex cubic one, where $\zeta(3)$, $\zeta(4)$, and $\zeta(5)$ are the Riemann ζ functions.

It is known that RG series are at best asymptotic. An appropriate resummation procedure has to be applied in order to extract reliable physical information from them. To obtain the eigenvalue estimates, we have used an approach based on the Borel transformation modified with a conformal mapping [18, 20]. If both eigenvalues of matrix (3) are negative, the associated FP is infrared stable and the critical behavior of the experimental systems undergoing second-order phase transitions is determined only by that stable point. For the Bose and the complex cubic FPs, our numerical results are presented in Table 1. It is seen that the complex cubic FP is absolutely stable in $D = 3$ ($\varepsilon = 1$), while the Bose point appears to be of the "saddle" type. However ω_2's of either points are very small at the four-loop level, thus implying that these points may swap their stability in the next order of RG approximation. We can compare ω_2 at the complex cubic FP quoted in Table 1 with the three-loop results of [9] obtained within the framework of the RG approach directly in 3D. Those estimates $\omega_2 = -0.010$ for $N^C = 2$ and $\omega_2 = -0.011$ for $N^C = 3$ are solidly consistent with ours.

Table 1. Eigenvalue exponent estimates for the Bose (BFP) and the complex cubic (CCFP) FPs at $N^C = 2$ and $N^C = 3$, as obtained in the four-loop order in ε ($\varepsilon = 1$) using the Borel transformation with a conformal mapping

Type of FP	$N^C = 2$		$N^C = 3$	
	ω_1	ω_2	ω_1	ω_2
BFP	−0.395(25)	0.004(5)	−0.395(25)	0.004(5)
CCFP	−0.392(30)	−0.029(20)	−0.400(30)	−0.015(6)

The four-loop ε expansion for the critical dimensionality of the order parameter of model (2) reads

$$N_c^C = 2 - \varepsilon + \frac{5}{24}[6\zeta(3) - 1]\varepsilon^2 + \frac{1}{144}[45\zeta(3) + 135\zeta(4) - 600\zeta(5) - 1]\varepsilon^3.$$

Instead of processing this expression numerically, we state the exact relation $N_c^C = \frac{1}{2}N_c^R$, which is independent of the order of approximation used. In fact, the critical dimensionality N_c^C for the complex cubic model is determined as that value of N^C at which the complex cubic FP coincides with the isotropic one. In the same way, the critical dimensionality N_c^R is defined for the real cubic model. Both systems exhibit effectively the isotropic critical behavior at $N^C = N_c^C$ and $N^R = N_c^R$. So, because the complex $O(2N^C)$-symmetric model is equivalent to the real $O(N^R)$-symmetric one, the relation $2N_c^C = N_c^R$ holds true. For $N^C > N_c^C$, the complex cubic FP of model (2) should be stable in 3D.

The five-loop ε expansion for N_c^R was recently obtained in [22]. Resummation of that series gave the estimate $N_c^R = 2.894(40)$ (see [23]). Therefore, we conclude that $N_c^C = 1.447(20)$ from the five loops. Practically the same estimate $N_c^C = 1.435(25)$ follows from the constrained analysis of N_c^R, taking into account $N_c^R = 2$ in two dimensions [19]. From the recent pseudo-ε-expansion analysis of the real hypercubic model [24], one can extract $N_c^C = 1.431(3)$. However, the most accurate estimate $N_c^C = 1.445(20)$ results from the value $N_c^R = 2.89(4)$, obtained on the basis of the numerical analysis of the four-loop [23] and the six-loop [19] 3D RG expansions for the β functions of the real hypercubic model.

Table 2. Critical exponents for the isotropic (IFP), the Bose (BFP), and the complex cubic (CCFP) FPs at $N^C = 2$ and $N^C = 3$, as calculated in the four-loop order in ε ($\varepsilon = 1$) using the Borel transformation with a conformal mapping

Type of FP	$N^C = 2$			$N^C = 3$		
	η	ν	γ	η	ν	γ
IFP	0.0343(20)	0.725(15)	1.429(20)	0.0317(10)	0.775(15)	1.524(25)
BFP	0.0348(10)	0.664(7)	1.309(10)	0.0348(10)	0.664(7)	1.309(10)
CCFP	0.0343(20)	0.715(10)	1.404(25)	0.0345(15)	0.702(10)	1.390(25)

Finally, we have computed the four-loop ε series for the critical exponents. At the stable complex cubic FP, they are

$$\eta = \frac{\varepsilon^2}{48} + \frac{5}{288}\varepsilon^3 - \frac{21\zeta(3) - 13}{1728}\varepsilon^4,$$

$$\gamma^{-1} = 1 - \frac{\varepsilon}{4} - \frac{7}{96}\varepsilon^2 + \frac{84\zeta(3) - 1}{1152}\varepsilon^2 \qquad (7)$$

$$- \frac{1420\zeta(3) - 1512\zeta(4) + 5840\zeta(5) - 2059}{27648}\varepsilon^4,$$

for $N^C = 2$ and

$$\eta = \frac{5}{242}\varepsilon^2 + \frac{177}{10648}\varepsilon^3 - \frac{59328\zeta(3) - 50083}{5153632}\varepsilon^4,$$

$$\gamma^{-1} = 1 - \frac{3}{11}\varepsilon - \frac{7}{242}\varepsilon^2 + \frac{912\zeta(3) + 3905}{58564}\varepsilon^3 \qquad (8)$$

$$- \frac{207682\zeta(3) - 15048\zeta(4) + 30320\zeta(5) - 151817}{1288408}\varepsilon^4,$$

for $N^C = 3$. Other critical exponents can be found through the known scaling relations. The numerical estimates obtained are collected in Table 2. The critical exponents for the isotropic and the Bose FPs are also presented for comparison. We can compare our results with the available experimental data. For example, in the case of the structural transition in the NbO_2 crystal, the critical exponent of spontaneous polarization was measured in [7], $0.33 < \beta < 0.44$. Our estimate $\beta = 0.371$ obtained using the data of Table 2 and scaling relations lies in that interval.

In summary, the four-loop ε-expansion analysis of the Ginzburg–Landau model with cubic anisotropy and complex vector order parameter relevant to the phase transitions in certain antiferromagnets with complicated ordering has been carried out. Investigation of the global structure of RG flows for the physically significant cases $N^C = 2$ and $N^C = 3$ leads to the conclusion that the anisotropic complex cubic FP is absolutely stable in 3D. Therefore, the critical thermodynamics of the phase transitions in the NbO_2 crystal and in the antiferromagnets $TbAu_2$, DyC_2, K_2IrCl_6, TbD_2, MnS_2, and Nd should be governed by this stable point with a specific set of critical exponents, within the frame of the given approximation. The critical dimensionality $N_c^C = 1.445(20)$, obtained from six loops, supports this conclusion. At the complex cubic FP, the critical exponents were calculated using the Borel summation technique in combination with a conformal mapping. For the structural phase transition in NbO_2 and for the antiferromagnetic phase transitions in $TbAu_2$ and DyC_2, they were shown to be close to the critical exponents of the $O(4)$-symmetric model. In contrast to this, the critical exponents for the antiferromagnetic phase transitions in K_2IrCl_6, TbD_2, MnS_2, and Nd turned out to be close to the Bose ones.

Although our calculations show that the complex cubic FP, rather than the Bose one, is stable at the four-loop level, the eigenvalues ω_2 of both points are very small. Therefore, the situation is very close to marginal, and the FPs might change their stability to opposite in the next order of perturbation theory, so that the Bose point would become stable. This conjecture is in agreement with the recent six-loop RG study of the three-coupling-constant model (1) directly in three dimensions [25]. The authors argue in support of the global stability of the Bose FP, although the numerical estimate $\omega_2 = -0.007(8)$ of the smallest stability matrix eigenvalue of the Bose point appears to be very small, and the apparent accuracy of the analysis does not exclude the opposite sign for ω_2. In this situation, it would be very desirable to compare the critical exponent values obtained theoretically with values that could be determined from experiments, in order to confirm which of the two FPs is really stable in physical space. Finally, it would also be useful to investigate certain universal amplitude ratios of the model, because they vary much more among different universality classes than exponents do and might be more effective as a diagnostic tool.

We are grateful to Prof. M. Henkel for his helpful remarks and to Dr. E. Vicari for sending us a copy of the review cited in [25]. This work was supported by the Russian Foundation for Basic Research (project no. 01-02-17048) and the Ministry of Education of the Russian Federation (project no. E00-3.2-132).

REFERENCES

1. D. Mukamel, Phys. Rev. Lett. **34**, 481 (1975); D. Mukamel and S. Krinsky, J. Phys. C **8**, L496 (1975); Phys. Rev. B **13**, 5065 (1976).
2. P. Bak and D. Mukamel, Phys. Rev. B **13**, 5086 (1976).
3. S. A. Brazovskiĭ and I. E. Dzyaloshinskiĭ, Pis'ma Zh. Éksp. Teor. Fiz. **21**, 360 (1975) [JETP Lett. **21**, 164 (1975)]; S. A. Brazovskiĭ, I. E. Dzyaloshinskiĭ, and B. G. Kukharenko, Zh. Éksp. Teor. Fiz. **70**, 2257 (1976) [Sov. Phys. JETP **43**, 1178 (1976)]; P. Bak, S. Krinsky, and D. Mukamel, Phys. Rev. Lett. **36**, 52 (1976) and references therein.
4. D. Mukamel and S. Krinsky, Phys. Rev. B **13**, 5078 (1976).
5. J. C. Toledano, L. Michel, P. Toledano, and E. Brézin, Phys. Rev. B **31**, 7171 (1985).
6. J. Als-Nielsen, in *Phase Transitions and Critical Phenomena*, Ed. by C. Domb and M. S. Green (Academic, New York, 1976), Vol. 5A, p. 88.
7. R. Pynn and J. D. Axe, J. Phys. C **9**, L199 (1976).
8. J. Schneck *et al.*, Phys. Rev. B **25**, 1766 (1982).
9. N. A. Shpot, Phys. Lett. A **133**, 125 (1988); **142**, 474 (1989).
10. K. B. Varnashev and A. I. Sokolov, Fiz. Tverd. Tela (St. Petersburg) **38**, 3665 (1996) [Phys. Solid State **38**, 1996 (1996)]; A. I. Sokolov, K. B. Varnashev, and A. I. Mudrov, Int. J. Mod. Phys. B **12**, 1365 (1998); A. I. Sokolov and K. B. Varnashev, Phys. Rev. B **59**, 8363 (1999).
11. K. De'Bell and D. J. W. Geldart, Phys. Rev. B **32**, 4763 (1985); E. J. Blagoeva, Mod. Phys. Lett. B **10**, 439 (1996).
12. A. I. Mudrov and K. B. Varnashev, Phys. Rev. B **57**, 3562 (1998); **57**, 5704 (1998).
13. D. E. Khmelnitskiĭ, Zh. Éksp. Teor. Fiz. **68**, 1960 (1975) [Sov. Phys. JETP **41**, 981 (1976)].
14. J. Sak, Phys. Rev. B **10**, 3957 (1974); K. A. Cowley and A. D. Bruce, J. Phys. C **11**, 3577 (1978).
15. I. E. Dzyaloshinskiĭ, Zh. Éksp. Teor. Fiz. **72**, 1930 (1977) [Sov. Phys. JETP **45**, 1014 (1977)].
16. A. Aharony, in *Phase Transition and Critical Phenomena*, Ed. by C. Domb and M. S. Green (Academic, New York, 1976), Vol. 6, p. 357.
17. G. 't Hooft and M. Veltman, Nucl. Phys. B **44**, 189 (1972); G. 't Hooft, Nucl. Phys. B **61**, 455 (1973).
18. J. C. Le Guillou and J. Zinn-Justin, Phys. Rev. Lett. **39**, 95 (1977); Phys. Rev. B **21**, 3976 (1980); R. Seznec and J. Zinn-Justin, J. Math. Phys. **20**, 1398 (1979); A. A. Vladimirov, D. I. Kazakov, and O. V. Tarasov, Zh. Éksp. Teor. Fiz. **77**, 1035 (1979) [Sov. Phys. JETP **50**, 521 (1979)].
19. J. M. Carmona, A. Pelissetto, and E. Vicari, Phys. Rev. B **61**, 15136 (2000).
20. A. I. Mudrov and K. B. Varnashev, Phys. Rev. E **58**, 5371 (1998); in *Problems of Quantum Field Theory* (Joint Inst. for Nuclear Research, Dubna, 1999), p. 267; hep-th/9811125 (1998).
21. A. I. Mudrov and K. B. Varnashev, J. Phys. A **34**, L347 (2001); in *Group Theoretical Methods in Physics* (Joint Inst. for Nuclear Research, Dubna, 2001); cond-mat/0011167 (2000).
22. H. Kleinert and V. Schulte-Frohlinde, Phys. Lett. B **342**, 284 (1995).
23. K. B. Varnashev, J. Phys. A **33**, 3121 (2000); Phys. Rev. B **61**, 14660 (2000).
24. R. Folk, Yu. Holovatch, and T. Yavors'kii, Phys. Rev. B **62**, 12195 (2000).
25. A. Pelissetto and E. Vicari, cond-mat/0012164 (2000).

JETP Letters, Vol. 74, No. 5, 2001, pp. 284–287. Translated from Pis'ma v Zhurnal Éksperimental'noĭ i Teoreticheskoĭ Fiziki, Vol. 74, No. 5, 2001, pp. 314–317.

Vector Area Theorem Mapping in Crystals and Polarization Stability of SIT Solitons[1]

V. N. Lisin

Zavoĭskiĭ Physicotechnical Institute, Kazan Scientific Center, Russian Academy of Sciences, Sibirskiĭ trakt 10/7, Kazan 29, 420029 Tatarstan, 664033 Russia

e-mail: vlisin@kfti.knc.ru

Received July 16, 2001; in final form, August 8, 2001

The stability of polarization, areas, and the number of self-induced transparency (SIT) solitons at the output of the $LaF_3 : Pr^{3+}$ crystal is theoretically studied versus the polarization direction and the area of the input linearly polarized laser pulse. For this purpose, the Vector Area Theorem is rederived and the two-dimensional Vector Area Theorem map is obtained. The map is governed by the crystal symmetry and takes into account directions of the dipole matrix element vectors of the different site subgroups of optically excited ions. The Vector Area Theorem mapping of the time evolution of the laser pulse allows one to highlight soliton polarization properties.

PACS numbers: 42.50.Md; 42.65.Tg

For an isotropic medium, stability properties of self-induced transparency (SIT) solitons are determined by the Area Theorem. The Area Theorem is the name given to a theoretical result that governs the coherent nonlinear transmission of short light pulses through isotropic materials, effectively two-level media, that have an absorption resonance very near the frequency of the incident light. In 1967, McCall and Hahn [1] identified a new parameter (called "Area" and denoted by θ) of optical pulses travelling in such media and then predicted that the Area obeys the simple equation

$$\frac{\partial\theta}{\partial z} = -\frac{\alpha}{2}\sin\theta, \tag{1}$$

where α is the attenuation coefficient for the material. The two most striking consequences of the Area Theorem are the following: (i) pulses with special values of Area, namely, all integer multiples of π, are predicted to maintain the same Area during propagation, and (ii) pulses with other values of Area must change during propagation until their Area reaches one of the special values. This property can be shown to be unstable for the odd multiples, but the even multiples enjoy the full immunity of the theorem. Equation (1) was derived for the isotropic material in which the dipole matrix element vector of any ion is parallel to the electric field vector of the light pulse. On the contrary, the direction of the dipole matrix element vector of any Pr^{3+} ion in LaF_3 does not depend on the electric field vector of the light pulse. Thus, it is necessary to rederive Area Theorem taking into account directions of the dipole matrix element vectors of the different subgroups of Pr^{3+} ions. Pr^{3+} ions in a LaF_3 unit cell can replace La^{3+} in six different types of sites ($\pm\alpha$, $\pm\beta$, $\pm\gamma$). The local environment of any of these has C_2 symmetry. Six local C_2-symmetry axes are located in the plane normal to the C_3 axis and make an angle of $2\pi/6$ in this plane (Fig. 1). The electric dipole matrix element vector of the Pr^{3+} ion (optical transition $\Gamma_1 \longrightarrow \Gamma_1$)

$$\mathbf{p}_j = \mathbf{p}\mathbf{e}_j, \ldots \quad j = 1, \ldots, 6 \tag{2}$$

is directed [2] along the local C_2-symmetry axis

$$\mathbf{e}_j = \left(\cos\left(j\frac{2\pi}{6}\right), \sin\left(j\frac{2\pi}{6}\right)\right), \quad \mathbf{e}_z \cdot \mathbf{e}_j = 0, \tag{3}$$

where $\mathbf{e}_j$ is the unit vector along the C_{2j} axis. Here, the Z axis is directed along the C_3 axis and the X axis along the α axis. We define the Vector Area of the light pulse as

$$\mathbf{\Theta} = \frac{p}{\hbar}\int_{-\infty}^{+\infty} dt\mathbf{E}(z, t), \tag{4}$$

where $\mathbf{E}(z, t)$ is the vector amplitude of the light pulse, p is the electric dipole matrix element, and $\hbar$ is Planck's constant. Taking into account Eqs. (2) and (3) and using arguments presented in [3], we can write the equation for the Vector Area as:

$$\frac{\partial\Theta}{\partial z} = -\alpha\frac{1}{6}\sum_{j=1}^{6}\mathbf{e}_j\sin(\mathbf{\Theta}\cdot\mathbf{e}_j), \tag{5}$$

[1] This article was submitted by the authors in English.

if a light pulse propagates along the C_3 axis. Here, α is the linear attenuation coefficient for $LaF_3 : Pr^{3+}$. As $\mathbf{\Theta} \longrightarrow 0$, Eq. (5) transforms to

$$\frac{\partial \mathbf{\Theta}}{\partial z} = -\frac{\alpha}{2}\mathbf{\Theta}, \tag{6}$$

as expected for a small pulse Area.

Equating the right-hand side of Eq. (5) to zero, we can find special values of the Vector Area, where $\partial\mathbf{\Theta}/\partial z = 0$. It can be done more obviously and easily from the graphical representation. We can rewrite Eq. (5) as

$$\frac{\partial \mathbf{\Theta}}{\partial z} = \frac{\partial}{\partial \mathbf{\Theta}}\frac{\alpha}{6}\sum_{j=1}^{6}\cos(\mathbf{\Theta}\cdot\mathbf{e}_j), \tag{7}$$

and the problem is reduced to the determination of points in a two-dimensional plane, in which the function $\sum\cos(\mathbf{\Theta}\cdot\mathbf{e}_j)$ has extremes. The circles and triangles in Fig. 2 give the contour plot of this function. We easily find three types of special values of the Vector Area, namely,

$$\mathbf{\Theta}_c = m\mathbf{\Theta}_+ + n\mathbf{\Theta}_-, \tag{8}$$

$$\mathbf{\Theta}_u = \mathbf{\Theta}_c + \mathbf{u}_j, \tag{9}$$

$$\mathbf{\Theta}_s = \mathbf{\Theta}_c + \mathbf{s}_j, \tag{10}$$

which are predicted to maintain the same Vector Area during propagation. Here, m and n are arbitrary integers and

$$\mathbf{\Theta}_+ = \frac{2\pi}{\cos(\pi/6)}\mathbf{k}_1, \quad \mathbf{\Theta}_- = \frac{2\pi}{\cos(\pi/6)}\mathbf{k}_6; \tag{11}$$

$$\mathbf{s}_j = \frac{\pi}{\cos(\pi/6)}\mathbf{k}_j, \tag{12}$$

$$\mathbf{u}_j = \frac{\pi}{\cos^2(\pi/6)}\mathbf{e}_j, \tag{13}$$

where the unit vectors $\mathbf{e}_j$ (3) and $\mathbf{k}_j$ are directed, respectively, along and between the C_2 axes:

$$\mathbf{k}_j = \left(\cos\left(j\frac{2\pi}{6} - \frac{\pi}{6}\right), \sin\left(j\frac{2\pi}{6} - \frac{\pi}{6}\right)\right). \tag{14}$$

These special points (8)–(10) give rise to a two-dimensional lattice in a $\mathbf{\Theta}$-phase plane with basis vectors $\mathbf{\Theta}_+$ and $\mathbf{\Theta}_-$ (11), as is shown in Fig. 2. A unit cell of the lattice is determined by the symmetry of the crystal. It is a regular hexagon. The hexagon centers are $\mathbf{\Theta}_c$ (8) (centers of the circles in Fig. 2). As measured from the hexagon center, coordinates of the six vertices of the hexagon are $\mathbf{u}_j$ (13) (centers of the triangles in Fig. 2), and coordinates of midpoints of the sides of the hexagon are $\mathbf{s}_j$ (12). It is obvious from Eqs. (5), (7) and definitions (8)–(10) that, in a neighborhood of these special points, the Vector Area behaves as

$$\frac{\partial \mathbf{\Theta}}{\partial z} = -\frac{\alpha}{2}(\mathbf{\Theta} - \mathbf{\Theta}_c), \tag{15}$$

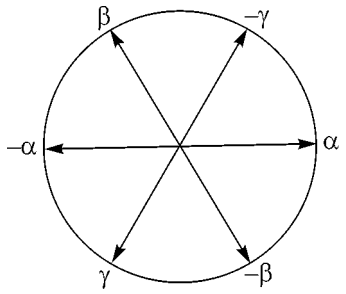

Fig. 1. Directions of the local C_2-symmetry axes for the different Pr^{3+} ion sites in the plane normal to the C_3 axis of the $LaF_3 : Pr^{3+}$ crystal.

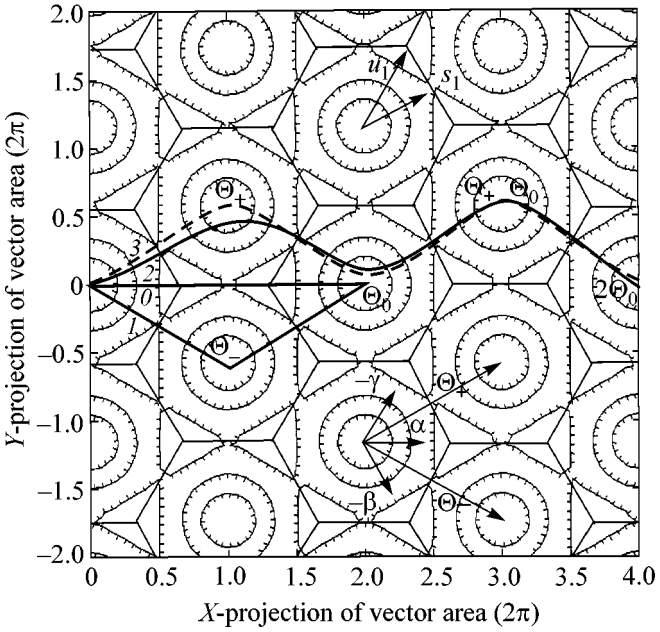

Fig. 2. Vector Area Theorem map. The $\mathbf{\Theta}/2\pi$ projections onto the X and Y axes are plotted on the X and Y axes, accordingly. The vectors $\mathbf{s}_1$ (12) and $\mathbf{u}_1$ (13) are shown in the upper part of the figure. The two basis vectors $\mathbf{\Theta}_+$ and $\mathbf{\Theta}_-$ (11) and the unit vectors along the local C_2-symmetry axes ($+\alpha$, $-\beta$, $-\gamma$) are in the lower part of the figure. Vector coordinates of some of the unit-cell centers are also shown. Bold lines *0* and *1* are mappings of the time evolution of laser pulses with mod $(\mathbf{\Theta}_0) = 4\pi$, and the angles between the directions of the Vector Area and the crystallographic axis α are 0° and –1°, respectively. In this case, $\alpha L = 20$, where L is the sample length and α is the attenuation coefficient. The bold line *2* is the mapping of the time evolution of the laser pulse with mod$(2\mathbf{\Theta}_0) = 8\pi$; the angle between the directions of the Vector Area and the crystallographic axis α is +1°, and $\alpha L = 40$. The bold line *3* is as *2*, but $\alpha L = 80$.

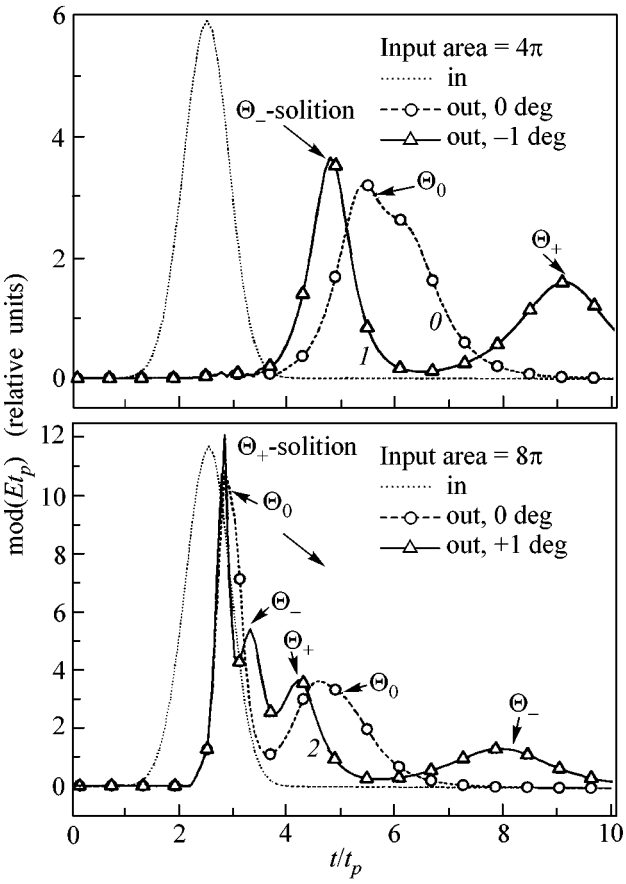

Fig. 3. Time evolution of the amplitude of the laser pulses at the output of the sample. Values of the input Area, the angles between the directions of the Vector Area and the crystallographic axes α, and the parameter L for the curves *0*, *1*, and *2* are the same as for the curves *0*, *1*, and *2* in Fig. 2. The value αL for the 0° curve in the lower part of the figure is the same as for curve *2*. The dotted line is input pulse, and t_p is the input pulse duration. The Vector Area Theorem mapping (curves *1* and *2* in Fig. 2) allows one to easily spot the polarizations and the areas of the solitons in curves *1* and *2* in this figure.

$$\frac{\partial \boldsymbol{\Theta}}{\partial z} = \frac{\alpha}{4}(\boldsymbol{\Theta} - \boldsymbol{\Theta}_u), \tag{16}$$

and as

$$\frac{\partial \boldsymbol{\Theta}}{\partial z} = -\frac{\alpha}{6}(\boldsymbol{\Theta} - \boldsymbol{\Theta}_s), \tag{17}$$

if $\boldsymbol{\Theta} - \boldsymbol{\Theta}_s$ is directed along the side of the hexagon, and

$$\frac{\partial \boldsymbol{\Theta}}{\partial z} = +\frac{\alpha}{2}(\boldsymbol{\Theta} - \boldsymbol{\Theta}_s), \tag{18}$$

if $\boldsymbol{\Theta} - \boldsymbol{\Theta}_s$ is directed perpendicularly to the side of the hexagon. Therefore, for an absorbing (amplifying) medium with $\alpha > 0$ ($\alpha < 0$), the points (8) are of the type of a stable (unstable) knot, the points (9) are of the type of an unstable (stable) knot, and the points (10) are of the type of a saddle in the $\boldsymbol{\Theta}$-phase plane. Below, we shall explore the case of the absorbing medium with $\alpha > 0$. If the input pulse Vector Area falls inside the unit cell, then the Vector Area must change during propagation until it reaches the unit cell center. If the input Vector Area is not equal to (9) and (10) and falls on a side of the hexagon, then the Vector Area must change during propagation until it reaches the midpoint of the hexagon side. It is necessary to note that the Vector Area Theorem map (Fig. 2) allows one to easily predict only the sum of the pulse vector areas at the output of the sample. To determine the number of the output SIT solitons and their polarization and area, one should solve the system of coupled Maxwell–Bloch equations.

The input pulse with the Vector Area directed between the crystallographic axes and equal, for example, to $\boldsymbol{\Theta}_+$ excites only four ($\pm\alpha$, $\pm\gamma$) ion subgroups. This pulse is a 2π-pulse for these ions. It does not excite $\pm\beta$ ions, because $\boldsymbol{\Theta}_+ \perp \mathbf{e}_{\pm\beta}$. Similarly, the input pulse with the Vector Area equal to $\boldsymbol{\Theta}_-$ is the 2π-pulse for ($\pm\alpha$, $\pm\beta$)-ion subgroups and does not excite $\pm\gamma$ ions. If the input Vector Area is parallel to $\boldsymbol{\Theta}_+$ ($\boldsymbol{\Theta}_-$) and falls inside the unit cell $\boldsymbol{\Theta}_c = m\boldsymbol{\Theta}_+$ ($\boldsymbol{\Theta}_c = m\boldsymbol{\Theta}_-$), then the time evolution of the pulse may be described by the inverse scattering method. The input pulse is split at the output into m SIT solitons with Vector Areas equal to $\boldsymbol{\Theta}_+$ ($\boldsymbol{\Theta}_-$), as in the isotropic medium. We refer to these solitons as $\boldsymbol{\Theta}_+$ solitons and $\boldsymbol{\Theta}_-$ solitons. If the input Vector Area is not parallel to $\boldsymbol{\Theta}_+$ ($\boldsymbol{\Theta}_-$) but falls inside the unit cell $\boldsymbol{\Theta}_c = m\boldsymbol{\Theta}_+$ ($\boldsymbol{\Theta}_c = m\boldsymbol{\Theta}_-$), then numerical calculations show that the input pulse is also split into m $\boldsymbol{\Theta}_+$ ($\boldsymbol{\Theta}_-$) solitons at the output.

If the input pulse Vector Area is directed along the crystallographic axis, for example, and the α axis is equal to

$$\boldsymbol{\Theta}_0 = \boldsymbol{\Theta}_+ + \boldsymbol{\Theta}_-, \tag{19}$$

then all ($\pm\alpha$, $\pm\beta$, $\pm\gamma$) ions are excited. The input pulse is the 2π-pulse for ($\pm\beta$, $\pm\gamma$)-ion subgroups and the 4π-pulse for ($\pm\alpha$) ions. The time evolution of the pulse is not described by the inverse scattering method. The numerical calculations show that, if the input Vector Area $\boldsymbol{\Theta}_{in}$ is parallel to $\boldsymbol{\Theta}_0$ and falls inside the unit cell $\boldsymbol{\Theta}_c = m\boldsymbol{\Theta}_0$, then the input pulse is split into m SIT solitons with Vector Areas equal to $\boldsymbol{\Theta}_0$. We refer to these solitons as $\boldsymbol{\Theta}_0$ solitons. Let the input Vector Area be not parallel to the $\boldsymbol{\Theta}_0$ and fall inside the unit cell $\boldsymbol{\Theta}_c = m\boldsymbol{\Theta}_0$. Then, as one can see in Figs. 2 and 3, a small change in the input pulse polarization leads to the splitting of each $\boldsymbol{\Theta}_0$ soliton into $\boldsymbol{\Theta}_+$-and $\boldsymbol{\Theta}_-$ solitons. Therefore, the number of solitons and their polarization strongly depend on the direction of the vector $\boldsymbol{\Theta}_{in}$ with respect to the crystallographic axis. This conclusion is also valid in the general case when the input Vector Area falls inside the unit cell $\boldsymbol{\Theta}_c = m\boldsymbol{\Theta}_+ + n\boldsymbol{\Theta}_-$, where $m \neq n$. This is valid because the unit-cell center coordinates may be rewritten as $\boldsymbol{\Theta}_c = (m-n)\boldsymbol{\Theta}_+ + n\boldsymbol{\Theta}_0$ if $m > n$, or as $\boldsymbol{\Theta}_c = (n-m)\boldsymbol{\Theta}_- + m\boldsymbol{\Theta}_0$ if $n > m$. At first, there are $(m-n)\boldsymbol{\Theta}_+$ soli-

tons for $m > n$, or $(n - m)\mathbf{\Theta}_-$ solitons if $n > m$ at the output. Then, the number of solitons appearing at the output depends on the direction of the vector $\mathbf{\Theta}_{in} - (m - n)\mathbf{\Theta}_+$ or $\mathbf{\Theta}_{in} - (n - m)\mathbf{\Theta}_-$ with respect to the crystallographic axis. In the stable case, the output solitons are $\mathbf{\Theta}_+$ solitons and $\mathbf{\Theta}_-$ solitons, and their number is $(m + n)$.

For the amplifying medium, $\mathbf{\Theta}_+$ solitons and $\mathbf{\Theta}_-$ solitons are unstable, so the polarization of the output solitons must be directed along the crystallographic axis in the stable case.

It is necessary to note that for circular polarization of the laser pulse the equation for the Area is of the form (1), as in the case of isotropic medium.

To summarize, we have shown by the example of the model system $LaF_3 : Pr^{3+}$ that the Vector Area mapping of the pulse time evolution during propagation is an effective method for analyzing the polarization properties of solitons.

I thank Ildar Ahmadullin for help with the assimilation of Fortran 90 and Ashat Basharov for his useful notes. This work was supported by the ISTC (grant no. 737) and the Russian Foundation for Basic Research (project no. 00-02-16510).

REFERENCES

1. S. L. McCall and E. L. Hahn, Phys. Rev. Lett. **18**, 908 (1967).
2. V. N. Lisin, Pis'ma Zh. Éksp. Teor. Fiz. **57**, 402 (1993) [JETP Lett. **57**, 414 (1993)].
3. G. L. Lamb, in *Elements of Soliton Theory* (Wiley, New York, 1980).

JETP Letters, Vol. 74, No. 5, 2001, pp. 288–292. From Pis'ma v Zhurnal Éksperimental'noĭ i Teoreticheskoĭ Fiziki, Vol. 74, No. 5, 2001, pp. 318–322.

Stimulated Light Backscattering from Exciton Bose Condensate[1]

Yu. E. Lozovik* and I. V. Ovchinnikov

Institute of Spectroscopy, Russian Academy of Sciences, Troitsk, Moscow region, 142190 Russia

** e-mail: lozovik@isan.troitsk.ru*

Received August 8, 2001

A new effect—light backscattering from exciton Bose-condensate—is considered. This effect is connected with the photoinduced coherent recombination of two excitons in the condensate with the production of two photons with opposite momenta. The effect of two-exciton coherent recombination leads also to the appearance of the second-order coherence in exciton luminescence connected with squeezing between photon states with opposite momenta. The estimations given for Cu_2O and GaAs excitons show that the effect of stimulated light backscattering can be detected experimentally. Moreover, in the system of 2D excitons in coupled quantum wells, the effect of *stimulated anomalous light transmission* must also take place. Anologous effects can also take place in systems of Bose-condensed atoms in excited (but metastable) states. © *2001 MAIK "Nauka/Interperiodica"*.

PACS numbers: 71.35.Lk; 78.45.+h

Great progress has recently been made in the study of exciton Bose condensation in 3D and 2D exciton systems (see [1–8] and references therein). The study of various ways in which exciton condensate should unambiguously reveal itself by its optical properties is vital [9, 10].

In this letter, we analyze the coherent coupling of photons with opposite momenta originating from the coherent recombination of two excitons from the condensate. We reveal that this process leads to a new effect—stimulated light *backscattering* from exciton condensate. This effect can be viewed as the photoinduced coherent recombination of two *condensate* excitons with the production of two photons with opposite momenta.

1. Let us first consider 3D excitons in Cu_2O. The direct recombination of the electron and hole in Cu_2O is a forbidden process, and an exciton decays mainly with the production of a photon and an optical phonon. The interaction Hamiltonian is

$$\hat{V}(t) = \sum_{\mathbf{p}-\mathbf{k}-\mathbf{q}=0} \frac{\hbar L_{k,q}}{\sqrt{V}} \hat{a}^{\dagger}_{\mathbf{p}}(t)\hat{c}_{\mathbf{k}} e^{-i\omega_{\mathbf{k}}t} \times (\hat{b}_{\mathbf{q}} e^{-i\omega_{phn,\mathbf{q}}t} + \hat{b}^{\dagger}_{-\mathbf{q}} e^{i\omega_{phn,\mathbf{q}}t}) + \text{H.c.}, \quad (1)$$

where $\hat{a}(\hat{a}^{\dagger})$, $\hat{b}(\hat{b}^{\dagger})$, and $\hat{c}(\hat{c}^{\dagger})$ are the exciton, phonon, and photon destruction (creation) operators, respectively; $\omega_{phn,\mathbf{q}}$ is the optical phonon dispersion; V is volume of the system; L is the effective interaction constant; $\omega_{\mathbf{k}} = ck$ is the frequency of photons with wave vector $\pm\mathbf{k}$; and $c = c_0/n$ is the speed of light in Cu_2O ($n \approx 3$).

In *normal* phase of the exciton system, the main process of exciton recombination is determined by the diagram in Fig. 1a. The spectrum of exciton luminescence shows a broadened peak at the frequency $\approx\omega_{ex}(\mathbf{0}) - \omega_{phn}(\mathbf{0})$ [9]. The radiative lifetime of an isolated exciton with wave vector $\mathbf{k} = 0$ can be written as

$$\frac{1}{\tau_{Cu_2O}} = \frac{|L(k_0, k_0)|^2 k_0^2}{\pi c}, \quad (2)$$

where L is the matrix element in Eq. (1); k_0 is the absolute value of the photon wave vector $\approx E_g/c\hbar$; and E_g is the energy gap in Cu_2O, $E_g \approx 2$ eV. The process of two-exciton recombination (Fig. 1b) has an extra vertex of exciton–photon interaction and, therefore, is substantially weaker.

In the *Bose-condensed* phase of the exciton system, the exciton lines in Fig. 1b can belong to excitons from the condensate (see Fig. 1c). One-exciton recombination from the condensate (Fig. 1a) has the only large factor $\sqrt{N_0}$, where N_0 is the number of quanta in the macroscopically populated lowest quantum exciton state, while *two-exciton recombination has two such factors*. The additional factor can compensate the weakness of the process, in comparison with the process given in Fig. 1a, and thus make the rate of two-exciton recombination on the order of the one-exciton recombination rate. In pure samples, due to momentum and energy conservation laws, two created photons have the same energy and the opposite momenta. The

[1] This article was submitted by the authors in English.

luminescence originating from this recombination process has a peak at the chemical potential of the exciton system, measured from the valence band $\hbar\mu$ ($\hbar\mu \approx E_g$). Due to the fact that in two-exciton recombination no energy is transformed to phonons, the frequency of two-exciton recombination luminescence is higher than that of one-exciton recombination by a value of $\omega_{phn} \ll E_g/\hbar$ (Fig. 2).

The rate of two-exciton recombination with the production of two photons with wave vectors $\pm\mathbf{k}$ is

$$W^{\text{spon}}_{\text{Cu}_2\text{O}}(\mathbf{k}) = 2\pi\delta(2\omega_{\mathbf{k}} - 2\mu)|M(\mathbf{k})|^2, \quad (3)$$

where M is the matrix element of the process. The overall rate of spontaneous photon emission in the two-exciton recombination process per unit volume is obtained by integrating $W^{\text{spon}}_{\text{Cu}_2\text{O}}(\mathbf{k})$ over all photon wave vectors $\mathbf{k}$ and multiplying the result by 2 (at every elementary event of the process, two photons are created):

$$W^{\text{spon}}_{\text{Cu}_2\text{O}} = \frac{k_0^2}{\pi c}|M(k_0)|^2. \quad (4)$$

The matrix element $M(\mathbf{k})$ has the form

$$M_{\text{Cu}_2\text{O}}(k_0) = G_{phn}(0, k_0)L(k_0, k_0)^2\rho_{\text{cond}}, \quad (5)$$

where ρ_{cond} is the spatial density of the condensate, and

$$G_{phn}(\omega, \mathbf{q}) = (\omega - \omega_{\mathbf{q}} + i\delta)^{-1} - (\omega + \omega_{\mathbf{q}} - i\delta)^{-1} \quad (6)$$

is the phonon Green's function. Combining Eqs. (4), (5), and (2), one obtains

$$W^{\text{spon}}_{\text{Cu}_2\text{O}} = \frac{1}{\tau_{\text{Cu}_2\text{O}}}\frac{4\pi c\rho^2_{\text{cond}}}{k_0^2\omega^2_{phn}\tau_{\text{Cu}_2\text{O}}}. \quad (7)$$

In Cu_2O, the radiative lifetime of exciton $\tau_{\text{Cu}_2\text{O}}$ [see Eq. (2)] is approximately 10 μs and the energy of the optical phonon ω_{phn} is 10^{-2} eV. Taking as an estimation $\rho_{\text{cond}} = 10^{19}$ cm^{-3}, we have the rate of photon creation in coherent *two-exciton* recombination process, which is

$$W^{\text{spon}}_{\text{Cu}_2\text{O}} \approx \frac{1.5\times 10^{-2}}{\tau_{\text{Cu}_2\text{O}}}\rho_{\text{cond}}, \quad (8)$$

while the rate of photon creation in *one-exciton* recombination from the condensate is $\tau^{-1}_{\text{Cu}_2\text{O}}\rho_{\text{cond}}$. This result shows that approximately every hundredth exciton in the condensate decays due to the process under consideration. Therefore, the spontaneous two-exciton recombination process is still weak, in spite of the extra bosonic (excitonic) factor $\sqrt{N_0}$ in the matrix element of the process (Fig. 1c). However, the process can be induced by external resonant radiation (with frequency $\omega = \mu$) propagating through the Bose-condensed exciton system (Fig. 1d). At every event of such exciton recombination, not only a photon propagating along the inducing radiation direction is created but also a photon propagating in the opposite direction. Consequently, it appears that the process effectively acts as a light *backscattering* from the condensate. The rate with which photons are emitted in the opposite direction is

$$W_{-\mathbf{k}} = (N_{\mathbf{k}} + 1)W^{\text{spon}}_{\mathbf{k}}, \quad (9)$$

where N_k is the average number of quanta in the quantum state of the inducing photon beam with the wave

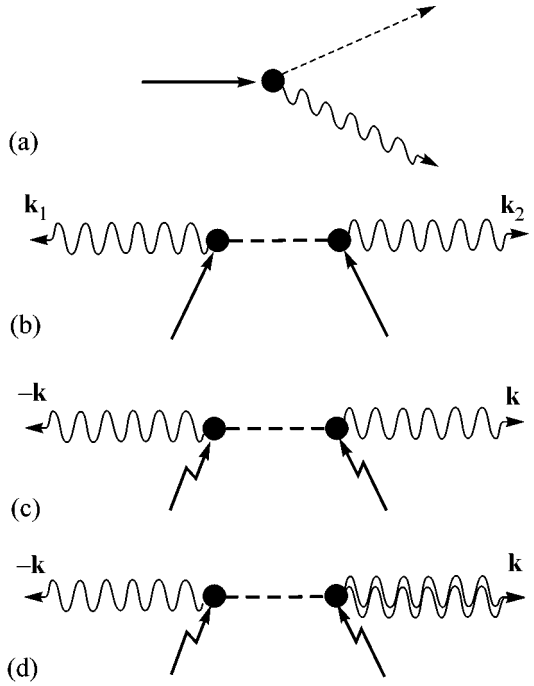

Fig. 1. (a) The diagram of one-exciton recombination in Cu_2O; dashed line represents phonon, straight line represents exciton, and wavy line represents photon. (b) The diagram of the two-exciton recombination process where the phonon is virtual. (c) The diagram of recombination of two excitons from the condensate. Due to momentum conservation, photons have opposite wave vectors. (d) The process of two-exciton recombination stimulated by an external beam with wave vector k; double wavy line represents a classical laser field.

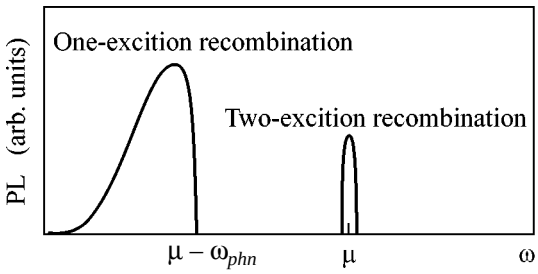

Fig. 2. The schematic photoluminescence (PL) spectrum of Cu_2O. One-exciton recombination results in the spectrum at the left of the figure. This portion of the spectrum was studied, e.g., in [9]. The portion of the spectrum at the right of the figure corresponds to two-exciton recombination. It has a higher energy, since no energy is transformed to phonons.

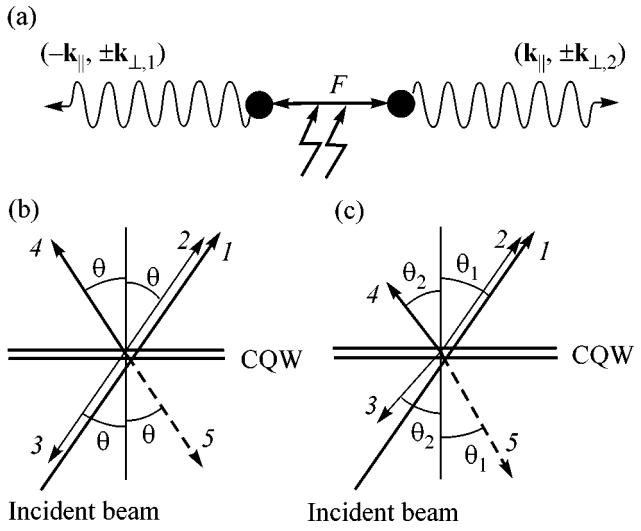

Fig. 3. (a) The diagram of two-exciton recombination from 2D exciton condensate in QW or CQW. *F* is the anomalous Green's function; wavy lines represent photons with opposite in-plane wave-vector components. (b) Laser beam induces two processes of two-exciton recombination, which are different in the signs of normal wave-vector components of photons with in-plane components $-k_{||}$. Light also undergoes normal reflection from CQW planes. (*1*) Normally transmitted laser beam; (*2*) stimulated emission; (*3*) stimulated backscattering; (*4*) stimulated anomalous transmission; and (*5*) normal reflection from CQW. (c) Nonresonant case; i.e., stimulating beam has energy substantially different from chemical potential of excitons $\hbar\mu$; photons with in-plane components $-k_{||}$ (c, d) have energies $\hbar\omega_2$ different from the energy of incident light ω_1. Normal components are also different. The angles θ_1, θ_2 obey the relation $\sin(\theta_1)/\sin(\theta_2) = \omega_2/\omega_1$. 1, 2, 3, 4, 5 denote the same as in part (b) of the Figure.

vector **k**; the unity takes into account the spontaneous two-exciton recombination.

Consequently, the inducing beam at the frequency $\omega = \mu$, which has approximately one hundred quanta per mode, makes the two-exciton recombination luminescence in one opposite direction of the same intensity as the one-exciton recombination luminescence [see Eq. (8)]. This comment implies that the effect of stimulated backscattering of a laser beam on exciton condensate can be detected experimentally.

In the absence of an inducing beam, two-exciton recombination luminescence is squeezed between the photon states with opposite momenta (two-mode squeezing). Luminescence at a given direction does not possess statistical coherence. The only statistical correlation which luminescence has is the correlation between the opposite-direction luminescence intensities. This correlation can be detected by Hunburry–Brown–Twiss measurements with two detectors arranged diagonally with respect to the exciton system.

2. Now we consider a direct-gap semiconductor with an allowed interband transition such as GaAs. However, in GaAs 3D excitons do not form Bose condensate but, rather, gather into metallic electron–hole drops. Recently, GaAs excitons and their coherent properties have been much studied in two dimensions—in coupled quantum wells (CQW). In CQW, spatially indirect excitons have electric dipoles, and their interaction has a strongly repulsive character making them able to form stable Bose condensate at $T = 0$ (or a quasi-long, nondiagonal-order, superfluid phase with local quasi-condensate at temperatures lower than the temperature of the Kosterlitz–Thouless transition). CQW is a quasi-2D system, where only *2D in-plane momentum is conserved*. The operator of exciton–photon interaction in the interaction picture can be given as

$$\hat{V}(t) = \hbar\sum_{\mathbf{k}}\frac{\mathbf{g}(\omega_{\mathbf{k}})}{\sqrt{L}}(\hat{a}_{\mathbf{k}_{||}}(t)\hat{c}^{\dagger}_{\mathbf{k}}e^{-i\omega_{\mathbf{k}}t} + \text{H.c.}), \qquad (10)$$

where $\hat{a}(\hat{a}^{\dagger})$ and $\hat{c}(\hat{c}^{\dagger})$ are exciton and photon destruction (creation) operators, respectively; and $g(\omega)$ is the coupling constant; the vectors $\mathbf{k}_{||}$ are two-dimensional; and L is the width of the system in the direction normal to CQW.

To the lowest order in exciton–photon interaction, the spontaneous rate of a process with the production of two photons with in-plane wave vector components $\pm\mathbf{k}_{||}$ (Fig. 3a), is

$$W^{\text{spon}}_{\text{GaAs}}(\mathbf{k}_{||}) = \int(2\pi)\delta(\omega_{\mathbf{k}_1} + \omega_{\mathbf{k}_1} - 2\mu)\left|\mathbf{g}(\omega_{\mathbf{k}_1})\mathbf{g}(\omega_{\mathbf{k}_2})\right|^2 \times\left|F(\omega-\mu, \mathbf{k}_{||})\right|^2 dk_{\perp,1}(2\pi)^{-1}dk_{\perp,2}(2\pi)^{-1}, \qquad (11)$$

where F is the anomalous Green's function of an exciton subsystem. For estimations, we take the anomalous Green's function in the form

$$F(\omega, \mathbf{k}_{||}) = -\beta(\omega - \mu - \omega_{ex}(\mathbf{k}_{||}) + i\eta)^{-1} \times(\omega - \mu + \omega_{ex}(\mathbf{k}_{||}) - i\eta)^{-1},$$

$$\omega_{ex}(\mathbf{k}_{||}) = \sqrt{\beta\hbar k_{||}^2 m_{ex}^{-1} + (\hbar k_{||}^2 m_{ex}^{-1})^2}, \quad \hbar\beta = \rho_{\text{cond}}V_0,$$

where m_{ex} is the exciton mass (in GaAs, $m_{ex} \approx 0.22m_0$, where m_0 is the mass of the free electron); ρ_{cond} is the 2D density of excitons in the condensate; V_0 is the zero 2D Fourier component of exciton–exciton interaction potential; ω_{ex} is the dispersion of elementary excitation in an exciton subsystem; and η is the rate of decay of elementary excitation in exciton subsystem; for simplicity, we take this parameter to be frequency independent. The energy of elementary excitation in an exciton system is negligibly small in comparison with the gap

between valence and conduction bands. Therefore, one can substitute in Eq. (11)

$$|F(\omega-\mu,\mathbf{k}_\parallel)|^2 \longrightarrow$$
$$\longrightarrow \frac{\pi(\delta(\omega-\mu-\omega_{ex}(\mathbf{k}_\parallel))+\delta(\omega-\mu+\omega_{ex}(\mathbf{k}_\parallel)))\beta^2}{((2\omega_{ex}(\mathbf{k}_\parallel))^2+\eta^2)\eta} \quad (12)$$
$$\approx \frac{2\pi\delta(\omega-\mu)\beta^2}{((2\omega_{ex}(\mathbf{k}_\parallel))^2+\eta^2)\eta}.$$

This approximation can be viewed as a resonant approximation. In resonant processes, photons are created with frequencies $\mu \pm \omega_{ex}(\mathbf{k}_\parallel) \approx \mu$. These values differ from μ negligibly. Therefore, the absolute values of photon wave vectors with frequencies $\mu + \omega_{ex}(\mathbf{k}_\parallel)$ and $\mu - \omega_{ex}(\mathbf{k}_\parallel)$ differ negligibly as well. Consequently, since they have the same absolute magnitude of in-plane wave vector components, the angles of their propagation θ (Fig. 3b) are almost the same.

Substituting Eq. (12) into Eq. (11), one obtains

$$W_{\mathrm{GaAs}}^{\mathrm{spon}}(\mathbf{k}_\parallel) = \frac{\beta^2}{((2\omega_{ex}(\mathbf{k}_\parallel))^2+\eta^2)\eta} \times\left(\int 2\pi\delta(\omega_{\mathbf{k}_\parallel,\mathbf{k}_\perp}-\mu)|\mathbf{g}(\mu)|^2\frac{dk_\perp}{2\pi}\right)^2. \quad (13)$$

The magnitude in the parentheses is more than the inverse radiative lifetime $\tau_{\mathrm{GaAs}}^{-1}$ of an isolated exciton with the in-plane wave vector $\mathbf{k}_\parallel$. For spatially indirect exciton in GaAs CQW, the radiative lifetime τ_{GaAs} approximately equals 10^{-8} s. Letting τ_{GaAs} be independent of $k_\parallel$ and assuming that the entire radiative zone ($k_\parallel < k_0$) corresponds to the linear part of the elementary excitation spectrum in the exciton subsystem, one can integrate $W_{\mathrm{GaAs}}^{\mathrm{spon}}(k_\parallel)$ over the radiative zone, yielding the total spontaneous rate of the process per unit area of CQW in the form

$$W_{\mathrm{GaAs}}^{\mathrm{spon}} = \frac{\beta m_{ex}}{16\pi\hbar\eta\tau_{\mathrm{GaAs}}^2}\log\left(1+\frac{4\beta\hbar k_0^2}{m_{ex}\eta^2}\right). \quad (14)$$

Taking, as an estimation, the exciton density $\rho_{\mathrm{cond}} = 10^{10}$ cm^{-2}, $\hbar\beta = 0.5$ meV, $\eta = 10^{7-10}$ s^{-1}, $k_0 = 3\times10^5$ cm^{-1}, we have

$$W_{\mathrm{GaAs}}^{\mathrm{spon}} \approx \frac{10^{2\ldots-2}}{\tau_{\mathrm{GaAs}}}\rho_{\mathrm{cond}}.$$

This result shows [compare with Eq. (8)] that the effect of interest can be detected in the system of indirect excitons in GaAs/AlGaAs CQW.

Since, in two dimensions, the third component of the photon wave vector is not fixed and is determined only by the energy conservation law, the rate (11) corresponds to *four processes* in which the photons with wave vectors ($\mathbf{k}_\parallel$, $\pm\mathbf{k}$) and ($-\mathbf{k}_\parallel$, $\pm\mathbf{k}_\perp$) are created. Therefore, stimulating laser light with the in-plane wave-vector component $\mathbf{k}_\parallel$ induces *two processes* in which the photons with in-plane components $\mathbf{k}_\parallel$ are emitted in two directions ($-\mathbf{k}_\parallel$, $\pm\mathbf{k}_\perp$); i.e., in addition to stimulated backscattering, *stimulated anomalous light transmission* arises, in which only the in-plane wave-vector component changes its sign (Fig. 3b).

Furthermore, in the process of interest, it is not necessary that the photons be "resonant"; i.e., photons can have energies ω different from $\mu \pm \omega_{ex}(\mathbf{k}_\parallel)$ [see Eq. (12)]. However, the rate of this process is low, and for $|\omega-\mu| \gg \omega_{ex}(\mathbf{k}_\parallel)$ it is proportional to $(\omega-\mu)^{-4}$. In such processes, photons with different energies ω_1 and ω_2 have different normal wave components as well. The angles of their propagation obey the relation $\sin(\theta_1)/\sin(\theta_2) = \omega_2/\omega_1$ (Fig. 3c).

In conclusion, we have predicted and estimated a new optical effect of stimulated light backscattering from exciton Bose condensate. Moreover, being detected, this effect is nothing more than the signature of exciton Bose condensate, since there are no other possibilities for the light to undergo backscattering from the exciton subsystem. Estimations given in this work for Cu_2O excitons and excitons in GaAs/AlGaAs CQW show that the effect can be observed experimentally.[2] The angular distribution in the backscattering process is smeared by impurities or interface roughness, due to which the exciton momentum is not a good quantum number. The characteristic angle at which the photons are emitted can be estimated as $1/k_0 l$, where l is the mean free path of an exciton.

For the described effect to exist, it is essential that exciton condensate be *quasi*-equilibrium; i.e., the Bose-condensed system is not a ground state of the total system but has excess energy which can be transferred to photons. For example, there is no such effect in the case of the Bose condensate of atoms in their *ground state*. However, the analogous effect can exist in the system of metastable Bose-condensed atoms. Studies of Bose condensation in the systems of metastable atoms have been recently initiated.

This work was supported by the INTAS, the Russian Foundation for Basic Research, and the Program "Solid State Nanostructures."

REFERENCES

1. *Bose–Einstein Condensation*, Ed. by A. Griffin, D. W. Snoke, and S. Stringari (Cambridge Univ. Press, Cambridge, 1995); S. A. Moskalenko and D. W. Snoke, *Bose–Einstein Condensation of Excitons and Biexcitons and Coherent Nonlinear Optics with Excitons* (Cambridge Univ. Press, New York, 2000).

[2] Experimentally, the effect of backscattering can be studied using semitransparent mirror.

2. A. L. Ivanov, H. Haug, and L. V. Keldysh, Phys. Rep. **296**, 237 (1998); L. V. Keldysh and Yu. V. Kopaev, Fiz. Tverd. Tela (Leningrad) **6**, 2791 (1964) [Sov. Phys. Solid State **6**, 2219 (1965)]; A. N. Kozlov and L. A. Maximov, Zh. Éksp. Teor. Fiz. **48**, 1184 (1965) [Sov. Phys. JETP **21**, 790 (1965)]; V. A. Gergel, R. F. Kazarinov, and R. A. Suris, Zh. Éksp. Teor. Fiz. **53**, 544 (1967) [Sov. Phys. JETP **26**, 354 (1968)]; B. I. Halperin and T. M. Rice, Solid State Phys. **21**, 115 (1968); L. V. Keldysh and A. N. Kozlov, Zh. Éksp. Teor. Fiz. **54**, 978 (1968) [Sov. Phys. JETP **27**, 521 (1968)]; E. Hanamura and H. Haug, Phys. Rep. **33**, 209 (1977).
3. Yu. E. Lozovik and O. L. Berman, Pis'ma Zh. Éksp. Teor. Fiz. **64**, 526 (1996) [JETP Lett. **64**, 573 (1996)]; Yu. E. Lozovik, O. L. Berman, and V. G. Tsvetus, Phys. Rev. B **59**, 5627 (1999) and references therein.
4. L. V. Butov and I. V. Filin, Phys. Rev. B **58**, 1980 (1998).
5. P. Kner, S. Bar-Ad, M. V. Marquezini, *et al.*, Phys. Rev. B **60**, 4731 (1999).
6. J.-P. Cheng, J. Kono, B. D. McCombe, *et al.*, Phys. Rev. Lett. **74**, 450 (1995).
7. D. W. Snoke, J. P. Wolf, and A. Mysyrowicz, Phys. Rev. Lett. **64**, 2543 (1990); E. Fortin, S. Fafard, and A. Mysyrowicz, Phys. Rev. Lett. **70**, 3951 (1993); E. Benson, E. Fortin, and A. Mysyrowicz, Solid State Commun. **101**, 313 (1997).
8. A. V. Larionov, V. B. Timofeev, J. Hvam, *et al.*, Pis'ma Zh. Éksp. Teor. Fiz. **71**, 174 (2000) [JETP Lett. **71**, 117 (2000)]; A. V. Larionov and V. B. Timofeev, Pis'ma Zh. Éksp. Teor. Fiz. **73**, 342 (2001) [JETP Lett. **73**, 301 (2001)].
9. M. Inoue and E. Hanamura, J. Phys. Soc. Jpn. **41**, 1273 (1976); H. Shi, G. Verechaka, and A. Griffin, Phys. Rev. B **50**, 1119 (1994).
10. Yu. E. Lozovik and A. V. Poushnov, Phys. Rev. B **58**, 6608 (1998).